ABSTRACT

Title of Dissertation: TENSOR NETWORK APPROACHES IN NON-EQUILIBRIUM QUANTUM MANY-BODY DYNAMICS

Yongchan Yoo
Doctor of Philosophy, 2024

Dissertation Directed by: Professor Brian Swingle
Department of Physics

Understanding the dynamics of non-equilibrium quantum systems has been a longstanding challenge in a wide range of physical phenomena. Recent advancements in various quantum technologies have driven theoretical investigations of non-equilibrium quantum many-body dynamics. A crucial aspect of the theory is the development of computational methods, which have led to significant results and show promising directions for further development. However, simulating these complex systems using classical algorithms remains extremely difficult, primarily due to the challenge of identifying physically principled and efficient approximations capable of reducing their computational complexity.

This thesis discusses theoretical and numerical studies on the non-equilibrium dynamics of quantum many-body systems, particularly focusing on the steady-state transport of conserved quantities in various one-dimensional spin systems. We study transport phenomena employing boundary-driven open quantum setups and investigate various aspects of the non-equilibrium

dynamics induced by these systems. Our goal is to understand steady-state phenomena and to push the boundaries of simulation capacity using state-of-the-art technologies.

In the first part, we examine the non-equilibrium steady-state (NESS) phases of an interacting Aubry-André-Harper model. This model involves a quasiperiodic potential, leading to interesting emergent collective phenomena. The observed spin transport and quantum correlation structure suggest the presence of multiple dynamical phases between the well-studied thermal and many-body-localized phases.

In the second part, we study the impact of operator weight dissipation on the scaling behavior of transport in various spin models. Our findings suggest that dissipation's effect on transport depends on the system's conserved quantities. When dissipation preserves these symmetries, it maintains the scaling of the system's transport properties. However, when it disrupts these conserved quantities, it leads the system towards diffusive scaling of transport.

In the third part, we investigate energy transport within the non-integrable regime of the $\mathbb{Z}_3$ chiral clock model, utilizing Lindblad operators with adjustable size and temperature. Through scaling analysis, we extract the model's transport coefficients at relatively high temperatures, both above its gapless and gapped low-temperature phases. Furthermore, we calculate the temperature dependence of the energy diffusion constant across various model parameters, including the regime where the model exhibits quantum critical behavior at low temperatures.

TENSOR NETWORK APPROACHES IN NON-EQUILIBRIUM QUANTUM MANY-BODY DYNAMICS

by

Yongchan Yoo

Dissertation submitted to the Faculty of the Graduate School of the
University of Maryland, College Park in partial fulfillment
of the requirements for the degree of
Doctor of Philosophy
2024

Advisory Committee:
Professor Brian Swingle, Chair/Advisor
Professor Jay Deep Sau, Co-Chair
Professor Maissam Barkeshli
Professor Michael Gullans
Professor Christopher Jarzynski

Dedication

To my beloved family

Acknowledgments

I feel incredibly fortunate and deeply appreciative of the extraordinary journey I've had at the University of Maryland. My heart is overflowing with gratitude for the countless individuals whose invaluable contributions have shaped my academic experience and the realization of my thesis.

At the helm of this transformative journey is my exceptional advisor, Professor Brian Swingle. His unwavering guidance has been the cornerstone of my academic odyssey. From the onset of my graduate studies, his patient mentorship and illuminating conversations have been instrumental in shaping my intellectual growth and guiding me through the complexities of forefront problems. His steadfast support and encouragement have been indispensable in crafting this dissertation. Moreover, beyond his role as an advisor, he has become a cherished friend and mentor. Through his unwavering belief in my capabilities, he has instilled confidence while fostering a boundless freedom of imagination.

I am deeply grateful to the esteemed faculty at the University of Maryland. Their expertise has not only enriched my academic journey but has also provided inspiration and guidance crucial to my development. Special recognition goes to Professors Jay Deep Sau, Maissam Barkeshli, Michael Gullans, and Christopher Jarzynski, whose generous dedication of time and expertise as members of my thesis committee has significantly influenced my work.

The camaraderie and collaboration of fellow students and colleagues, including Stefano

Antonini, Christopher Baldwin, Charles Cao, Cheng Gong, Andrew Guo, Shaokai Jian, Junhyun Lee, Subhayan Sahu, Troy Sewell, Yixu Wang, Christopher White, Michael Winer, and Cris Zanoci, have profoundly enriched my academic journey. Their passion for science and the shared pursuit of knowledge have undoubtedly made a lasting impact on my life.

Equally, I extend my heartfelt gratitude to all staff members in the Physics Department, Condensed Matter Theory Center, and Joint Quantum Institute for their unwavering support. Their contributions and nurturing environment have played an integral role in making my experience truly exceptional.

Finally, I must express my deepest appreciation to my family - my unwavering pillars of support. My mother, father, and late grandparents have been my unwavering believers, guiding me through every challenge with love and encouragement. Above all, my lovely wife, Myungjin Lee, has been my steadfast companion, facing every hardship together. I am convinced that the adventure of discovering remarkable pieces of knowledge and insight during my graduate school years will undoubtedly open new horizons for the next stage of my life.

Summary of Research Contributions

The research documented in this thesis, as published in papers [1–4], was conducted during my graduate studies in collaboration with Brian Swingle, Junhyun Lee, Christopher David White, and Cris Zanoci.

By the guidelines set forth by the University of Maryland and the Physics Department's Graduate Director, Chapters 2 to 4 of this thesis reproduce the contents of references [1–3] verbatim. Additionally, Appendices A to C reproduce the corresponding papers, except two subsections in Appendix C, drawn from reference [4], to provide a deeper insight into the methodologies employed in Chapter 4. The specific contributions of each author to different sections of the thesis are detailed as follows:

Chapter 1 serves as introductory material, providing the requisite theoretical background for understanding non-equilibrium quantum many-body dynamics within the framework of tensor network ansatz. This chapter is solely authored by myself.

Chapter 2 and Appendix A were originally published as reference [1]. All authors contributed to the conceptual development, while detailed calculations and simulations were exclusively undertaken by myself.

Chapter 3 and Appendix B were originally published as reference [2]. Once again, all authors contributed to the conceptual development, while detailed calculations and simulations were exclusively carried out by myself.

Chapter 4 and Appendix C were originally published as reference [3]. This chapter represents a continuation of the method developed in the preceding paper [4], with relevant sections directly extracted and presented in Appendix C. Both authors contributed to the conceptual development, while detailed calculations and simulations were exclusively conducted by myself.

Chapter 5 provides a summary and outlook of the thesis, authored solely by myself.

Table of Contents

List of Figures

List of Abbreviations

AAH	Aubry-Andre-Harper
CCM	Chiral Clock Model
CPTP	Completely Positive Trace Preserving
DAOE	Dissipation-Assisted Operator Evolution
DMRG	Density Matrix Renormalization Group
GKSL	Gorini-Kossakowski-Sudarshan-Lindblad
MBL	Many-Body Localization
MPDO	Matrix Product Density Operator
MPO	Matrix Product Operator
MPS	Matrix Product State
NESS	Non-Equilibrium Steady State
t-DMRG	Time-dependent Density Matrix Renormalization Group
TEBD	Time-Evolving Block Decimation

Chapter 1: Introduction

1.1 Overview

Non-equilibrium phenomena are inherent in a broad spectrum of physical realms and scales from transport in condensed matter systems to dynamics of cosmological scale structures and beyond. In many-body physics, a prominent example of a non-equilibrium scenario involves the steady-state transport of conserved quantities, such as charge or energy. It is elegantly described by established laws like Fourier's law, which correlates energy current with a temperature gradient. While these concepts naturally extend to quantum many-body systems, the underlying microscopic mechanisms remain elusive. Of particular interest are strongly correlated quantum systems in one dimension, representing the simplest battleground one can imagine with profound theoretical importance. In these systems, quantum fluctuations give rise to exotic dynamical properties unique to such physical systems. For instance, the absence of finite-temperature phase transitions and the breakdown of Landau's Fermi liquid theory make one-dimensional systems remarkable in their own right. One reason for such complication is that one-dimensional systems often exhibit larger entanglement than higher dimensional systems where mean field theory becomes exact [5]. Notably, the low-temperature behavior of one-dimensional quantum systems is succinctly captured by the universal Tomonaga-Luttinger theory, a framework that is effectively addressed through bosonization techniques.

The renewed interest in one-dimensional systems arises from the study of non-equilibrium dynamics in closed quantum systems [6–9] and many-body localization [10, 11]. In these areas, one-dimensional systems are employed to explore new concepts, novel phase transitions, and dynamics far from equilibrium. Additionally, the integrability of specific one-dimensional systems allows for a systematic examination of the transition between integrability and quantum-chaotic behavior [12–14]. Meanwhile, groundbreaking experiments on low-dimensional systems, particularly in cold atom systems [15–17], have contributed significantly to these research areas. These platforms enable precise control and manipulation of quantum many-body dynamics at a microscopic level, leading to accelerated theoretical understanding of these fundamental phenomena.

Interestingly, simulating open quantum many-body systems poses a significant challenge for classical computers, surpassing closed systems. Because compared to a pure state, a density matrix has more data stemming from its statistical nature. However, it is remarkable that experimentally preparing the stationary state of an open quantum system is notably simpler than achieving the ground state of a closed system. These unique attributes position open quantum systems as promising candidates for illustrating the quantum advantage of quantum simulators over classical methods, particularly within noisy intermediate-scale quantum devices [18]. Nevertheless, harnessing this potential necessitates a thorough evaluation of the capabilities of classical simulation methods.

In particular, the study of transport phenomena in one-dimensional quantum systems is a complex and challenging task, both conceptually and computationally. Even in the presence of local interactions, where the corresponding equilibrium problem is well understood, calculating transport coefficients is often formidable. However, the boundary-driven open quantum systems among the current state-of-the-art technologies provide a compelling solution to this problem.

This setup, which links an isolated system to a drive at its boundaries, is expected to reduce system entanglement, thereby facilitating the exploration of transport physics near the thermodynamic limit. Consequently, the desired non-equilibrium steady state (NESS) can be obtained in such a low-entanglement simulation.

Combining boundary-driven open quantum systems with tensor network-based simulations has shown great potential, with practical implications in various fields. However, many essential questions in this field have yet to be thoroughly explored, making it a very active and promising study area. Although entanglement may be low during time evolution in these settings, accurately capturing the NESS requires a significant amount of entanglement, especially for large system sizes and long-time simulations. This necessitates extensive computational resources. Furthermore, understanding the transport properties of strongly interacting systems, which often have complex dynamic phase diagrams, poses significant challenges. For example, the transport properties of well-studied models such as the XXZ model are still poorly understood and mostly limited to high (near infinite) temperatures. Even approximations that establish a valid open quantum system framework may not work in such scenarios. Therefore, it is crucial to investigate the limitations of existing theoretical descriptions and develop new tools to overcome these challenges, thereby advancing our understanding of transport phenomena. Within this context, this thesis examines one-dimensional transport under boundary-driven open quantum systems from various angles and configurations, aiming to tackle these open questions and expand the framework's capacity to its limits.

1.2 Non-equilibrium Open Quantum Systems

1.2.1 Quantum Master Equations

The theory of open quantum systems provides a natural framework for understanding quantum transport. In this framework, the state of an open quantum system is described by its density operator, denoted as ρ, which can be represented as a statistical ensemble of pure states. Mathematically, this can be expressed as:

$$\rho = \sum_i p_i |\psi_i\rangle\langle\psi_i|, \tag{1.1}$$

where p_i represents the probability of finding the system in the state $|\psi_i\rangle$. In standard treatments, it's assumed that the overall density matrix of the system and its surrounding baths evolves unitarily, following the Liouville-von Neumann equation:

$$\frac{d\rho_{SB}(t)}{dt} = -i\left[H, \rho_{SB}\right], \tag{1.2}$$

where H is the total Hamiltonian including system, bath, and their interaction. We also set $\hbar = 1$. Initially, ρ_{SB} begins with a product state of the system and the bath states. The focus is on the time evolution of the reduced density matrix $\rho(t) = \mathrm{tr}_B\left[\rho_{SB}\right]$, with $\mathrm{tr}_B\left[\cdot\right]$ denoting the partial trace over the bath. The time evolution of $\rho(t)$ can be expressed as a differential equation derived by applying a projection operator to ρ_{SB} in Eq. (1.2). By manipulating the initial conditions as a factorized state of the system and the bath, the resultant equation typically conforms to the

form [19, 20]:

$$\frac{d\rho(t)}{dt} = \int_0^t dt' \mathcal{K}(t-t')\rho(t'), \tag{1.3}$$

where $\mathcal{K}(t-t')$ is a linear super-operator, termed the memory kernel. This yields a non-local equation in time with a complex memory kernel, often as challenging to handle as the original problem [21].

When considering short bath correlation times, the absence of memory effects allows for the representation of reduced system dynamics as a quantum dynamical semigroup. [22, 23]. Assuming the initial state of the total system as $\rho_{SB}(0) = \rho(0) \otimes \rho_B$, where ρ_B denotes a reference state of the environment, such as a thermal equilibrium state, the dynamical map $V(t)$ that describes the evolution of the reduced density operator over time t can be expressed as $\rho(t) = V(t)\rho(0) = \mathrm{tr}_B\left[U(t)\rho(0) \otimes \rho_B U^\dagger(t)\right]$. Utilizing the spectral decomposition of $\rho_B = \sum_n \lambda_n |\phi_n\rangle\langle\phi_n|$, where $|\phi_n\rangle$ represents an orthonormal basis and $\sum_n \lambda_n = 1$, the dynamical map equation can be written as

$$\rho(t) = V(t)\rho(0) = \sum_{m,n} W_{mn}(t)\rho(0)W_{mn}^\dagger(t), \tag{1.4}$$

where $W_{mn} = \sqrt{\lambda_m}\langle\phi_m|U(t)|\phi_n\rangle$. It immediately follows that $\sum_{m,n} W_{mn}^\dagger(t)W_{mn}(t) = 1$, and therefore $\mathrm{tr}[\rho(t)] = \mathrm{tr}[V(t)\rho(0)] = \mathrm{tr}[\rho(0)] = 1$. As a result, the dynamical map $V(t)$ must be a completely positive and trace-preserving (CPTP) map. It is noteworthy that while a positive map ensures a valid subsystem state, the presence of entanglement with other system components may invalidate the resulting state of the entire system after applying a positive map solely to the subsystem. If the characteristic time scales over which the reservoir correlation functions decay

are much shorter than the system's evolution time scale, neglecting memory effects in reduced system dynamics can be justified. In essence, the action of reservoirs should be as stochastic as possible, indicating the absence of memory within the maps corresponding to Markovian evolution. Formally, the dynamical map $V(t)$ should possess semigroup properties, enabling the evolution to be decomposed into smaller steps as $\rho(t_1+t_2) = V(t_1+t_2)\rho(0) = V(t_1)V(t_2)\rho(0)$.

Given a quantum dynamical semigroup, certain mathematical conditions give rise to a linear map $\mathcal{L}$, which is commonly referred to as the generator of the semigroup. The linear map allows the semigroup's representation in an exponential form $V(t) = \exp(\mathcal{L}t)$, which leads to a differential equation form for the reduced density matrix of the open system, described by:

$$\frac{d\rho(t)}{dt} = \mathcal{L}\rho(t). \tag{1.5}$$

This differential equation, known as the Markovian quantum master equation, is local in time. For an N-dimensional Hilbert space, the orthonormal basis F_μ of the corresponding Liouville space should have a cardinality of N^2. Through an analysis of the previous CPTP map with these N^2 Liouvillian operators, it can be established that the most general form for the generator of the quantum dynamical semigroup takes the following form:

$$\begin{aligned}\frac{d\rho(t)}{dt} = \mathcal{L}\left[\rho(t)\right] &= -i\left[H,\rho(t)\right] + \mathcal{D}[\rho(t)] \\ &= -i\left[H,\rho(t)\right] + \sum_{\mu=1}^{N^2}\left(L_\mu\rho(t)L_\mu^\dagger - \frac{1}{2}L_\mu^\dagger L_\mu\rho(t) - \frac{1}{2}\rho(t)L_\mu^\dagger L_\mu\right).\end{aligned} \tag{1.6}$$

Here, H represents the system's Hamiltonian, $\mathcal{D}$ represents the dissipator, and L_μ are termed Lindblad operators. These operators can be derived by applying an appropriate unitary transfor-

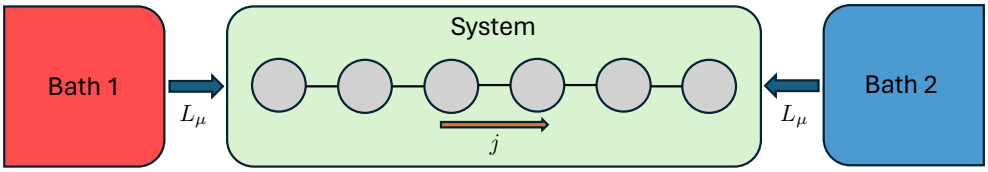

Figure 1.1: Schematics of boundary-driven systems governed by GKLS master equation: The system is locally coupled to external baths represented by Lindblad operators L_μ and internally via a Hamiltonian. This enables NESSs characterized by stationary currents j.

mation to F_μ–which can be any operators including non-Hermitian ones–and can describe the influence of reservoirs. Moreover, it can be deduced that the master equation Eq. (1.6) with prescribed L_μ and H generates a CPTP map, which is desirable for describing Markovian dynamics in open quantum systems. This general form of the Markovian quantum master equation is valid in both finite Hilbert spaces [24] and infinite ones [25], commonly referred to as the GKSL master equation, in homage to Gorini, Kossakowski, Sudarshan, and Lindblad.

Equipped with the GKSL master equation framework, a common approach to investigating non-equilibrium phenomena involves creating a NESS through interactions with reservoirs and examining its properties. The NESS, denoted as ρ_∞, represents a fixed point solution where the master equation yields zero evolution: $\mathcal{L}[\rho_\infty] = 0$. Under certain algebraic conditions on L_μ and H [26–28], it is known that there exists precisely one steady state. In consequence, it can be practically asserted that any initial state eventually converges to this unique NESS after a long time evolution: $\lim_{t\to\infty} e^{\mathcal{L}t}\rho(0) = \rho_\infty$.

1.2.2 Models for Boundary-driven Open Quantum Systems

Compared to their classical counterparts, studying quantum NESS presents greater challenges primarily due to the complexities of designing efficient yet interpretable quantum reservoirs. Nevertheless, there is a straightforward and reliable method exploring quantum transport

within the GKSL framework: utilizing local dissipators that exclusively affect the edges of the system (Fig. 1.1). This approach is similar to the one used in classical non-equilibrium lattice models [29,30]. The resulting boundary-driven GKSL equation establishes a robust NESS framework, free from issues such as the early-time positivity violation encountered in the Redfield equation. Additionally, this approach often simplifies the simulation of large systems consisting of hundreds of spins and sometimes permits exact solutions.

Boundary-driven open quantum systems provide an efficient framework for inducing temperature or magnetization differences across a specified region. In such scenarios, the system's dynamics is primarily governed by the dissipator $\mathcal{D}$ in Eq. (1.6), making the choice of $\mathcal{D}$ critical. Typically, $\mathcal{D}$ is constructed to emulate relevant physical processes or drive the system efficiently toward a NESS.

In a standard boundary-driven setup for spin-1/2 systems, baths are coupled to the system at the first site ($i = 1$) and the last site ($i = L$), leading to a local master equation:

$$\mathcal{D}_i(\rho) = \gamma_i(1 - f_i)D[\sigma_i^-](\rho) + \gamma_i f_i D[\sigma_i^+](\rho), \tag{1.7}$$

where D represents a Lindblad dissipator:

$$D[L_\mu](\rho) := L_\mu \rho L_\mu^\dagger - \frac{1}{2}\left\{L_\mu^\dagger L_\mu, \rho\right\}. \tag{1.8}$$

Here, γ_i denotes the bath coupling strength at site i, and $f_i = 1/(e^{\beta h} + 1)$ represents the Fermi-Dirac distribution with inverse temperature β and energy unit h. Assuming that the boundary sites are uncoupled to the rest of the system, the dissipator Eq. (1.7) drives them to the thermal

states of the Hamiltonian $H = -h\sigma^z/2$ with a rate γ_i. In general, the resulting steady-state typically deviates from the intended bath-induced state due to a complex interplay between the bath driving and the Hamiltonian couplings. However, thermalization generally occurs in regions far from the boundaries, enabling the determination of thermodynamic parameters describing local equilibrium from local observables [31, 32]. It's noteworthy that while the typical single-site bath setup yields CPTP dynamics, it may not faithfully replicate the behavior of standard thermal baths. Nevertheless, the bulk conductivity or transport properties should be independent of the specific driving mechanism in the thermodynamic limit, provided that the dynamics is sufficiently ergodic.

To investigate finite temperature transport, the single-site driving method previously outlined can be extended to encompass multiple sites. This extension should be at least two sites for effectively coupling to the energy density, which is thus indispensable for studying energy transport. [31,33–35]. Analogous to the magnetization bath, a straightforward approach for finite temperature transport with a two-site bath utilizes a Gibbs state for the bath. More specifically, the Lindblad dissipator can be parametrized as $D(\rho) = \sum_{i,j} \gamma_{ij}(L_i \rho L_j^\dagger - \frac{1}{2}\left\{L_j^\dagger L_i, \rho\right\})$, with jump operators L_j acting solely on the two sites involved. In this expression, the matrix γ_{ij} adjustment results in the desired condition–the fixed point of $D(\rho)$ is given by the Gibbs state ρ_T on the two sites. Importantly, the choice of γ_{ij} is not unique due to its larger dimension than that of the thermal state, enabling the design of a more efficient dissipator in various ways. For example, all the excited modes of the bath operator can decay at the same rate, thereby achieving faster relaxation to the steady state. [33]. Alternatively, the rates can be selected to satisfy the detailed-balance condition, thereby enhancing performance by producing states closer to the thermal state at lower temperatures [35].

Provided that two conditions are fulfilled—namely, that the fast oscillatory terms do not significantly impact the dynamics and that the system is under the weak system-bath coupling limit—thermalization using a Gibbs state bath within the GKSL formalism can be validated. However, it is essential to note that this formalism only ensures positivity, and as a result, the resulting dynamics may not always be entirely physically accurate [36]. Commonly, these techniques can encounter slow convergence to the steady state if the open system dynamics are not appropriately designed. For instance, the resulting local GKSL equation may sometimes fail to accurately describe the correct steady state, as observed in integrable systems [31, 37], in the presence of multiple baths [38, 39], and even for the weak coupling limit [40–44].

Understanding the thermalization processes induced by the baths is crucial for evaluating their efficacy and analyzing the resulting steady state in relation to a thermal state while considering local equilibrium. A common method to assess the consistency of this approach involves coupling the chain to two baths at the same temperature and investigating the resulting steady state to check its resemblance to a thermal state. It is crucial to note that the steady state may not exhibit characteristics of a thermal state, depending on the specific bath. Notably, the magnetization bath Eq. (1.7) fails to achieve proper thermalization of the system when two baths possess identical thermal parameters, $f_1 = f_L$, leading to a non-zero expectation value for bulk magnetization, contrary to the thermal state $e^{-\beta H}$. Furthermore, these identical thermal parameters predict uncorrelated local sites, a deviation from the conditions of a thermal state [45].

On the other hand, the two-site bath with a Gibbs state fixed point yields improved thermalization, bringing the resulting steady state closer to a thermal state. While the specifics of the thermalization process may depend on the Hamiltonian parameters, the steady state generally approaches towards a thermal state at a temperature higher than the bath temperature. This dif-

ference diminishes at high bath temperatures, resulting in a better convergence to a thermal state. In addition, achieving a thermal state is influenced by the system size, with lower temperatures necessitating a substantially larger system size to achieve similar proximity to a thermal state. An approach to quantify the proximity between the resulting steady state and a thermal state involves computing the expectation values of various observables and verifying their consistency with those in the corresponding thermal state. This method also establishes an effective temperature for each observable. Furthermore, it is observed that the dispersion in expectation values becomes smaller at higher temperatures and for observables with smaller support sizes [34, 35]. This indicates that while the resulting steady state may locally resemble a thermal state, representing a global thermal state presents challenges.

Another important question in the context of finite temperature transport is whether boundary driving can thermalize the system to arbitrarily low temperatures. Previous investigations [46] have addressed the issue of thermalization in open quantum systems, exploring both interacting and non-interacting fermionic systems with particle number conservation. Perturbative expansions in the limit of zero system-bath coupling indicate that both models may achieve thermalization when the baths are infinitely large and weakly damped. Building upon these insights in our prior work [4], we extend these observations to various strongly interacting spin chains whose steady states admit a tensor network representation. In this context, a larger bath, resembling the thermal states of the system's Hamiltonian with controllable damping parameters, is coupled to the systems at their boundary. Under these settings, the system achieves thermalization even at low temperatures, provided the bath is sufficiently large, weakly coupled to the system, and infinitely damped, consistent with previous findings [46]. Within this multi-site bath framework, the final temperature of the NESS is estimated using a thermometry technique [47]. However,

the system's effective temperature typically exceeds that imposed by the bath. This imperfect thermalization implies that the primary limiting factor within the boundary-driven configuration is the minimal temperature threshold at which the baths can no longer efficiently cool the system within computationally accessible time scales. It is conceivable that this threshold might be determined by the smallest energy scale within the problem – either the model's gap or its interaction strength.

1.2.3 Properties of Boundary-driven Open Quantum Systems

Scaling Analysis

We focus on the transport of conserved quantities Q, which satisfies $[Q, H] = 0$ and are expressed as $Q = \sum_i q_i$, where q_i denotes the corresponding local quantity. In bulk where system obeys a unitary evolution, the local current operator $\hat{j}_i$ can be obtained from the Heisenberg equation of motion and the discretized continuity equation. It follows that the NESS current can be calculated by $j_i = \mathrm{tr}\left[\rho_\infty \hat{j}_i\right]$. By virtue of the continuity equation, the current j is independent of the lattice site i. For systems exhibiting normal diffusion, the current can be phenomenologically modeled by the famous Fourier's law $j = -D\Delta\mu/L$, where $\Delta\mu$ is the difference in driving potentials, and D is a diffusion constant. In particular, low-dimensional systems often deviate from the conventional Fourier's law, thus exhibiting anomalous transport characterized by nontrivial power-law scaling, given by

$$j \sim \frac{1}{L^\gamma}. \tag{1.9}$$

Depending on γ, various anomalous transport regimes can arise: (i) diffusive transport for $\gamma = 1$, (ii) ballistic transport for $\gamma = 0$, (iii) superdiffusive transport for $0 < \gamma < 1$, and (iv) subdiffusive

transport for $\gamma > 1$. In addition, γ approaching infinity can be regarded as localization from a practical standpoint. Comprehending the conditions for such various transport regimes is one of the main challenges in theoretical physics.

Relationship to Linear Response Theory

A crucial objective in the study of quantum transport is to establish a correlation between phenomenological laws and microscopic theories. The predominant and natural approach for analyzing transport in interacting one-dimensional systems is to apply linear response theory, which examines the system's response to an additional perturbation in the Hamiltonian.

To illustrate the linear response expression, let's delve into a simple classical scenario. Imagine a particle with a position denoted by $x(t)$, and a variance $d^2 := \langle x^2(t) \rangle$ over ensembles. In terms of the velocity, the variance can be expressed as $d^2 = \int_0^t \int_0^t \langle v(t_1) v(t_2) \rangle dt_1 dt_2$. In a stationary state reached after a long time, this correlation function depends only on the time difference, resulting in the variance

$$d^2 \to \int_0^t 2(t - t') \langle v(t') v(0) \rangle dt'. \tag{1.10}$$

This variance serves as an indicator of the particle's diffusion process and the diffusion constant is given by an integral of an autocorrelation function of the velocity–current of the position.

Now, let's consider an analogous argument in the quantum realm. When a system is under a weak perturbation, the total Hamiltonian becomes $H = H_0 - A\phi(t)$, where A is the operator coupled to the driving field $\phi(t)$. For example, in the context of energy transport, we have $(\dot{A}_E, \phi_E) = (\hat{j}_E, T\nabla(1/T))$, and for spin transport with the magnetic field b, we consider

$(\dot{A}_S, \phi_S) = (\hat{j}_S, -T\nabla(b/T))$. Within this framework, our objective is to calculate the expectation value of the operator $B(t)$ with respect to the state $\rho(t)$. Decomposing the density matrix into $\rho(t) = \rho_0 + \delta\rho(t)$, the Heisenberg equation of motion yields the following expression

$$\delta\rho(t) = -i \int_0^t d\tau e^{-i(t-\tau)H_0}[\rho_0, A]e^{i(t-\tau)H_0}\phi(\tau). \tag{1.11}$$

Assuming the local equilibrium, it follows that the expectation value of an operator B under the linearized dynamics is given by

$$\langle B(t)\rangle = \langle B\delta\rho(t)\rangle = -i \int_0^t d\tau \langle [\rho_0, A]B(t-\tau)\phi(\tau)\rangle, \tag{1.12}$$

where $\langle \bullet \rangle = \text{tr}[e^{-\beta H_0}\bullet]/Z$ and $Z = \text{tr}[e^{-\beta H_0}]$. For $\rho_0 = e^{-\beta H_0}$, it follows that $[\rho_0, A] = i\int_0^\beta d\lambda e^{-(\beta-\lambda)H_0}\dot{A}e^{-\lambda H_0}$. Using this expression, the expectation value becomes

$$\langle B(t)\rangle = \beta \int_0^t d\tau \langle \dot{A}|B(t-\tau)\rangle\phi(\tau), \tag{1.13}$$

where

$$\langle A|B\rangle := \frac{1}{\beta}\int_0^\beta d\lambda \langle Ae^{-\lambda H_0}Be^{\lambda H_0}\rangle \tag{1.14}$$

defines the Kubo inner product. The current is then found by setting $\dot{A} = B = \hat{j}$:

$$j(t) = \langle \hat{j}(t)\rangle = \beta \int_0^t d\tau \langle \hat{j}(0)|\hat{j}(t-\tau)\rangle\phi(\tau). \tag{1.15}$$

Utilizing the Fourier transform $j(t) = \frac{1}{2\pi}\int_{-\infty}^{\infty} d\omega e^{-i\omega t}j(\omega)$, the frequency space expression of

the current can be obtained: $j(\omega) = \kappa(\omega)\phi(\omega)$. In the thermodynamic limit, the desired transport coefficient $\kappa(\omega)$–typically conductivity–can be expressed as an autocorrelation function of the current, similar to the classical case:

$$\kappa(\omega) = \beta \lim_{t\to\infty} \lim_{L\to\infty} \frac{1}{L} \int_0^t e^{i\omega\tau} \langle \hat{j}(0) | \hat{j}(\tau) \rangle d\tau. \tag{1.16}$$

Establishing a rigorous mathematical connection between transport coefficients obtained from linear response theory and those from phenomenological macroscopic laws remains a general challenge. These two coefficients can be related in a well-defined setup for a very limited case. In the zero-frequency limit—the longest wavelength modes often representing hydrodynamic behavior—and with a vanishing singular part of κ, the spin diffusion constant at infinite temperature for the diffusive case can be obtained in the form of the current autocorrelation function:

$$D = 4 \lim_{t\to\infty} \lim_{L\to\infty} \frac{1}{L} \int_0^t \langle \hat{j}(0) | \hat{j}(\tau) \rangle d\tau. \tag{1.17}$$

Linear response theory is limited to sufficiently small driving fields. Even with such small perturbations, validating the theory can be challenging. The condition $t \to \infty$ in estimating transport coefficients implies that microscopic evolution can become unstable under the small driving limit. However, stable macroscopic behavior can be expected if the system possesses good thermalization properties and sufficiently chaotic microscopic dynamics. For example, in the regime of weak driving, there has been a quantitative agreement between the Lindblad approach and unitary Green-Kubo type linear-response calculations of the diffusion constant in chaotic models [48, 49].

Similarly, one can juxtapose the GKSL master equation approach with non-dissipative dynamics in an out-of-equilibrium scenario. For a meaningful comparison, it is imperative to concentrate on mutually assessable parameters via both methodologies, such as the diffusion constant or the scaling exponent. Under the assumption of a single-exponent scaling, the scaling exponents from these two methods are connected with the relation [50]

$$\alpha' = \frac{2}{\gamma + 1}. \tag{1.18}$$

Here, α' is another scaling exponent derived from the domain-wall spreading in a bipartitioning protocol. Although the same scaling exponent is generally observed [51, 52] for non-diffusive systems, the fundamental relationship between the NESS and the non-dissipative approaches is less evident.

Transport Properties and Depahsing

Transport in a noisy environment can be achieved by implementing dephasing baths on all system sites. When the dephasing strength Γ significantly outweighs other scales within the system, the current is expected to be governed by the expression:

$$j(\Gamma, L) = \frac{c_{deph}}{\Gamma L}. \tag{1.19}$$

Here, c_{deph} represents a constant factor. This result is intimately linked to the analytical solution of a uniform tight-binding chain, expressed by the formula $j \sim a/(b + \Gamma L)$, wherein a and b represent constants depend on the energy scales associated with both the bath and the sys-

tem [45]. In cases where the parameter Γ is a moderate value, there exists an interplay between the Hamiltonian—responsible for the system's inherent transport behavior $j \sim 1/L^{\gamma}$—and the dephasing mechanism—which inclines towards diffusive transport $j \sim 1/L$. Consequently, a characteristic length scale denoted by L_{Γ} emerges, implying the point of transition from one transport regime to another [53]:

$$j(\Gamma, L) = \begin{cases} c_0/L^{\gamma} & L \ll L_{\Gamma} \\ c_{\Gamma}/L & L \gg L_{\Gamma}, \end{cases} \tag{1.20}$$

where c_0 and c_{Γ} denote constants, with the former independent of Γ.

When L is sufficiently large ($L \gg L_{\Gamma}$), diffusive transport is anticipated, displaying a non-trivial dependence on the parameter Γ:

$$j(\Gamma, L) = \begin{cases} c_0 \Gamma^{(\gamma-1)/(\gamma+1)}/L & \Gamma \text{ small} \\ c_{deph}/L\Gamma & \Gamma \text{ large.} \end{cases} \tag{1.21}$$

The energy scales characterizing the system's Hamiltonian broadly differentiate these two expressions. This tendency is inferred from empirical observations across noninteracting and interacting models employing diverse potential settings [54–60]. Notably, despite the diffusive transport induced by the dephasing, the exponent γ characterizing the dephasing-free system continues to exert a discernible influence.

1.3 Tensor Network Approaches for Accessing NESS

Indeed, various strategies exist for solving the GKSL master equation to address the dynamics of open quantum systems. Despite its inherent complexity, exact solvability is achievable in certain cases. Notable instances include non-interacting models [61, 62], and the pure-dephasing spin-boson model [63, 64]. Additionally, some integrable models can be analytically treated using methods such as the Bethe ansatz [61, 65–68] or a field-theoretical description within the Keldysh formalism [69]. However, these exactly solvable models are severely limited, especially when considering a broad spectrum of models reflecting real materials, many of which feature perturbation terms that disrupt integrability. Consequently, it is a common strategy to employ assorted numerical methods for solving such complicated problems, particularly when considering generic interacting systems.

Despite the variety of approaches available for studying the dynamics of boundary-driven open quantum systems, not all methods are equally efficient, and many suffer from notable drawbacks, particularly in transport simulations. For instance, the quantum trajectories approach, which involves stochastically evolving wavefunctions instead of directly solving the master equation, can encounter sampling problems from Monte Carlo techniques. Similarly, perturbation theory is constrained to the weak coupling limit, limiting its applicability in certain scenarios. Other methods, such as exact-type approaches (such as diagonalization and quantum typicality) or variational-type approaches (including neural networks), encounter scalability limitations. However, tensor network approaches emerge as the most promising direction among computational methods to address these challenges and achieve scalability, particularly toward accessing the near thermodynamic limit. This section discusses the most relevant types of tensor networks

and their potential applications in overcoming the difficulties encountered in transport simulations.

1.3.1 Matrix Product State Ansatz

When considering the dynamics of one-dimensional open quantum systems, tensor network methods have emerged as the most efficient approach for decades. These methods aim to capture the "physical corner" of the Hilbert space to approximate the most relevant quantum states for describing the dynamic evolution. To be precise, let us consider a quantum spin system governed by a local Hamiltonian whose ground state is denoted as $|\psi\rangle$. Bipartitioning $|\psi\rangle$ into two connected regions, A and B, results in corresponding reduced density matrices ρ_A and ρ_B, respectively. Then, the entanglement entropy $S(\rho_A) = -\operatorname{tr}[\rho_A \log(\rho_A)] = S(\rho_B)$ measures the quantum correlations between these regions. In most cases, the strongest correlations occur between the nearest neighboring spins, which are forced to interact by the local Hamiltonian. This observation suggests that the entanglement between two regions of a large system is directly proportional to the surface area separating them. This phenomenon is termed the area law for entanglement entropy [70]. In contrast to the volume law exhibited by random states in Hilbert space, atypical quantum states adhering to an area law for entanglement entropy hold exceptional significance due to their effective representations using tensor networks. It is known that the area laws can rigorously be demonstrated for non-interacting bosonic [71] and fermionic systems [72, 73]. However, proving valid area laws for interacting systems generally poses a greater challenge. Nonetheless, research suggests that the NESS of open quantum many-body systems, induced by Markovian evolution, exhibit the area law entanglement, quantified through measures

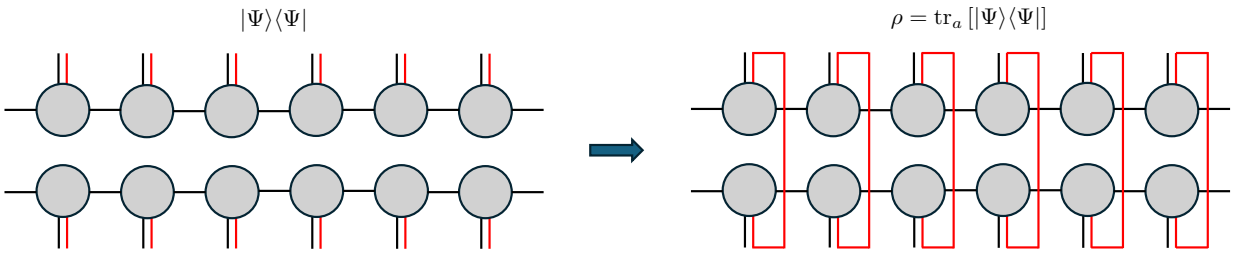

Figure 1.2: Purification: an MPS $|\Psi\rangle$ is defined in an enlarged Hilbert space using ancillas and tracing out them from the projector $|\Psi\rangle\langle\Psi\rangle$ to obtain the MPDO ρ.

such as mutual information [74].

In transport studies, which necessitate large systems and long time scales, it is crucial that a NESS accepts an efficient tensor network representation. A preferred method within the tensor network family for this direction is a variant of the time-dependent density matrix renormalization group (t-DMRG) [33]. t-DMRG offers the advantage of enabling the selection of system sizes large enough to reach the thermodynamic limit effectively, thanks to a finite effective speed of information propagation [75]. Furthermore, it is not constrained to integrable models or translationally invariant cases. This method is employed to evolve $\rho(t)$ over time, usually by the time-evolved block decimation (TEBD) algorithm [76], until reaching the NESS. After obtaining the NESS, the NESS current is calculated as the expectation value of the current operator with respect to the NESS. Approaching the near thermodynamic limit, the NESS current plays a key role in evaluating the system's transport properties—the NESS current scales with system size, facilitating the classification of transport behavior. While several mixed state simulation techniques exist, two formalisms emerge as prominent methods for practically accessing NESS across diverse open quantum system configurations [77–80].

Most t-DMRG family algorithms rely on the matrix product state (MPS) framework. An

MPS representing a total of L sites is formulated as follows:

$$|\psi\rangle = \sum_{s_1,\cdots,s_L=1}^{d} A_1^{s_1} \cdots A_L^{s_L} |s_1, \cdots, s_L\rangle, \tag{1.22}$$

where the A matrices' dimensions are determined by the bond dimension χ, and d is the physical dimension of the Hilbert space. In the context of t-DMRG for GKSL equations, this concept must extend to matrix product density operators (MPDOs), akin to pure states. The key distinction is that the local Hilbert space dimension in the operator space equals the square of the pure state dimension. An MPDO ρ for L d-local Hilbert space particles with $(D_1, D_2, \cdots, D_L)$-dimensional bonds is defined as follows:

$$\rho = \sum_{s_1,s_1',\cdots,s_L,s_L'=1}^{d} M_1^{s_1,s_1'} \cdots M_L^{s_L,s_L'} |s_1, \cdots, s_L\rangle\langle s_1', \cdots, s_L'|, \tag{1.23}$$

where

$$M_k^{s_k,s_k'} = \sum_{a=1}^{d_k} A_k^{s_k,a} \otimes (A_k^{s_k',a})^*. \tag{1.24}$$

This construction of MPDOs inherently ensures the positivity of the reduced density matrix ρ. Alternatively, ρ can be expressed through a purification process. In such a process, a pure state MPS Ψ residing in an enlarged Hilbert space by the ancillary degree of freedoms, corresponding to the original density matrix ρ, is defined as follows:

$$|\Psi\rangle = \sum_{s_1,\cdots,s_L} \sum_{a_1,\cdots,a_L} A_1^{s_1,a_1} \cdots A_L^{s_L,a_L} |s_1 a_1, \cdots, s_L a_L\rangle. \tag{1.25}$$

Then ρ can be obtained by tracing over the ancillary degree of freedoms, $\rho = \mathrm{tr}_a\left[|\Psi\rangle\langle\Psi|\right]$ (Fig.

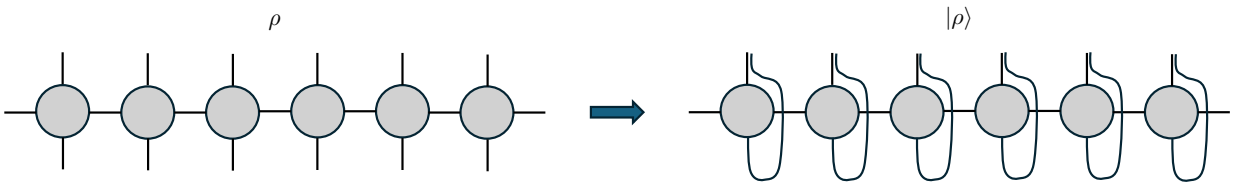

Figure 1.3: Vectorization: vectorizing a MPDO by merging its two physical tensor indices into one large physical tensor index, which is equivalent to the Choi-Jamiolkowski isomorphism.

1.2). While the positivity of ρ is secured through the purification process, it's important to note that local purification techniques can often be more computationally intensive than the MPDO form itself [81].

Another method for investigating mixed state dynamics employs the MPS ansatz in conjunction with the concept of Choi-Jamiolkowski isomorphism [82,83]. The isomorphism involves a mathematical manipulation that transforms a bra index into a ket index for a density matrix, representing the coefficients of ρ in a vectorized form denoted by $|\rho\rangle$. Once vectorized, $|\rho\rangle$ is in $\mathbb{C}_{d^2}^{\otimes L}$, and the master equation can be expressed in the corresponding vector form (Fig. 1.3). Explicitly, the resulting mixed state can be represented as follows:

$$|\rho\rangle = \sum_{s_1=0}^{d^2-1} \cdots \sum_{s_L=0}^{d^2-1} c_{s_1,\cdots,s_L} |s_1\rangle \otimes \cdots \otimes |s_L\rangle, \tag{1.26}$$

where $|s_i\rangle$ now represents an orthonormal basis of the extended Hilbert space $\mathbb{C}_{d^2}^{\otimes L}$.

In instances where the Liouvillian super-operator $\mathcal{L}$ can be decomposed into nearest neighbor terms at most, $\mathcal{L}[\rho] = \sum_l \mathcal{L}_{l,l+1}[\rho]$, it is possible to consider the utilization of the conventional TEBD algorithm, which involves a two-site nearest-neighbor transformation. The TEBD algorithm involves discretizing the time evolution operator $e^{\mathcal{L}t}$ into multiple small time step operators $e^{\mathcal{L}\delta t}$ up to a tolerable order of error, through the employment of the Trotter-Suzuki decomposition [84, 85]. These operators are then applied to the initial density operator until it converges to

the desired NESS.

1.3.2 Accuracy of NESS Simulations

Two factors primarily determine the efficiency and accuracy of t-DMRG family simulations for the GKSL equations. Firstly, the truncation error occurs when representing the NESS with a finite-bond MPDO by setting a bond dimension threshold to discard less significant components. Generally, the bond dimension required to maintain consistent truncation per time step tends to increase exponentially over time [86]. This can potentially limit the accessible time scales, typically spanning several powers of the inverse energy unit. Therefore the truncation process mitigates excessive entanglement growth [87]. The magnitude of the truncation error is related to the operator space entanglement [88] of the resulting NESS $\rho_\infty = \sum_k \sqrt{\lambda_k} A_k \otimes B_k$, where λ_k are non-negative coefficients (with $\sum_k \lambda_k = 1$) obtained via the Schmidt decomposition. However, the optimal process is eventually disrupted by the non-unitarity of the dynamics, necessitating periodic reorthogonalization of the evolving state along with bond dimension truncation [32]. In general, dissipative dynamics are expected to exhibit less severe entanglement growth compared to pure state simulations, hence a smaller bond dimension suffices [33]. For instance, when a small magnetization μ is applied, one typically observes the Schmidt spectrum λ_k scales asymptotically as $\mu^2 L^r / k^p$ for large values of k. The specific power-law exponents r and p, which rely on the model, play a crucial role in determining the extent of truncation error, and consequently, the necessary bond dimension χ. The Schmidt spectrum provides a reliable estimation of error without additional fitting parameters, particularly when assessing the actual error of the NESS current. Additionally, different initial states should converge to the same unique NESS. Numer-

ical errors resulting from a fixed bond dimension simulation should not significantly impede the system's convergence to the correct NESS, at least to some degree.

The other crucial parameter is the time required for the system to reach the NESS, which is determined by the inverse gap of the Lindbladian super-operator $\mathcal{L}$. In the case of the spin-1/2 Heisenberg model, this time scales approximately as $\sim L^3$ [89]. Consequently, the computational complexity of achieving NESS with a fixed precision $\chi \sim L$ scales as $L^3 \cdot L \cdot \chi^3 \sim L^7$. If the decay of the Schmidt spectrum λ_k is slower than $1/k^2$, as is often the case, the required bond dimension will scale even worse [33]. Nonetheless, for sufficiently (or infinitely) high-temperature simulations, when the NESS closely resembles a product operator close to identity, the method generally performs well because high temperatures tend to reduce entanglement [88]. However, for very slow transport scenarios such as strongly subdiffusive dynamics, a very long convergence time to the steady state might pose a challenge, making the open quantum system framework less appropriate.

1.3.3 MPS for Finite Temperature Transport Simulations

Transitioning from high (infinite) temperature to low (finite) temperature dynamics using tensor network machinery presents a significant challenge. The concept of the MPDO is indispensable for describing mixed state dynamics. The thermal density matrix $\rho = e^{-\beta H}/Z$—$Z = \sum_n e^{-\beta E_n}$ is the partition function—assumes the form of an MPDO, defined by a partial trace over a pure state residing in an enlarged Hilbert space. In this framework, ancillary degrees of freedom encode the thermal bath, as highlighted in previous studies [78, 87, 90, 91]. Typically, the purification process involves the analytical representation of the infinite temperature ($\beta = 0$)

state $\rho = 1/Z = 1/N$, where N is the dimension of the Hilbert space. A common strategy is entangling each physical degree of freedom with its counterpart in the bath, thereby establishing a maximally entangled state between them. Subsequent imaginary time evolution, where the Hamiltonian H exclusively affects the physical degrees of freedom, is performed using standard DMRG time evolution techniques. The goal of this process is to yield a purified version of the thermal state ρ at any desired finite temperature. Thermal expectation values are derived by tracing over the auxiliary degrees of freedom. This approach provides a systematic methodology of exploring quantum systems at finite temperatures within the DMRG framework.

Indeed, both imaginary and real-time evolutions, along with the trace operation, are linear operations. This enables the calculation of multiple operations in arbitrary order to streamline computational procedures. For instance, correlation functions can be computed using the formula:

$$\langle A(t)B\rangle = \langle \Psi_0 | e^{-\beta H/2} U^\dagger(t) A U(t) B e^{-\beta H/2} | \Psi_0 \rangle, \tag{1.27}$$

where the MPS $|\Psi_0\rangle$ purifies the thermal state at infinite temperature. If the Hamiltonian being considered comprises solely short-ranged interactions, both the real and imaginary time evolutions in this equation can be directly computed using the TEBD algorithm [76, 79]. For non-zero β, entanglement growth occurs in ancillary degrees of freedom. As this entanglement lacks any physical entity, one can select a purification–which is not uniquely determined up to an arbitrary unitary–with minimal entanglement. This choice allows the resulting time evolution to access a longer time scale [92, 93]. Additionally, a practical method exists for finding the minimally entangled representation by iteratively minimizing the second Renyi entropy [94]. Furthermore, rewriting $\langle A(2t)B\rangle = \langle A(t)B(-t)\rangle$ in Eq. (1.27) so that the same formalism can access larger

time scales, typically by a factor of two or less [91]. Typically, the finite temperature t-DMRG algorithms can be used to determine Drude weights and diffusion constants by accessing the long-time limit of the current correlation function [92, 95–97] or from local quenches [98, 99] as well as in the bipartitioning protocol [100, 101]. In conclusion, the primary objective of such development is to reduce the accumulation of entanglement, thereby extending the simulation time.

Other methods for incorporating finite temperatures within DMRG include a Lindbladian super-operator approach [80], a transfer-matrix formulation [102], or probabilistic sampling over pure states [103]. These various approaches offer flexibility and efficiency in studying quantum systems at finite temperatures within the DMRG framework. However, their performance diminishes as the temperature decreases, given that relevant time scales and finite-size effects substantially increase as the temperature lowers from infinity.

1.3.4 Improving the Performance of NESS Simulations

Exploring the ways to enhance algorithmic efficiency is also important when dealing with tensor network simulations. It is often challenging to investigate large and strongly interacting systems for a long time with desired accuracy.

One notable improvement entails incorporating symmetries, particularly the conservation of quantum numbers such as total particle number or total magnetization. In general, there are two main obstacles when applying this concept to open quantum systems: quantum numbers are now in both the bra and ket components of the density matrix, and the dissipators typically change the conversation laws. To address this challenge, a scheme that dynamically adjusts to

fluctuations in quantum numbers was introduced [104].

Parallelization of the application of the time evolution operator to the MPS, alternating between even and odd bonds, has demonstrated efficacy in bolstering performance [86]. Importantly, this parallelization scheme preserves the canonical structure of the MPS, enabling a concurrent reduction in local bond dimensions. Similarly, one can divide the time evolution sweeping process into multiple segments across the system [105, 106]. These segments can then be distributed across different computational nodes, with nodes communicating once they converge at their shared bond.

Furthermore, recent research has unveiled an intriguing method wherein a mapping from alternative geometrical configurations to the linear chain can augment simulation performance by reducing the bond dimension [107–109].

1.4 Structure of the Thesis

Building upon the foundational materials in Chapter 1, this dissertation presents three distinct scenarios regarding the dynamics of boundary-driven open quantum systems. Across these scenarios, the focus is on exploring the transport properties of the one-dimensional spin systems in non-equilibrium steady states. Within this framework, the analysis delves into various properties of NESSs, including entanglement structures, symmetry-based attributes, and perspectives on thermalization. These explorations are made feasible through the employment of novel and efficient computational approaches—an additional cornerstone of this thesis.

In Chapter 2 (based on the publication 'Nonequilibrium steady state phases of the interacting Aubry-André-Harper model' by Yongchan Yoo, Junhyun Lee, and Brian Swingle, published

as Phys. Rev. B 102, 195142 (2020)), the NESS phases and entanglement structure of the interacting Aubry-André-Harper (AAH) model are discussed. This model is renowned for its diverse dynamical phases stemming from the quasi-periodic disorder. The investigation into spin transport in this model involves analyzing the scaling exponents of the NESS spin current, which remains highly challenging even with the aid of the effective boundary-driven open quantum system framework. Furthermore, the decay of quantum mutual information (QMI) also reveals several distinct regimes based on the strength of the quasi-periodic potential. However, we suspect that these regimes may be delineated by crossovers rather than true phase transitions.

In Chapter 3 (based on the publication 'Open-system spin transport and operator weight dissipation in spin chains' by Yongchan Yoo, Christopher David White, and Brian Swingle, published as Phys. Rev. B 107, 115118 (2023)), we investigated NESSs of boundary-driven open quantum systems to explore how the operator weight dissipation influences the scaling behavior of transport in several different spin models of the XXZ family—spanning chaotic, integrable, and Anderson localized flavors. We revealed that operator weight dissipation tends to drive the system towards diffusive transport scaling unless it conserves fundamental symmetry or a conserved quantity of the underlying dynamics. This result aligns with the premise of the effective field theory in hydrodynamics, which posits that a system's dynamics is primarily characterized by its symmetries and related conservation laws up to certain $O(1)$ factors. Indeed, our findings regarding the isotropic point of the XXZ model, where superdiffusion persists despite operator-weight dissipation, suggest a more intricate interplay between the dynamical properties and the symmetry of the underlying Hamiltonian.

In Chapter 4 (based on the publication 'Temperature dependence of energy transport in the $\mathbb{Z}_3$ chiral clock model' by Yongchan Yoo and Brian Swingle, published as Phys. Rev. B 109,

235104 (2024)), we investigated finite temperature energy transport in the non-integrable $\mathbb{Z}_3$ chiral clock model with the multi-site thermal bath technology. In the high-temperature regime, we consistently observed the diffusive energy transport across different model parameters, as anticipated within the non-integrable regime. This finding supports our hypothesis that low-temperature physics does not directly influence high-temperature transport phenomena. Furthermore, we focused on a quantum critical point at zero temperature to investigate the temperature dependence of transport coefficients. Configuring the multi-site bath enables access to transport behavior at lower temperatures, which are comparable to the model's characteristic energy scale. In addition, the diffusion constant obtained at this phase diagram point exhibits good agreement with a power-series expansion in terms of inverse temperature.

In Chapter 5, the outlook and possible future directions of the entire theme of this thesis is presented.

Chapter 2: Non-Equilibrium Steady State Phases of the Interacting Aubry-André-Harper Model

This chapter is based on the publication 'Nonequilibrium steady state phases of the interacting Aubry-André-Harper model' by Yongchan Yoo, Junhyun Lee, and Brian Swingle, published as Phys. Rev. B 102, 195142 (2020).

2.1 Overview

Here we study the phase diagram of the Aubry-Andre-Harper model in the presence of strong interactions as the strength of the quasiperiodic potential is varied. Previous work has established the existence of many-body localized phase at large potential strength; here, we find a rich phase diagram in the delocalized regime characterized by spin transport and unusual correlations. We calculate the non-equilibrium steady states of a boundary-driven strongly interacting Aubry-Andre-Harper model by employing the time-evolving block decimation algorithm on matrix product density operators. From these steady states, we extract spin transport as a function of system size and quasiperiodic potential strength. This data shows spin transport going from superdiffusive to subdiffusive well before the localization transition; comparing to previous results, we also find that the transport transition is distinct from a transition observed in the speed of operator growth in the model. We also investigate the correlation structure of the steady state and

find an unusual oscillation pattern for intermediate values of the potential strength. The unusual spin transport and quantum correlation structure suggest multiple dynamical phases between the much-studied thermal and many-body-localized phases.

2.2 Introduction

Developments in highly engineered quantum many-body systems have given unprecedented experimental access to controlled quantum many-body models. For a variety of model systems, it is now possible to observe quantum many-body dynamics over times long compared to the microscopic energy scales in the Hamiltonian. This influx of new experimental data has reinvigorated numerous conceptual questions in the foundations of the subject, including the conditions under which isolated quantum systems come to some kind of effective equilibrium state.

In this context, many-body localization (MBL) [10,11,110–121], corresponding to a failure to reach equilibrium, has received intense attention for the insights it brings to the foundations of quantum statistical physics. Many experimental investigations of localization physics in such systems have been carried out [117, 122–128], with the non-equilibrium relaxation dynamics of the system typically being probed by preparing a suitable initial state and evolving it in time. For example, if the system is initialized into an imbalanced state with more atoms on even than odd sites, monitoring the time-dynamics of the imbalance can reveal the onset of localization and the failure to thermalize.

From the experimental point of view, it has proven convenient to study localization in the context of so-called quasiperiodic systems [129–134]. These systems are typically formulated as lattice models subject to a periodic potential whose wavelength is incommensurate with the un-

derlying lattice. When the imposed potential is strong enough, the system is driven to a localized phase.

One important observation in systems with a quasiperiodic potential is anomalous transport characterized by a power-law in time spreading of the conserved particle number. This power law can be super-diffusive, often as a result of proximity to integrability, or sub-diffusive. While the emergence of sub-diffusive transport in random systems can be explained by Griffiths effects, the correlated nature of the on-site potentials in a quasiperiodic system precludes conventional Griffiths effects. There are a few theories to interpret the difference of the anomalous transport and localization in the quasiperiodic potential compared to the random potential [118], however, the physical origin is still unclear. Here our interest will be transport physics of one-dimensional spinless fermions evolving according to the interacting Aubry-Andre-Harper (AAH) model [135, 136].

Prior work with this model has suggested that as the strength of the quasiperiodic potential is increased, the system can enter an intermediate regime of slow dynamics before the fully localized state is reached [128, 137]. A few theories have been proposed to explain these anomalous dynamics, including local fluctuations of energy density [138] and atypical transition rates between the single-particle eigenstates [131]. However, the origin of the slow dynamics is still under debate. Moreover, the observed dynamical behavior raises the question of the possible existence of intermediate many-body phases. Recently, such a slow intermediate phase was claimed based on a numerical observation that the butterfly velocity, the speed at which Heisenberg operators spread in a chaotic system, vanished well before the full localization transition [133].

In this work, we study transport and entanglement properties of non-equilibrium steady states (NESS) of the interacting AAH model in the strongly interacting regime under the influence

of external baths coupled to the ends of the system [Fig. 2.2(a)]. Using a standard fermion-to-spin mapping, the AAH model is converted into a corresponding spin model. In the spin language, the conserved quantity of interest is the spin/magnetization in the z-direction. Using a tensor network method built upon a matrix product operator (MPO) ansatz for the density matrix, the steady states of the model at large size can be obtained by evolving a Gorini-Kossakowski-Lindblad-Sudarshan (GKLS) master equation [24, 25] close to its dynamical fixed point. By measuring the asymptotic scaling exponent characterizing magnetization transport, we show that there is a transition from superdiffusive transport to subdiffusive transport.

The existence of this transition is further supported by a study of out-of-equilibrium magnetization domain wall dynamics using a different tensor network method based on unitarily evolving an initial state without any baths present [Fig. 2.2(b)]. Interestingly, our data indicate that this transition before the point where the butterfly velocity vanishes. Hence, we conclude that as the quasiperiodic potential strength is increased, the system first experiences subdiffusive magnetization transport then experiences subballistic operator growth, and then finally reaches a fully localized state. These series of transition points are summarized in the phase diagram Fig. 2.1.

The entanglement and correlation structure of the NESS is explored by studying the two-site quantum mutual information (QMI). From the correlation pattern extracted from the QMI, we find that there are three distinctive regimes of potential strength, which are characterized by different decay trends in the QMI. For small values of the potential, the QMI decays approximately monotonically. As the strength increases, the system enters a regime showing strong modulation of the QMI with the same wavelength as the quasiperiodic potential. Interestingly, this modulation suddenly disappears at even larger potential strength, providing another indication that the

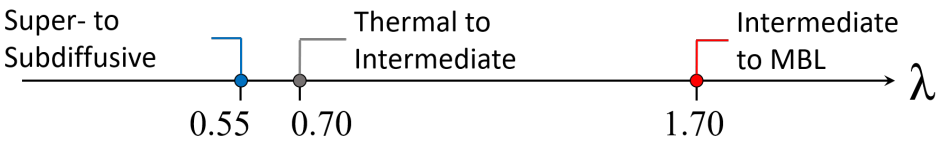

Figure 2.1: Transport phase diagram of the interacting AAH model as a function of quasiperiodic potential strength λ.

model supports very rich dynamics.

2.3 Model and methods

2.3.1 Models

We study the interacting AAH model with the following Hamiltonian [135, 136],

$$H = J \sum_{i=1}^{N-1} \left(\sigma_i^x \sigma_{i+1}^x + \sigma_i^y \sigma_{i+1}^y + U \sigma_i^z \sigma_{i+1}^z \right) + \sum_{i=1}^{N} h_i \sigma_i^z, \tag{2.1}$$

where σ_i's are the spin Pauli matrices at site i and U is the interaction strength. Units of time and energy are chosen such that $J = \hbar = 1$. The quasiperiodic potential is $h_i = 2\lambda \cos(2\pi\beta i + \phi)$, which is characterized by a strength λ and an irrational wave-number β.

Without the interaction ($U = 0$), the AAH model experiences a transition from a ballistic state to a fully localized state at $\lambda = 1$ [136]. Thus, a distinguishing feature of the localization transition in the non-interacting case is that the system has a sharp transition at a single quasiperiodic potential strength. Previous studies [132, 133, 137, 139] suggested that adding the interaction leads to various intermediate phases with slow dynamics.

It is notable that since Griffiths-type regions do not appear with the quasiperiodic potential [121, 140], the physical origin of slow intermediate dynamics in the interacting AAH model

should be distinct from models with random disorders. Here we study the physics of spin transport and correlation as a function of varying potential strength in the strong interaction regime, $U = 1.0$, with fixed irrational wave number $\beta = (\sqrt{5} - 1)/2$ and global phase $\phi = 0$.

2.3.2 Master equation and NESS

Our primary tool for investigating the spin dynamics is to study non-equilibrium steady states of long chains driven at the boundaries by Markovian baths. The Markovian time evolution of the open system is described by the GKLS master equation [24, 25]:

$$\frac{d\rho}{dt} = \mathcal{L}(\rho) \equiv i[\rho, H] + \sum_{\nu} \left(L_\nu \rho L_\nu^\dagger - \frac{1}{2} \left\{ L_\nu^\dagger L_\nu, \rho \right\} \right). \tag{2.2}$$

Here, ρ is the density matrix of the system and L_ν's are the Lindblad operators representing the baths with index ν. We consider single-spin baths at the two boundaries of the system ($i = 1,\ N$) with a chemical potential bias μ. The Lindblad operators then become $L_{1,\pm} = \sqrt{1 \pm \mu}\sigma_1^\pm$ and $L_{N,\pm} = \sqrt{1 \mp \mu}\sigma_N^\pm$. Note that $\sigma^\pm = \frac{1}{2}(\sigma^x \pm i\sigma^y)$. At infinite time, the solution of the GKLS equation can approach a steady state, and we attempt to access that steady state by evolving for a large but finite time. This distinction is important because, although we always evolve long enough for the state to be very slowly changing in time, the true infinite time steady state may nevertheless not be approximately reached, especially at larger values of the potential.

Technically, if the density matrix is mapped to a superket state $|\rho\rangle\rangle$ [80], the GKLS master equation takes a numerically practical form $\frac{d}{dt}|\rho\rangle\rangle = \mathcal{L}|\rho\rangle\rangle$ with the Liouvillian superoperator $\mathcal{L}$

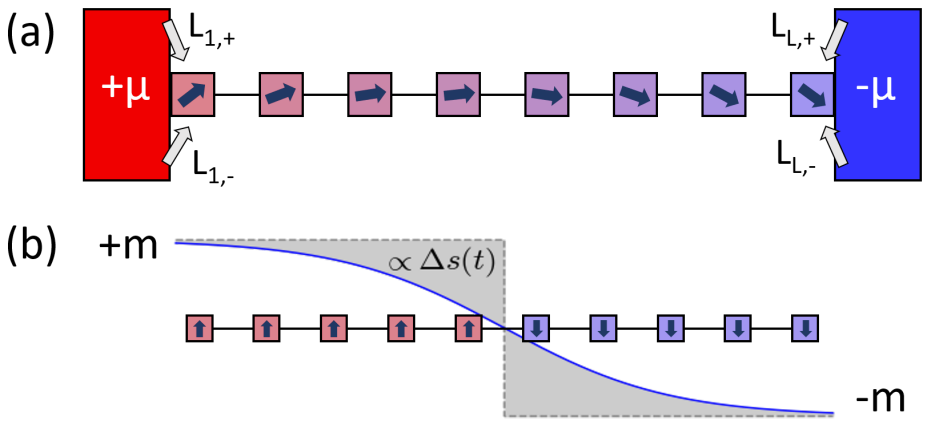

Figure 2.2: (a) Lindbladian setting and (b) unitary setting for numerical simulations. The blocks with chemical potential $\pm\mu$ [(a)] are baths in contact with the boundaries of the spin chains via Lindblad operators, L. Blue solid line [(b)] represents the magnetization at time t while the dotted lines are that on time $t = 0$.

as follows [141]:

$$\mathcal{L} = -iH \otimes \mathbb{I} + i\mathbb{I} \otimes H^T + \sum_\nu \left(L_\nu \otimes (L_\nu^\dagger)^T - \frac{1}{2} \left(L_\nu^\dagger L_\nu \otimes \mathbb{I} + \mathbb{I} \otimes (L_\nu^\dagger L_\nu)^T \right) \right). \tag{2.3}$$

The NESS (ρ_∞) is approximated by $|\rho(t)\rangle\rangle = e^{\mathcal{L}t}|\rho(0)\rangle\rangle$ for sufficiently large time t. It is known [33] that the NESS calculated from Eq. 2.3 is independent of the choice of initial state unless ρ_∞ and $\rho(0)$ have zero overlaps. We choose a product state $|\rho(0)\rangle\rangle = \prod_i e^{-\mu_i \sigma_i^z}$ as the initial state with μ_is linearly interpolating between the chemical potential bias ($\pm\mu$) at the two ends of the chain. Small bias is enough to measure the spin transport in this model while not perturbing the system too much; the calculations below take $\mu = 0.01$. This choice of initial state also appears to aid in a quick convergence to a quasi-steady state.

2.3.3 Numerical method: Tensor networks

In the superket-superoperator formalism, the density matrix and Liouvillian naturally map to a matrix product state (MPS) and matrix product operator (MPO), respectively. We choose the spin Pauli matrices σ^α ($\alpha = 0, x, y, z$) as a basis for the MPS and MPO (σ^0 is the identity matrix). For instance, the dissipative part of the Liouvillian superoperator has a simple 4×4 matrix representation in this basis. We then apply the time-evolving block decimation (TEBD) method [76, 142] to the Liouvillian superoperator equation ($|\rho(t)\rangle\rangle = e^{\mathcal{L}t}|\rho(0)\rangle\rangle$ and Eq. 2.3). First, we decompose the propagator $e^{\mathcal{L}t}$ into small time-steps, $e^{\mathcal{L}\Delta t}$, and also write the Liouvillian superoperator as $\mathcal{L} = \mathcal{L}_1 + \mathcal{L}_2$ using the Suzuki-Trotter decomposition [143], where $\mathcal{L}_1$ and $\mathcal{L}_2$ are sums of mutually commuting terms. The use of the Suzuki-Trotter decomposition is justified as the Liouvillian (both the Hamiltonian and the dissipative term) have at most nearest-neighbor couplings. We use the second-order Suzuki-Trotter decomposition and time steps as small as $\Delta t = 0.05$ in our numerical simulations.

For systems with large quasiperiodic potential (typically $\lambda \sim 1.5$), the relaxation time is very long due to the slow dynamics. To converge efficiently to the NESS in these cases, we choose different simulation parameters for the early and later stages of the time evolution, with the expectation that the intermediate time dynamics becomes irrelevant as the steady state is approached. At the early stage, a relatively small maximum bond dimension ($\chi = 32$) and a large time step ($\Delta t > 0.1$) are used to quickly drive the system into the rough neighborhood of the NESS. Then, during the remainder of the simulation, we carefully approach the NESS with a larger maximum bond dimension ($\chi = 128$) and a smaller time step ($\Delta t = 0.05$).

Expectation values of local observables ($\mathcal{O}$) are calculated as usual, $\langle \mathcal{O} \rangle = \mathrm{tr}(\mathcal{O}\rho_\infty)/\mathrm{tr}(\rho_\infty)$.

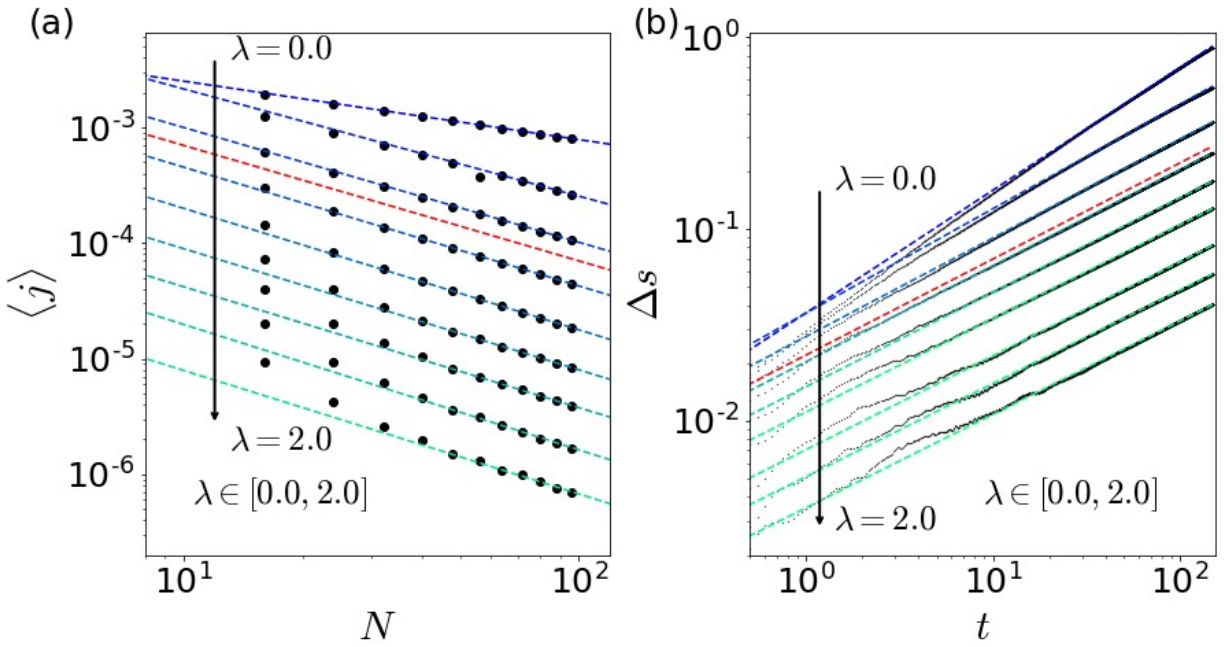

Figure 2.3: The spin transport of the interacting AAH model. (a) The average spin current $\langle j \rangle$ of the NESS for different quasiperiodic potential strengths as a function of the system size N. The dashed lines are the best asymptotic inverse power-law fittings. (b) The spread portion of the total magnetization Δs for different quasiperiodic potential strengths as a function of the time t. The gray dashed lines are the best asymptotic power-law fittings. The red dashed lines describe the diffusive transport scalings.

However, fluctuations are inevitably present in expectation values calculated from our approximate NESS, depending on the convergence. Therefore, throughout our numerical studies, we average over the expectation values of many successive Suzuki-Trotter time steps to effectively reduce the effect of fluctuations. For each observation, we monitor the convergence of the time-step averaged value and use an appropriate number of time-steps so that the result is converged. The number of sampling steps typically varies from 50 to 1000, depending on the simulation parameters of the model.

2.4 Spin transport

To observe different dynamical phases of the AAH model, we concentrate on the average spin current of the system in NESS as a function of the quasiperiodic potential strength λ. The spin current operator for the i-th bond is $j_i = 2(\sigma_i^x \sigma_{i+1}^y - \sigma_i^y \sigma_{i+1}^x)$; its expectation reaches an i-independent value (per the continuity equation) as the system approaches the NESS.

Diffusive transport is characterized by Fick's law, $\langle j \rangle = -D\, \partial_i \langle \sigma_i^z \rangle$, where D is the diffusion constant. The derivative can be approximated as $\frac{\langle \sigma_N^z \rangle - \langle \sigma_1^z \rangle}{N}$ in the NESS. This length dependence of $\langle j \rangle$ can be generalized to non-diffusive situations using a scaling exponent γ:

$$\langle j \rangle = -D \frac{\langle \sigma_N^z \rangle - \langle \sigma_1^z \rangle}{N^\gamma}. \tag{2.4}$$

$\gamma = 1$ corresponds to Fick's law of diffusive transport while $\gamma = 0$ indicates ballistic transport. Superdiffusive and subdiffusive transport correspond to $\gamma < 1$ and $\gamma > 1$, respectively.

In the boundary-driven spin chain we consider [Fig. 2.2 (a)], the boundary magnetization is constrained via the chemical potential imbalance $\langle \sigma_N^z \rangle - \langle \sigma_1^z \rangle \approx -2\mu$. Thus $\langle j \rangle \sim 1/N^\gamma$, and we can determine the exponent γ by directly observing how the spin current scales with the system size N. This analysis is shown in Fig. 2.3(a) which plots $\langle j \rangle$ as a function of N in logarithmic scale. A linear fit, where the magnitude of the slope gives γ, is obtained from a series of large N values ($N \geq 72$) to reduce finite size effects and to include the effect of self-averaging of ϕ. The increasing trend of γ with λ shows that the system experiences a transition from superdiffusive to subdiffusive transport as the quasiperiodic potential strength increases.

To further validate this result, we use a second method discussed in Ref. [132] to in-

vestigate the spin transport. In this approach, we eliminate the external baths at the boundary and observe the unitary evolution of a sharp domain wall. The initial state is $|\rho(0)\rangle\rangle \propto \prod_{i=1}^{N/2} e^{m\sigma_i^z} \otimes \prod_{i=N/2+1}^{N} e^{-m\sigma_i^z}$ (with appropriate normalization), where the spins are weakly polarized ($m = \frac{\pi}{1800}$) with a domain wall at the center of the system [Fig. 2.2 (b)]. Since the spreading of the domain wall is monitored throughout the whole time evolution (instead of only at very large times), we can reach a bigger system size within the unitary evolution set up ($N = 128$ and $\chi = 128$).

The spreading of the domain wall can be quantified by the difference of magnetization from the initial state,

$$\Delta s(t) \equiv 1 - \frac{1}{mN}\left(\sum_{i=1}^{N/2}\langle\sigma_i^z(t)\rangle - \sum_{i=N/2+1}^{N}\langle\sigma_i^z(t)\rangle\right), \tag{2.5}$$

where $\Delta s(0) = 0$ and $\Delta s(t) \to 1$ as $t \to \infty$, for typical diffusive systems. We define the scaling exponent α via $\Delta s(t) \sim t^{\alpha}$.

The two scaling exponents γ and α are related to each other by a relation $\gamma = \frac{1}{\alpha} - 1$ [51], which is obtained by dimensional analysis of the spin current. Therefore the values of α corresponding to diffusive and ballistic transport are $\alpha = 1/2$ and $\alpha = 1$, respectively. The system is subdiffusive for $0 < \alpha < 1/2$ and superdiffusive when $1/2 < \alpha < 1$. Fig. 2.3(b) shows the time-evolution of $\Delta s(t)$ for different quasiperiodic potential strengths (λ) with the scaling exponents (α) estimated from a least-squares best fit.

Fig. 2.4 compares the two methods of extracting γ and shows that the results are largely consistent, especially in the subdiffusive regime. Without the quasiperiodic potential ($\lambda = 0$), the interacting AAH model reduces to the isotropic Heisenberg XXZ model and approximately gives the expected result of $\gamma = 0.5$ [34]. Starting from this superdiffusive regime, γ increases with λ

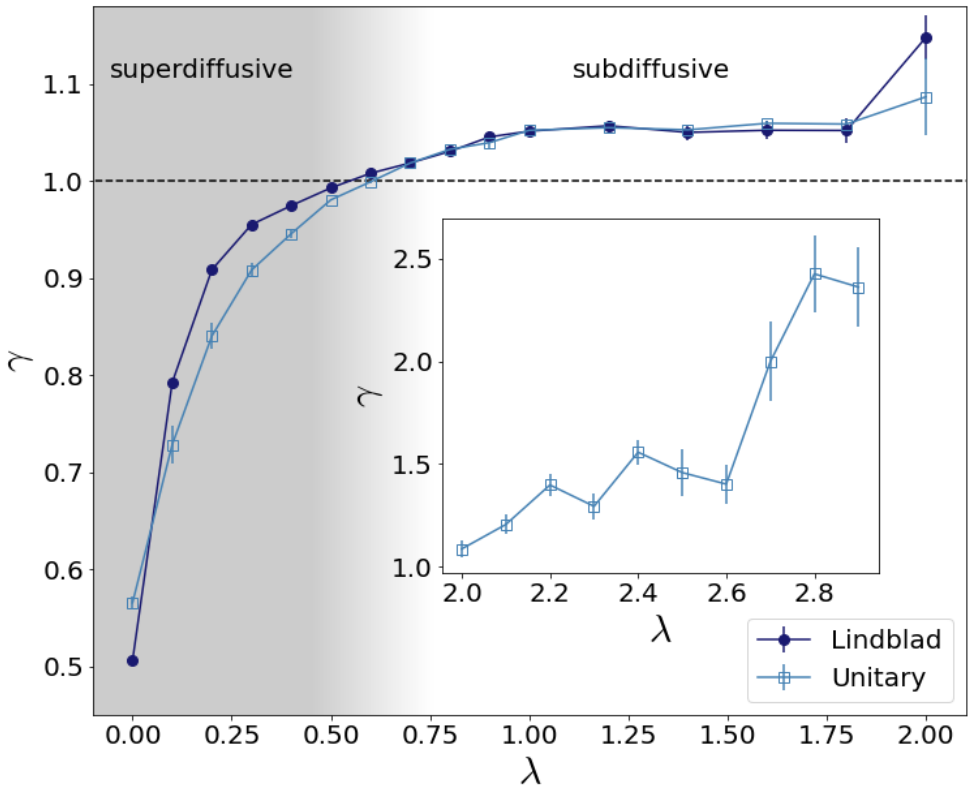

Figure 2.4: The scaling exponent γ from the Lindbladian and the unitary evolution as a function of the quasiperiodic potential strength. The (non-)shaded area represents the (subdiffusive) superdiffusive regime. The inset figure shows the γ for $\lambda \geq 2.0$ from the unitary evolution.The error bar indicates the standard deviation from the fitting samples.

above the critical value for exact diffusion ($\gamma = 1$), demonstrating a dynamical phase transition from superdiffusive to subdiffusive transport. The critical point is around $\lambda_c \approx 0.55\,(0.60)$ according to the Lindbladian (unitary) dynamics. Note the difference from the XXZ model with the uniform random disorder, where the change in γ is discontinuous and has a diffusive *phase* [144]. By contrast, at least for the sizes and times probed in this interacting AAH model, γ changes continuously in the superdiffusive regime and the exact diffusion only occurs at a *point*. We originally expected a diffusive regime for weak potential strength but did not observe it in the system sizes studied.

A previous study on the interacting Aubry-Andre model with fermions revealed a critical point λ_B between the thermal phase and a new intermediate phase [133]. This intermediate "S phase" is characterized by vanishing butterfly velocity and a power-law effective lightcone. Interestingly, our best estimate is that the transport transition ($\lambda_c \approx 0.55$) occurs before the onset of the S phase ($\lambda_B \approx 0.7$) for identical parameters. This suggests that there are two subphases characterized by distinct spin transport physics within the thermal phase: (i) thermal and superdiffusive phase (ii) thermal and subdiffusive phase.

Ref. [133] also showed the transition from S phase to an MBL phase occurs at $1.7 < \lambda_{\text{MBL}} < 1.9$. In our boundary driven system, we calculate up to $\lambda = 2.0$ and observe the dynamics become extremely slow from around $\lambda \approx 1.7$. Although this significant increase in relaxation time is a sign of the possible MBL transition, it also makes it nearly impossible to reach the NESS in this regime. One notable point is that γ exhibits a plateau-like behavior staying near the same value for $1.0 < \lambda < 2.0$.

For $\lambda > 2.0$, γ dramatically increases with increasing λ as shown in the inset of Fig. 2.4. The large error bars at those λ values are due to the very slow dynamics which results in almost no

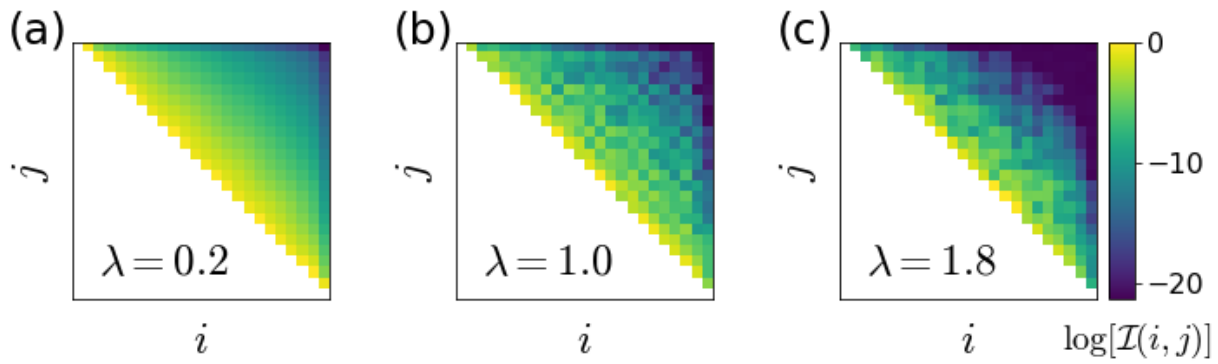

Figure 2.5: The colomap matrix representation of logarithm of the renormalized two-site quantum mutual information of the NESS of the interacting AAH model, $\log \mathcal{I}(i,j)$, for system size $N = 24$ and different quasiperiodic potential strength λ; (a) $\lambda = 0.2$; (b) $\lambda = 1.0$; (c) $\lambda = 1.8$.

changes of the value of $\Delta s(t)$. Accurately locating the localization transition is difficult with such observables, however, similar trends observed [130,134,145] in other 'imbalance' parameters are indicative of a transition.

Incorporating our results with the previous work [133], an updated phase diagram for the strongly interacting AAH model is shown in Fig. 2.1. The phase diagram consists of four dynamical phases: (i) thermal and superdiffusive phase ($\lambda < \lambda_c$); (ii) thermal and subdiffusive phase ($\lambda_c < \lambda < \lambda_B$); (iii) subdiffusive S phase ($\lambda_B < \lambda < \lambda_{\text{MBL}}$); and (iv) MBL phase ($\lambda_{\text{MBL}} < \lambda$).

2.5 Correlation structure

We further examine the correlation and entanglement structure of the NESS of the interacting AAH model. The initial motivation for this calculation was to check that the low entanglement assumption of TEBD is valid for the boundary driven NESS; we subsequently uncovered an interesting pattern in the quantum correlations.

These correlations, which include both classical effects and entanglement, can be quantified using the quantum mutual information (QMI), which has also been studied in the context of

metal-insulator transition in the noninteracting AAH model and the interacting disordered Hubbard chain [146]. The QMI $\mathcal{I}(A, B)$ for two subsystems A and B is given by the following formula [147]:

$$\mathcal{I}(A, B) = S(A) + S(B) - S(A \cup B), \tag{2.6}$$

where $S(A) = -\text{tr}(\rho_A \log \rho_A)$ is the von Neumann entropy of A with reduced density matrix ρ_A. In particular, we consider the two-site QMI $\mathcal{I}(i, j)$, where the two subsystems are the i-th and j-th ($i \neq j$) sites of the system. We calculate QMI from the partial trace of the NESS obtained with the MPO Lindbladian evolution for each parameter.

Fig. 2.5 shows $\mathcal{I}(i, j)$ for the interacting AAH model for several values of λ in a logarithmic colormap scale. For small quasiperiodic potential strengths [Fig. 2.5(a)] the two-site QMI decreases monotonically and smoothly as $x = |i - j|$ increases. On the other hand, although the overall decay trend persists, non-monotonicity appears in $\mathcal{I}(i, j)$ for larger values of λ, noticeable by the checkerboard pattern [Fig. 2.5(b)]. As we further increase λ [Fig. 2.5(c)], one observes the non-monotonicity effect decrease again.

We quantify this "non-monotonicity" pattern by introducing the averaged QMI $\bar{\mathcal{I}}(x) \equiv (1/N_x) \sum_{|i-j|=x} \mathcal{I}(i, j)$, where N_x is the number of i, j combinations satisfying $|i - j| = x$. Fig. 2.6 plots $\bar{\mathcal{I}}(x)$ in log-scale and the two-site correlation length can be read from the inverse slope. We clearly see the three distinct regimes of λ as in Fig. 2.5: (i) smooth and monotonic decrease for $\lambda < 0.5$, (ii) large oscillations for $0.5 < \lambda < 1.4$, and (iii) suppressed oscillations for $1.4 < \lambda$. (Note that the values of λ here are approximate and do not represent sharp critical values.) The first transition from (i) to (ii) seems to be a crossover as the oscillation builds up

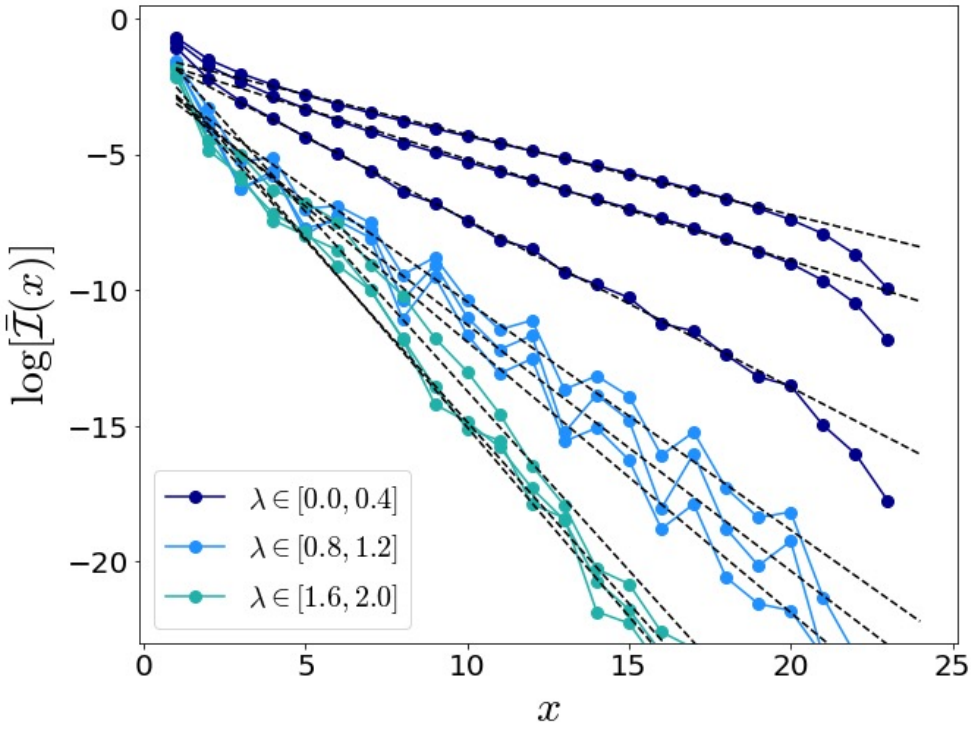

Figure 2.6: The plot of the logarithm of the spatial and Trotter-time averaged two-site quantum mutual information of the NESS of the interacting AAH model, $\log \bar{\mathcal{I}}(x)$, as a function of the distance between two sampling sites x. The three distinct groups are highlighted separately.The dashed gray lines are the best exponential fittings for each λ.

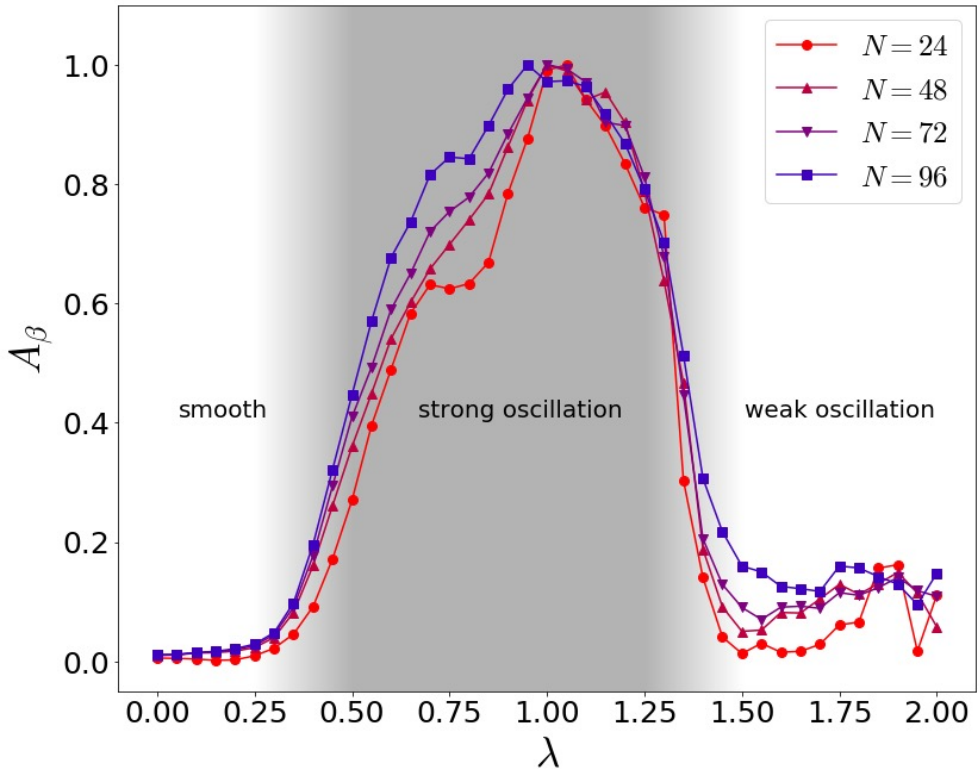

Figure 2.7: The normalized amplitude of the modulation $A_\beta(\lambda, N)$ at $\omega = \beta$ as a function of the quasiperiodic potential strength for several system sizes.

continuously, while the vanishing of the oscillation in (ii) to (iii) is more abrupt pointing towards a phase transition. The correlation length decreases rapidly in regime (i) while the decrease slows down in (ii) and almost saturates in (iii).

The modulation in regime (ii) has the same wavenumber from the quasiperiodic potential ($\beta = (\sqrt{5}-1)/2$). We extract the Fourier amplitude of this wavenumber ($A_\beta = \int \bar{\mathcal{I}}(x) \cos(2\pi\beta x) dx$) and plot it as a function of λ in Fig. 2.7. We confirm that A_β smoothly increases near the first crossover point and steeply falls at the second crossover point. The data is consistent with the three distinct regimes of λ based on the qualitative behavior of two-point QMI. The crossover points do not appear to coincide with the transport critical value λ_c, the critical point in Ref. [133] λ_B, or λ_{MBL}.

This may be a convergence issue – small N suffers from finite size effects and large N is less converged to the NESS. As in all tensor network calculations, there is also the possibility that the entanglement may be more severely affected by truncation compared to local observables. Note that the magnetization profile of the spin chain also has a modulation pattern with wavenumber β, however, it does not show any significant transition as we tune λ.

In addition, our expectation is that correlations in the NESS as measured by the QMI will exhibit an overall exponential decay with distance. However, the precise functional form of the QMI is non-trivial, as shown in Fig. 2.6. A linear fit to $\log \bar{\mathcal{I}}$ gives one measure of the correlation length; the results of this fit are shown in Fig. 2.8. One sees a clear dependence on system size up until approximately $\lambda = 0.75$ and weak dependence only on λ thereafter. However, we know from Fig. 2.7 that the oscillations in the QMI continue to evolve with λ up until approximately $\lambda = 1.4$. Thus, it is only after the oscillations cease that the QMI profile becomes approximately independent of both system size and λ. It is interesting to note that $\lambda = 0.75$ is close to the transition into the slow phase identified in [133].

2.6 Discussion

In this work, using a combination of unitary and open system tensor network methods, we found a transition in spin transport from superdiffusive to subdiffusive as a function of increasing quasiperiodic potential strength. Our results, when combined with those of Ref. [133] which argued for a transition in the speed of operator growth, lead to a rich proposed phase diagram for the strongly interacting AAH model. In addition, we showed that the decay of the QMI also exhibits several distinct regimes as a function of the quasiperiodic potential strength, although

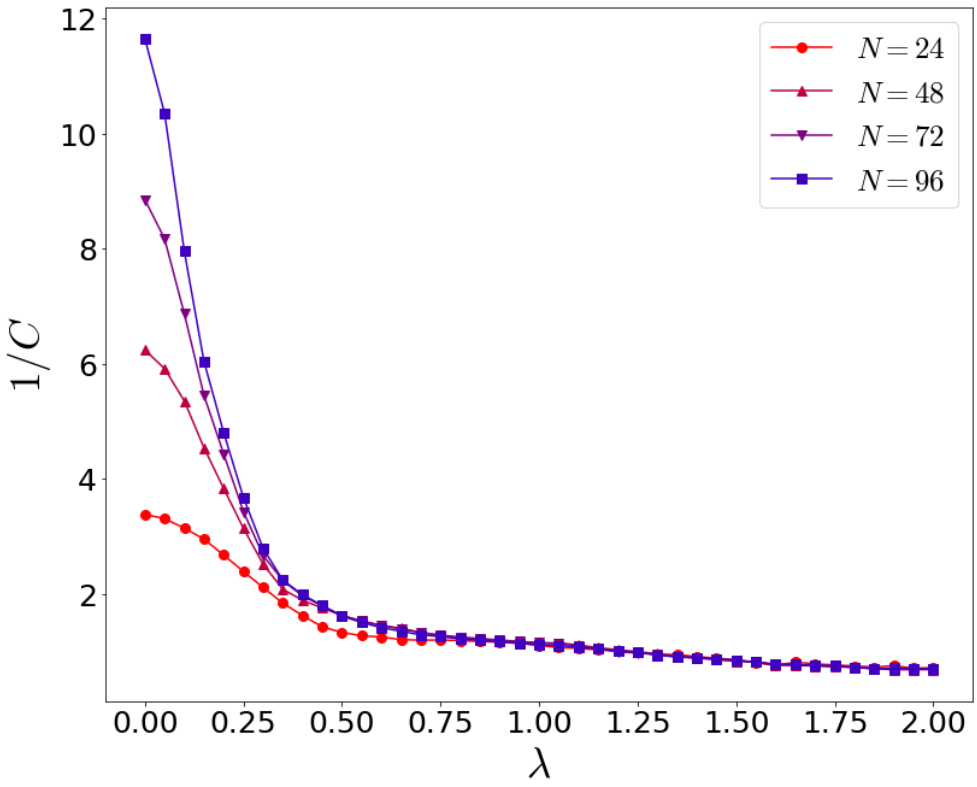

Figure 2.8: The inverse of the slope C of the linear fitting of $\log\left[\bar{\mathcal{I}}(x)\right]$ as a function of the quasiperiodic potential strength for several system sizes.

these regimes may be separated by crossovers rather than genuine phase transitions.

This rich set of phenomenology deserves further study, especially since a simple physical picture is currently lacking. There are various proposals to explain the slow dynamics at intermediate potential strength, but it is not clear if any of these are sufficient. One idea is that, at a mean-field or Hartree-Fock-like level, the strong interaction significantly renormalizes the single-particle potential leading to a regime in which the single-particle spectrum contains a mixture of localized and delocalized states [133]. However, certainly scattering and other interaction effects need to be included.

To better understand the physics in the intermediate regime, it would be interesting to study energy transport in addition to spin transport. One idea is to make more precise the mean-field picture described above, perhaps connecting to prior discussions of mobility edges [137, 148–151]. A solvable model, perhaps using large N technology [152], might also be helpful in developing an analytic understanding of the physics. Our result that the system goes subdiffusive before the speed of operator growth vanishes seems consistent with recently proposed bounds on diffusivity in terms of the operator growth speed, but this connection is not sharp until we understand how to estimate the other timescales involved in the bound [153, 154]. Finally, one could explore the physics discussed here in new regimes, for example, as a function of temperature.

2.7 Acknowledgments

We thank C. White and S. Xu for helpful discussions. B.S. is supported by DOE, ASCR, and QOALAS team. Y.Y. and J.L. are supported by NSF-PFC at the JQI. Y.Y. is also supported by Kwanjeong Educational Foundation.

Chapter 3: Open-system Spin Transport and Operator Weight Dissipation in Spin Chains

This chapter is based on the publication 'Open-system spin transport and operator weight dissipation in spin chains' by Yongchan Yoo, Christopher David White, and Brian Swingle, published as Phys. Rev. B 107, 115118 (2023).

3.1 Overview

We use non-equilibrium steady states to study the effect of dissipation-assisted operator evolution (DAOE) on the scaling behavior of transport in one-dimensional spin chains. We consider three models in the XXZ family: the XXZ model with staggered anisotropy, which is chaotic; XXZ model with no external field and tunable interaction, which is Bethe ansatz integrable and (in the zero interaction limit) free fermion integrable; and the disordered XY model, which is free-fermion integrable and Anderson localized. We find evidence that DAOE's effect on transport is controlled by its effect on the system's conserved quantities. To the extent that DAOE preserves those symmetries, it preserves the scaling of the system's transport properties; to the extent it breaks those conserved quantities, it pushes the system towards diffusive scaling of transport.

3.2 Introduction

Quantum out-of-equilibrium dynamics is at the heart of various areas of physics from condensed matter to high energy physics and even quantum information science. The dynamics of conserved quantities is particularly interesting within this broad non-equilibrium setting. In the solid-state context, measurements of transport of conserved quantities like energy and charge provide a useful window into the underlying dynamics of these complex systems. In particular the *scaling behavior* of a system's transport properties—whether it is diffusive, subdiffusive, or superdiffusive, as well as details like the nature of the scaling function—is intimately connected with the strength of the system's interactions [155], the presence of kinetic constraints and higher-form symmetries [156–166], and its integrable or chaotic nature. Recent experimental developments in various platforms including cold atom systems [15, 16, 167–170], quantum magnets [171], superconducting quantum circuits [172], and heavy-ion collisions [173] are also shedding light on the subject. Along with those experimental results, new theoretical approaches have been developed to tackle the major challenge of calculating and interpreting the observed transport phenomena. Due to the breadth of the subject, theoretical developments include a range of approaches from general frameworks to techniques for specific situations (reviews include [6–9, 11, 174–177]).

These new approaches are especially important for strongly interacting systems where the physical interpretation of transport phenomena is not well understood. Numerical approaches are indispensable since there is often no simple analytical technique available. Tensor network algorithms, especially matrix product state methods, can access transport physics close to the thermodynamic limit [178–180]. For other commonly considered problems (e.g. ground states

of gapped local Hamiltonians and short-time evolution), matrix product state methods are reliable because the states in question have low entanglement. For short-time evolution in particular, TEBD [76, 142] constitutes a controlled approximation. But matrix product state methods become expensive for systems with slow dynamics (e.g., subdiffusive transport [144, 181]) or high amounts of entanglement. Some alternate techniques have been suggested [94, 182–192]. Many of those methods modify the dynamics to a non-unitary time evolution not unlike a Lindblad dynamics. By doing so, they cut off (notionally) less relevant parts of the dynamics while preserving the essential transport physics. From a tensor network perspective, one important outcome of the modification is to reduce the amount of entanglement while preserving the physics of interest. Developing a principled theory of when and why these methods work is an active line of research [193–195].

One of these new tensor network methods, *dissipation assisted operator evolution* (DAOE) [187] employs an artificial dissipation based on *operator weight* to overcome the entanglement barrier in unitary simulations. Here operator weight refers to the number of non-identity single-qubit operators contained in a many-body operator; suppressing high-weight operators—that is, suppressing many-point correlations—suppresses many-body entanglement. Because the conserved quantities and their currents are local operators, the artificial dissipation does not directly modify those quantities or currents. In a chaotic system, the expectation values of conserved quantities and currents determine the state of the system, so one expects the artificial dissipation not to substantially modify the system's state or dynamics. Moreover, because DAOE directly manipulates the operator weight distribution, it is possible to study the influence of operator growth [196–201] on transport physics. Fig. 3.1 gives a schematic of DAOE as implemented with matrix product operators.

We investigate the effect of operator weight dissipation on the scaling behavior of spin transport in one-dimensional lattice models by combining two sources of non-unitarity: DAOE and boundary-driven open system dynamics. The physical quantity of interest is the scaling exponent relating the average spin current to the system size. Diffusive transport gives one characteristic value of the exponent, and the exponent allows us to characterize the transport away from the diffusive case.

First, as a benchmark, we apply the method to the anisotropic XXZ model with a staggered field, which is chaotic and possesses normal diffusive relaxation of the spin current. We find that for any operator dissipation parameters, the normal diffusive transport is maintained. Next, we study the clean XXZ model in three different regimes. In the weak interaction regime, the modified transport shows superdiffusive transport up to the system size we calculated ($N \sim 256$), whereas the unitary limit is believed to exhibit ballistic transport [202–205]. At the isotropic point ($\Delta = 1$) where the non-dissipative transport exhibits a superdiffusive relaxation, the transport under DAOE is still superdiffusive but the scaling exponents vary depending on the operator cut-off length. In the strong interaction regime ($\Delta > 1$), the unitary system's diffusive transport is retained for all operator cut-off lengths up to the largest system size. Lastly, we treat the disordered XY model. There we observe behavior consistent with coherent transport on length scales given by the DAOE cut-off length and diffusive transport on longer length scales; we explain this in terms of DAOE's effect on Anderson orbitals.

Taken together, these results point to the following conclusions. First, as a technical point, DAOE can be usefully combined with open system dynamics. This introduces a need to extrapolate to the physical limit, but the NESS is generally easier to obtain and more stable in the presence of artificial dissipation. Second, DAOE tends to push the dynamics towards diffusive

transport, all other things being equal. It maintains diffusivity for generic chaotic models and typically breaks integrability in non-chaotic models. Third, how well DAOE captures the underlying unitary dynamics depends sensitively on the number and nature of the symmetries it preserves. We elaborate on these points in the discussion.

The rest of the paper is structured as follows. In Section II we introduce the model and the framework for analyzing spin currents. Next, in Section III we describe the methods combining DAOE with open system dynamics. In Section IV we present our main results which include various one-dimensional spin models and crossovers between different transport types. Lastly, we discuss the results and possible future directions in Section V.

3.3 Model and quantities of interest

3.3.1 Model

We study spin transport in three variations of an XXZ spin chain. The general form of the Hamiltonian is

$$H = \sum_{i=1}^{N-1} H_{i,i+1}, \tag{3.1a}$$

$$H_{i,i+1} = \sigma_i^x \sigma_{i+1}^x + \sigma_i^y \sigma_{i+1}^y + \Delta \sigma_i^z \sigma_{i+1}^z + \frac{1}{2}(h_i \sigma_i^z + h_{i+1} \sigma_{i+1}^z), \tag{3.1b}$$

where σ_i^α's are Pauli matrices, Δ controls the anisotropy, and h_i is the magnitude of z-directed field at site i.

The model 4.1 displays a rich variety of spin-transport behaviors. At $\Delta = 0$ it is free-fermion integrable, so it displays ballistic transport if the h_j are uniform and Anderson localiza-

tion if the h_j are random. It can also exhibit a transition between the two behaviors if the h_j are appropriately quasiperiodic [136].

For $\Delta \neq 0$ and $h_j = 0$ uniform, the model is Bethe-ansatz integrable. At half filling it is ballistic for $\Delta \leq 1$ and diffusive for $\Delta > 1$ [51, 65, 96, 98, 206–227]. ([207] Sec. 6 has a useful, concise summary of this literature.) At the isotropic point $\Delta = 1, h = 0$ the model is $SU(2)$ symmetric; this symmetry appears to protect the superdiffusive behavior, which remains even for large $SU(2)$-symmetric perturbations [228].

For $\Delta \neq 0$ and h_i random, the spin transport is not well understood. For small to moderate disorder, the model appears to display anomalous diffusion [144, 229–235]. This anomalous diffusion may be due to Griffiths rare region effects [114, 140, 236–238], but other possible scenarios include irregular scaling of the matrix elements [239], multifractality of eigenstates [235], and a non-Griffiths phenomenological theory of the resistance distribution [181]. The system may undergo a many-body localization (MBL) [110–112] transition at $h \approx 7.6$, but recent work has cast doubt on the location and indeed existence of the transition [240–247]. Detailed reviews are available for the MBL phases [10, 11, 120].

In this paper, we consider three parameter regimes: one chaotic, one Bethe ansatz integrable, and one Anderson localized. DAOE [187] was designed to compute transport coefficients in the first regime, for chaotic one-dimensional quantum systems. To test the method in this case we consider the anisotropic XXZ model with anisotropy $\Delta = 0.5$ and staggered field $h_{2i} = -0.5$ and $h_{2i+1} = 0$. With these parameters, the model is non-integrable and shows diffusive transport [33].

We then pick two cases to study anomalous transport: the zero-field XXZ model and the disordered XX model. The XXZ model at zero field disorder $h = 0$ exhibits various transport

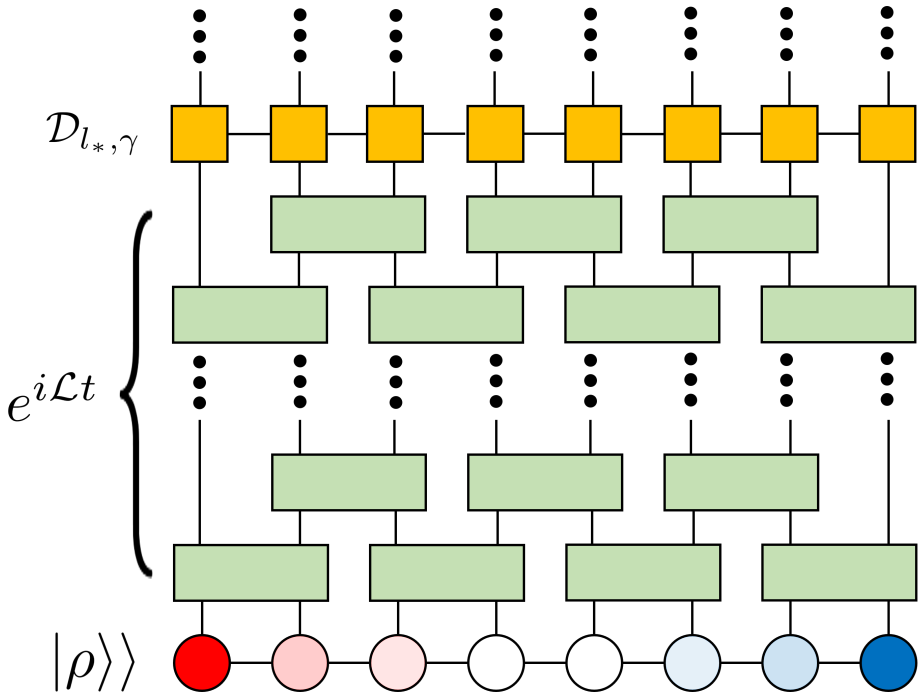

Figure 3.1: Schematics of the combined method of the boundary driven open quantum system and DAOE. It describes one period of the artificial dissipation superoperator application. The gradation of $|\rho\rangle\rangle$ from red to blue is for the spin imbalance by the Markovian spin bath setting.

types as the anisotropy Δ increases from zero. For weak anisotropy $\Delta < 1$, one finds ballistic transport; in the opposite regime $\Delta > 1$, the model exhibits normal diffusive transport. The critical point is at the isotropic point, $\Delta = 1$, where superdiffusive but subballistic transport occurs. The disordered XY model ($\Delta = 0$, $h \neq 0$) also displays an interacting crossover in its transport. The clean limit has ballistic transport thanks to a dual free fermion description, whereas any non-zero disorder brings Anderson localization in the thermodynamic limit [248]. But the model always possesses an extensive number of conserved quantities, and the physical size of these conserved quantities in the spin language varies with the disorder strength.

3.3.2 Spin Current Analysis

Suppose a system has a conserved quantity $Q = \sum_i Q_i$, Q_i local. The corresponding local current J_i is derived from the continuity equation and the Heisenberg equations of motion:

$$\frac{\partial Q_i}{\partial t} = -i\,[Q_i, H] = -(J_i - J_{i+1}). \tag{3.2}$$

The model 4.1 has a conserved quantity $Q^z = \sum_i \sigma_i^z$, the total z-spin; the current is $J_i = \sigma_i^x \sigma_{i+1}^y - \sigma_i^y \sigma_{i+1}^x$.

For systems exhibiting diffusive transport, the discrete Fourier's law $\langle J_i \rangle = -D(\langle Q_{i+1} \rangle - \langle Q_i \rangle)$ relates the current and the corresponding charge density. Here D is the diffusion constant in lattice units. If such a diffusive system is subject to a bias $\langle Q_L \rangle - \langle Q_R \rangle$, where $\langle Q_{L,R} \rangle$ denote fixed values of the spin density at the left and right ends of the sample, the current through the sample scales as

$$\langle J \rangle = -D \frac{\langle Q_L \rangle - \langle Q_R \rangle}{N}, \tag{3.3}$$

where N is the length of the system.

More generally, if the system exhibits anomalous transport, the above relation is modified by introducing a scaling exponent χ,

$$\langle J \rangle = -D_\chi \frac{\langle Q_L \rangle - \langle Q_R \rangle}{N^\chi} \tag{3.4}$$

We assume that χ in Eq. 4.19 is the only scaling exponent that characterizes the transport. Other than the normal diffusive transport ($\chi = 1$), possible types of anomalous transport are (i) ballistic

transport ($\chi = 0$), (ii) superdiffusive transport ($0 < \chi < 1$), and (iii) subdiffusive transport ($\chi > 1$). In a localized state, this power-law ansatz does not provide a good description of the spin transport. We can heuristically understand localized systems as having $\chi \to \infty$.

3.4 Methods

We extract quantum transport properties with dissipation assisted operator evolution (DAOE) simulations of non-equilibrium steady states (NESS). Each method takes advantage of non-unitary evolution to make simulating a system's dynamics tractable. We find that combining them gives new insights into both the systems' physics and the effect of DAOE on that physics. In this section we describe the two methods.

3.4.1 Master Equation and NESS

In a NESS experiment on a spin chain we attach leads with slightly different chemical potentials to the two ends of the system. The leads thermalize the system, so in the long-time limit its state should have an efficient MPO representation [249, 250]. But because the leads' chemical potentials differ, they induce a small spin current; how this current scales with system size characterizes the model's transport properties (cf Sec. 3.3.2).

Formally the NESS is the fixed point solution $d\rho_\infty/dt = 0$ of the Gorini-Kossakowski-Lindblad-Sudarshan (GKLS) master equation [24, 25]

$$\frac{d\rho}{dt} = \mathcal{L}(\rho) \equiv i[\rho, H] + \sum_\nu \left[L_\nu \rho L_\nu^\dagger - \frac{1}{2} \left\{ L_\nu^\dagger L_\nu, \rho \right\} \right]. \tag{3.5}$$

The NESS is generated by full Hamiltonian H and Lindblad operators L_ν, which model the leads.

Explicitly, the Lindblad operators are

$$L_{1,\pm} = \sqrt{1 \pm \mu}\, \sigma_1^{\pm}$$
$$L_{N,\pm} = \sqrt{1 \mp \mu}\, \sigma_N^{\pm} \tag{3.6}$$

where $\sigma^{\pm} = \frac{1}{2}(\sigma^x \pm i\sigma^y)$.

Under the right conditions, the GKLS equation has exactly one steady-state solution [251], but even when this is the case, there may still be many slowly-decaying almost steady states, especially when the jump operators only affect the edges of the sample. We expect to have a unique NESS ρ_∞ which is accessible in the long-time limit $t \to \infty$, but the presence of slow modes means we must be careful about convergence in time.

3.4.2 Artificial Dissipation Superoperator

Dissipation assisted operator evolution (DAOE) [187] is a tensor network-based algorithm that reduces the weight of operators longer than a given cut-off length (In this context, the length of operator means number of nontrivial Pauli operators. This is in contrast to diameter, or distance between leftmost and rightmost nontrivial Pauli operator, which [194] and (implicitly) [193] argue is the relevant quantity in spatially local systems.). These long operators are responsible for the entanglement growth that makes MPS simulations infeasible. By gently reducing them, DAOE makes long-time simulations possible.

DAOE is implemented by an artificial dissipation superoperator acting on the operator Hilbert space. The operator Hilbert space of our N-site system is spanned by a basis of 4^N Pauli strings. Each element (Pauli string) $\mathcal{S}$ in the basis is represented by the tensor product of

single-site Pauli matrices $\sigma^0, \sigma^x, \sigma^y, \sigma^z$. The *length* $\ell_{\mathcal{S}}$ of a string $\mathcal{S}$ is the number of non-trivial Pauli matrices in $\mathcal{S}$. In this notation the artificial dissipation superoperator is

$$\mathcal{D}_{\ell_*,\gamma}[\mathcal{S}] = \begin{cases} \mathcal{S} & \text{if } \ell_{\mathcal{S}} \leq \ell_* \\ e^{-\gamma(\ell_{\mathcal{S}}-\ell_*)}\mathcal{S} & \text{if } \ell_{\mathcal{S}} > \ell_*. \end{cases} \tag{3.7}$$

Periodically applying this superoperator generates a non-unitary quantum evolution that can be heuristically understood as a global 'bath'. Just as a bath—consider in particular the depolarizing channel—reduces the expectation value of a string of ℓ nontrivial Pauli operators by an amount $\propto \ell$, the DAOE superoperator 3.7 reduces the expectation value of a string of ℓ nontrivial Pauli operators by an amount $\propto \max(\ell - \ell_*, 0)$.

DAOE as presented in [187] uses the above artificial operator dissipation to modify the Heisenberg picture dynamics of observables. For example, starting from an initial state ρ_0 with some spatially varying profile for the average spin density $tr(S^z_r \rho_0)$, the spin diffusivity can be extracted from the time-dependent spin profile $tr(S^z_r(t)\rho_0)$ where $S^z_r(t)$ is the Heisenberg evolution of S^z at site r. DAOE is then used to modify the dynamics of $S^z_r(t)$ to render it more tractable to an entanglement-constrained tensor network simulation, with the true physics obtained from an extrapolation in γ.

However, more than just modifying the particular dynamics with the introduction of γ, DAOE significantly alters the basic rules of quantum evolution. This is most easily seen in the Schrodinger picture formulation, where the fact that DAOE reduces expectation values of long operators without reducing expectation values of short operators means it can break positivity of density matrices. Consider applying $D_{\ell_*=1,\gamma}$ to the density matrix of the two-site state $|\uparrow\uparrow\rangle$: it

becomes

$$\frac{1}{4}\mathcal{D}_{\ell_*=1,\gamma}\Big[I+\sigma_1^z+\sigma_2^z+\sigma_z^1\sigma_z^2\Big]=I+\sigma_1^z+\sigma_2^z+e^{-\gamma}\sigma_z^1\sigma_z^2 \tag{3.8}$$

which has one negative eigenvalue $\frac{1}{4}(e^{-\gamma}-1)$.

Crucially, the Heisenberg and Schrodinger pictures remain equivalent even in the presence of DAOE's artificial operator dissipation (Not all schemes have this property. The Liouvillian graph scheme of [194]—like DAOE—gives a linear effective evolution, so Heisenberg and Schrodinger evolutions are—as in DAOE—identical. But DMT [184] is strongly nonlinear, because it uses the SVD of a correlation matrix to determine what correlations to discard. (This nonlinearity is likely responsible for DMT's success in treating nearly free fermion [186] and integrable KPZ [170, 252] transport.) The method of Kvorning, Herviou, and Bardarson [188] is also nonlinear, because it approximates long-range correlation functions by products of local expectation values.). In the Heisenberg picture, the time evolution of some operator A by a Lindbladian $\mathcal{L}$ becomes

$$A(t)=\left[\mathcal{D}_{\ell_*,\gamma}e^{-i\mathcal{L}\tau}\right]^{t/\tau}A(0)\ . \tag{3.9}$$

But the DAOE superoperator, like the Lindblad time evolution superoperator $e^{i\mathcal{L}\tau}$, is linear; indeed $\mathcal{D}_{\ell_*,\gamma}$ is Hermitian under the trace inner product $\langle A,B\rangle=\mathrm{tr}\big(A^\dagger B\big)$. So the operator expectation value $\langle A(t)\rangle$ obeys

$$\mathrm{tr}\,A(t)\rho(0)=\mathrm{tr}\,A\rho(t) \tag{3.10}$$

where A is the Schrödinger picture operator and

$$\rho(t)=\left[\mathcal{D}_{\ell_*,\gamma}\rho(0)e^{i\mathcal{L}\tau}\right]^{t/\tau}\ . \tag{3.11}$$

Hence, the Schrödinger and Heisenberg pictures give identical dynamics, so we can speak of DAOE "failing to preserve positivity". Moreover we can use NESS simulations to examine how DAOE changes a system's dynamics, with full confidence that the results apply to Heisenberg-picture experiments like those of [187].

Given the significant modifications that DAOE makes to the quantum dynamics, it is important to understand when and why DAOE gives a good approximation of the transport coefficients. Ref. [193] analyses the "operator backflow" process, in which information contained in large-diameter, non-local operators flows into the subspace of short operators as the system evolves. For chaotic models, combinatoric scattering amplitude arguments and numerical experiments confirm the exponential suppression of the backflow process contribution to correlation functions between local operators. Consequently, the estimated error of DAOE-produced transport coefficients is also exponentially small in such systems.

But this backflow analysis will not go through for integrable systems. In the language of [194], the backflow analysis assumes that the dynamics of long operators is chaotic. But in the integrable system the tower of local conserved quantities will strongly constrain that dynamics—it cannot be treated as chaotic. Additionally, the interplay of DAOE with more complex non-Abelian symmetries and with integrability has not yet been studied. Some of our results below address these open problems.

3.4.3 Tensor Network Implementation

Both NESS and DAOE can be efficiently realized in the language of tensor networks. In this formalism, a vector in the operator Hilbert space directly expresses the corresponding den-

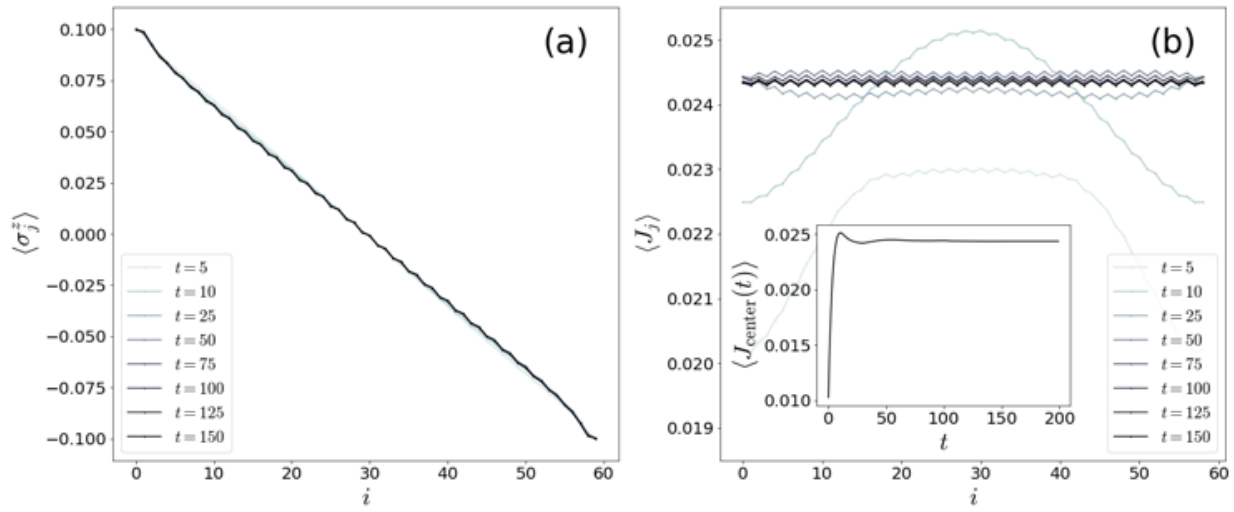

Figure 3.2: (a) Spin profile and (b) spin current profile extracted from the modified NESS of the chaotic anisotropic XXZ model with $(L, \ell_*, \gamma) = (60, 3, 0.4)$ at different times. The inset in (b) shows the time evolution of the spin current at the center of the chain.

sity matrix; we call such a vector a *superket state* $|\rho\rangle\rangle$. Physical operators can act on ρ in two ways, "bra-side" and "ket-side"—formally these are the left and right regular representations of $GL\left[(\mathbb{C}^2)^{\otimes n}\right]$. Two different physical operators X, Y can act on ρ by $|X\rho Y\rangle\rangle = Y^T \otimes X|\rho\rangle\rangle$—formally, this is a representation of $\left(GL\left[(\mathbb{C}^2)^{\otimes n}\right]\right)^{\otimes 2}$. In this representation the Lindbladian operator in Eq. 3.5 is

$$\mathcal{L} = -i\left(I \otimes H - H^T \otimes I\right) + \sum_\nu \left(L_\nu^* \otimes L_\nu - \frac{1}{2}\left(I \otimes L_\nu^\dagger L_\nu + L_\nu^T L_\nu^* \otimes I\right)\right). \tag{3.12}$$

Since the operator Hilbert space has a tensor product structure we can implement superket-superoperator calculations with standard MPS equipment. The time evolution of the superket is performed by the standard time-evolving block decimation (TEBD) algorithm [76, 142] with second-order Suzuki-Trotter decomposition of the time evolution operator $e^{\mathcal{L}t}$ [84, 85, 180]. We use the Trotter time step $\delta t = 0.1$ for our numerical simulations and check convergence in the Trotter step in App. B.2.

We interleave the TEBD Lindbladian evolution with periodic application of the DAOE superoperator (cf Fig. 3.1). We take the DAOE period $\tau = 1$. For small γ, the ratio γ/τ controls the effective dissipative dynamics; in principle, one would like to take τ small. The DAOE superoperator $\mathcal{D}_{\ell_*,\gamma}$ has an exact MPO representation of bond dimension ℓ_*, so applying it to a matrix product density operator is not infeasible. But $\mathcal{D}_{\ell_*,\gamma}$ does not conveniently commute with the terms in the Lindbladian 3.12, so we cannot fold it into Suzuki-Trotter decomposition leading to TEBD, and we treat it separately. At time $t \in [N\tau, (N+1)\tau]$, the initial superket $|\rho\rangle\rangle$ is evolved into

$$|\rho(t)\rangle\rangle = e^{\mathcal{L}(t-N\tau)} \left(\mathcal{D}_{\ell_*,\gamma} e^{\mathcal{L}\tau}\right)^N |\rho(0)\rangle\rangle. \tag{3.13}$$

We call the resulting state the modified NESS to stress the dissipation of long operator contributions.

For some models—especially those with subdiffusive or localized transport—the state can take a very long time to converge to the (modified) NESS. To alleviate this problem, we choose the initial superket as a linearly interpolated state between the two baths at the end of the system. Explicitly, the initial superket is chosen as $|\rho(0)\rangle\rangle \propto \exp(-\sum_i \mu_i \sigma_i^z)$. Since this spin profile is similar to the steady-state solution of Fourier's law we expect fast convergence to the modified NESS.

After obtaining the modified NESS, we directly calculate the expectation value of a local operator $\mathcal{O}$ by taking the operator trace $|\mathcal{O}\rangle = \mathrm{tr}(\mathcal{O}|\rho_\infty\rangle\rangle)/\,\mathrm{tr}(|\rho_\infty\rangle\rangle)$. There are small fluctuations in site i and time t of the current $J_i(t)$ even if we closely approach the modified NESS due to the limitation of our numerical methods. To avoid this issue, we average over all sites and a small time window to estimate the average current J which is supposed to be independent of i

and t.

3.4.4 Convergence

We check the convergence of the normalized, spatially-averaged current expectation value in the following three categories.

- Time: We declare that the NESS has been approximately reached when the relative change in the current is less than 10^{-4} per unit of time (J^{-1}).
- Bond dimension: the current varies $< 2\%$ between the bond dimension shown and a bond dimension smaller by a factor of $1/2$ or $3/4$ (depending on model and parameters).
- Trotter step size: for the clean models the current varies $< 1\%$ between the Trotter step shown and a smaller Trotter step size $\delta t = 0.025$ ($1/4$ the value used in plots shown). We allow larger tolerances for the disordered XY model: there the worst case is 8% at the strongest disorder ($h > 3.0$).

The total error budget is thus less than 5% for the clean models and 10% for the worst case of the disordered model. In general, convergence is affected by the DAOE parameters: it becomes worse as the dissipation strength γ decreases and the cut-off length ℓ_* increases. For a fixed set of TEBD and DAOE parameters, we also find that it becomes harder to obtain a reliable NESS for larger anisotropy Δ (disorder h) in the clean XXZ (disordered XY) model. Details are presented in App. B.2.

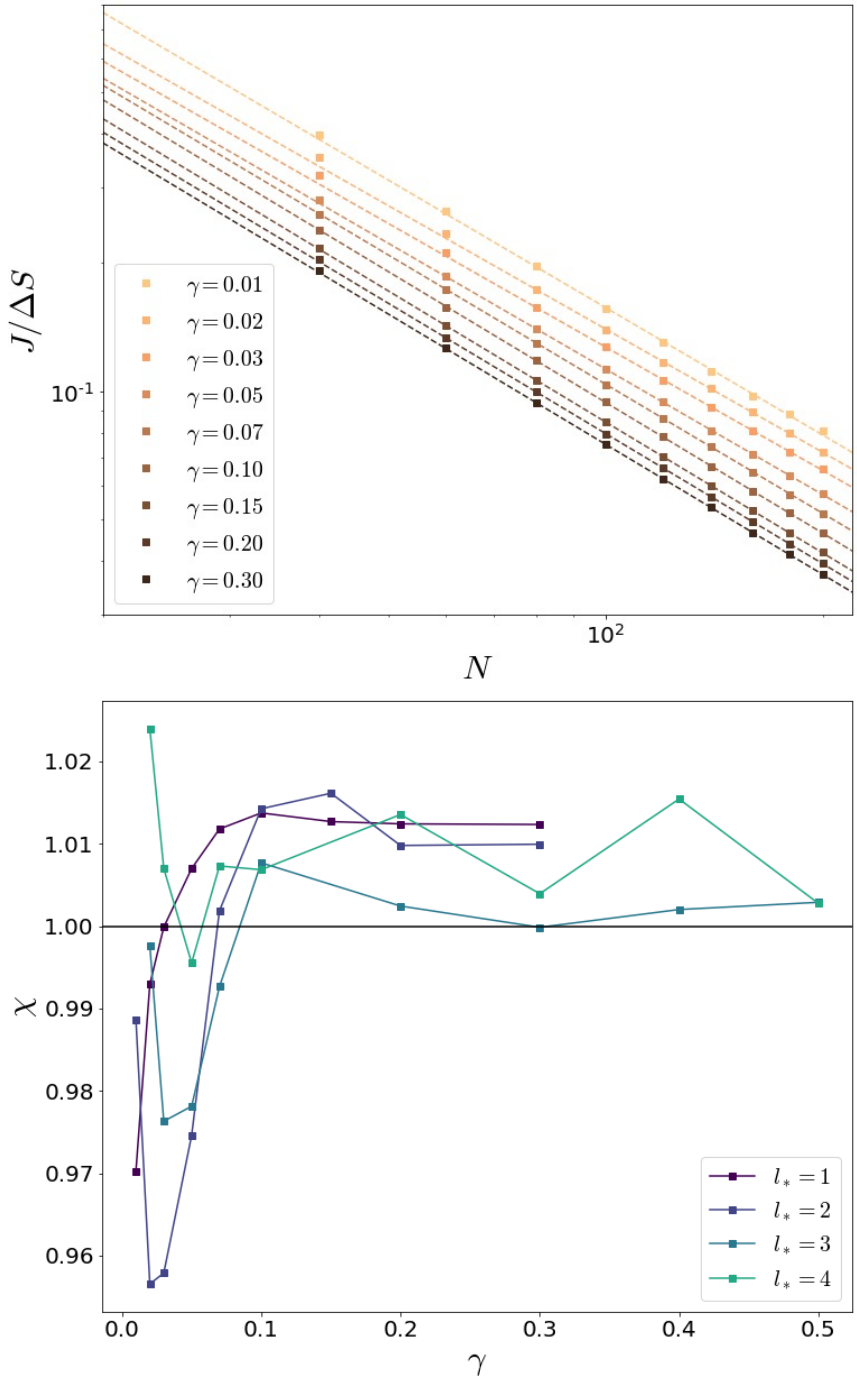

Figure 3.3: **Top**: Scaled average spin current with DAOE cut-off length $\ell_* = 2$ for the chaotic anisotropic XXZ model with a staggered field as a function of system size N. The dashed lines are the best power law that fits the data with system size $N \geq 100$. Although the data is not shown, similar results hold for all other cut-off lengths. **Bottom**: Scaling exponent extracted from the fit. The black horizontal solid line represents χ corresponding to the (normal) diffusion. The model parameters are in the main text.

3.5 Results

3.5.1 Chaotic Anisotropic XXZ Model

First, we study spin transport in the anisotropic XXZ model with a staggered field. We take the anisotropy $\Delta = 0.5$ and the staggered field $h_{2i} = -0.5, h_{2i+1} = 0$; the staggered field breaks integrability. We impose a chemical potential difference

$$\mu = 0.1$$

and work at bond dimension 32. We check that the system has in fact converged to the NESS by comparing the variance of the spin current across sites to its average.

Fig. 3.2 shows the spin $\langle \sigma_j^z \rangle$ and current $\langle J_j \rangle$ as a function of position in the NESS of this model. It displays roughly the expected linear profile. The zigzag pattern in $\langle \sigma_j^z \rangle$ comes about because of the staggered field. Additionally, the interplay of the Hamiltonian bond term with the Lindblad operators causes $\langle \sigma_j^z \rangle$ to depart from the linear profile near the boundaries. We, therefore, drop 5 sites at the left and right end of the chain, so

$$\Delta S = \langle \sigma_6^z \rangle - \langle \sigma_{N-5}^z \rangle. \tag{3.14}$$

Likewise in fits to 4.19 we take the length to be $N - 10$.

Fig. 3.3 top shows $J/\Delta S$ as a function of system size across dissipation strengths γ, all for cutoff $\ell_* = 2$, together with power-law fits. The fits are solely to system sizes $N \geq 100$. Fig. 3.3 bottom shows the power resulting from the fit, across artificial dissipation strengths γ and cutoffs

ℓ_*. The powers are all close to one. They deviate more for smaller γ because DAOE reduces large correlation functions less quickly at smaller γ so the simulations are more computationally demanding. The simulations do converge within 3% for NESS expectation values at bond dimension 32, but those criteria leave room for the small deviations from the diffusive exponent $\chi = 1$ that we see in Fig. 3.3 bottom.

To see why small-γ simulations are more difficult—and why large-γ simulations modify transport—we can make a rough model for the dynamics of the operator length distribution. The Hamiltonian increases the length of a Pauli string at a rate ≈ 1 (in our units). DAOE, on the other hand, decreases weight on a Pauli string of length ℓ at a rate $\approx \gamma(\ell - \ell_*)$. These effects balance at a characteristic DAOE lengthscale $\ell_{\text{DAOE}} \sim \ell_* + 1/\gamma$.

But even in the unitary NESS, the boundary Lindblad operators (and the resulting spread of entanglement) limit operator growth; this is one way to see why unitary NESS simulations are feasible. Write ξ for the characteristic operator length of the unitary NESS. ξ is not quite the correlation length: long operators contribute substantially to ξ even if they have a small weight, because there are many of them.

When $\gamma \ll (\xi - \ell_*)^{-1}$, DAOE does not substantially change the operator weight dynamics, because the spread of bath entanglement keeps most operators shorter than the characteristic DAOE length ℓ_{DAOE}. The simulations are then approximately as hard as unitary NESS simulations. When $\gamma \gg (\xi - \ell_*)^{-1}$, by contrast, DAOE substantially reduces the characteristic operator length and the simulations become easier than unitary NESS simulations.

In Fig. 3.4 we show the estimated diffusion coefficient $D_{\ell_*}(\gamma)$ as a function of γ across cutoff lengths ℓ_*, together with the unitary value of [33]. To extract these diffusion coefficients we fit ΔS and N to Eq. 4.19 with fixed scaling exponent $\chi = 1$. $D_{\ell_*}(\gamma)$ appears linear in γ

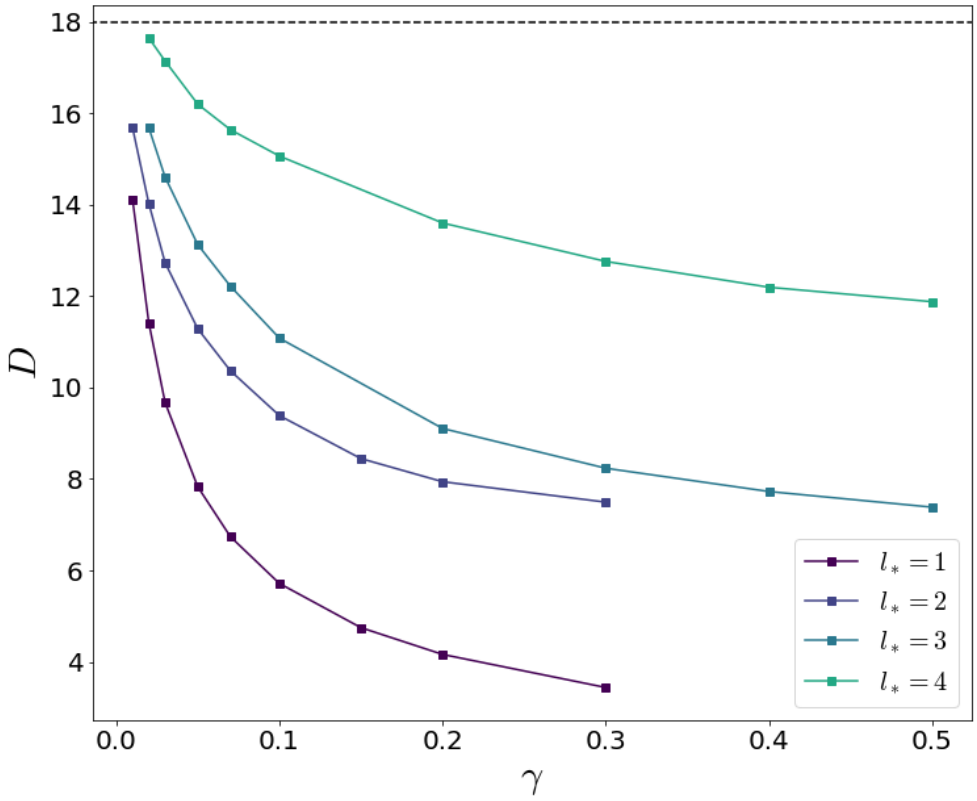

Figure 3.4: Diffusion constants of the chaotic anisotropic XXZ model for various DAOE parameters, from fits with fixed $\chi = 1$. The black horizontal dashed line represents D at the unitary limit ($\gamma \to 0$) from Ref. [33].

for $\gamma \sim 0.05$. Linear extrapolation to $\gamma = 0$ puts the unitary diffusion coefficient $D(\gamma = 0)$ somewhat above the value of [33]; we again attribute this to the imprecision of our small-γ simulations.

3.5.2 Integrable XXZ Model

Next, we investigate spin transport of the integrable XXZ model with anisotropy $0.0 \leq \Delta \leq 2.0$. We fix the magnitude of the artificial dissipation at $\gamma/\tau = 10.0$ for all cut-off lengths $\ell_* \in \{1, 2, \ldots, 5\}$. This artificial dissipation reduces the expectation value of operators longer than ℓ_* almost to zero, so it only allows processes involving operators with length $\ell > \ell_*$ on timescales shorter than $\tau = 1$.

For each ℓ_* and Δ, we plot the the scaled average spin current $J/\Delta S$ as a function of the system size in Fig's 3.5 (anisotropic case $\Delta \neq 1$) and 3.8 (isotropic case $\Delta = 1$). We then display the scaling exponents χ as a function of anisotropy Δ across cutoff lengths ℓ_* in Fig. 3.6.

3.5.2.1 Generic anisotropic case $(\Delta \neq 0, 1.0)$

Fig. 3.5 shows how the scaled average spin current depends on system size N and cutoff length ℓ_* for weak anisotropy $\Delta = 0.5$ (top) and strong anisotropy $\Delta = 1.5$ (bottom).

For weak anisotropy, the unitary system displays ballistic transport. When strongly perturbed with DAOE it displays two kinds of behavior: for $\ell_* \leq 3$ the system is nearly diffusive at all length scales, while for $\ell_* \geq 4$ it displays transient superdiffusive transport, with apparent exponent $\chi < 1$ at short length scales, before approaching diffusion at long length scales. We speculate that for $\ell_* \geq 4$ even strong artificial dissipation causes only weak scattering between

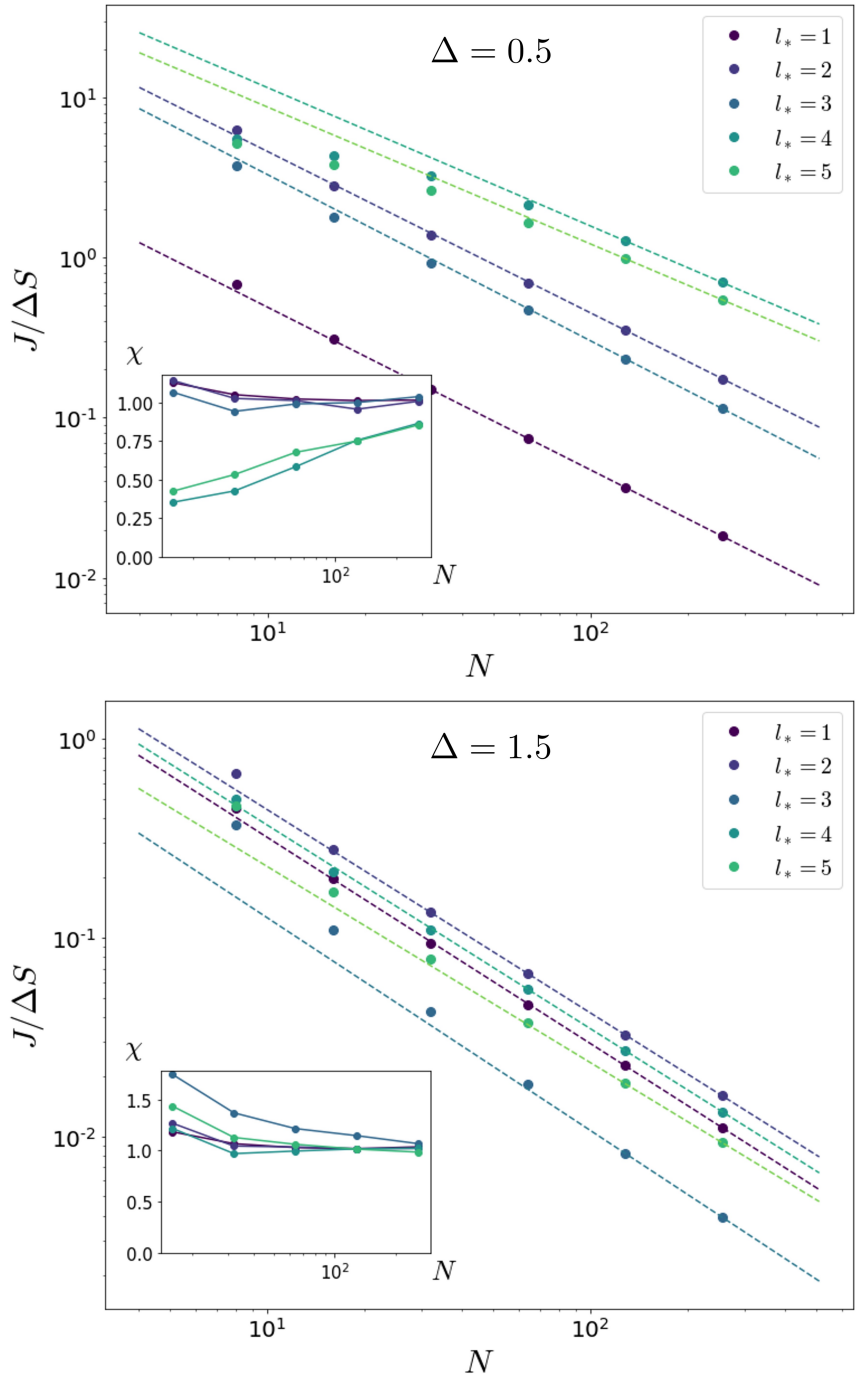

Figure 3.5: Scaled average spin current of the clean Heisenberg XXZ model as a function of system size N at $\Delta = 0.5$ (**top**) and $\Delta = 1.5$ (**bottom**). The dashed lines are best power law fittings corresponding to the (modified) NESS expectation values using data for $N \geq 100$.

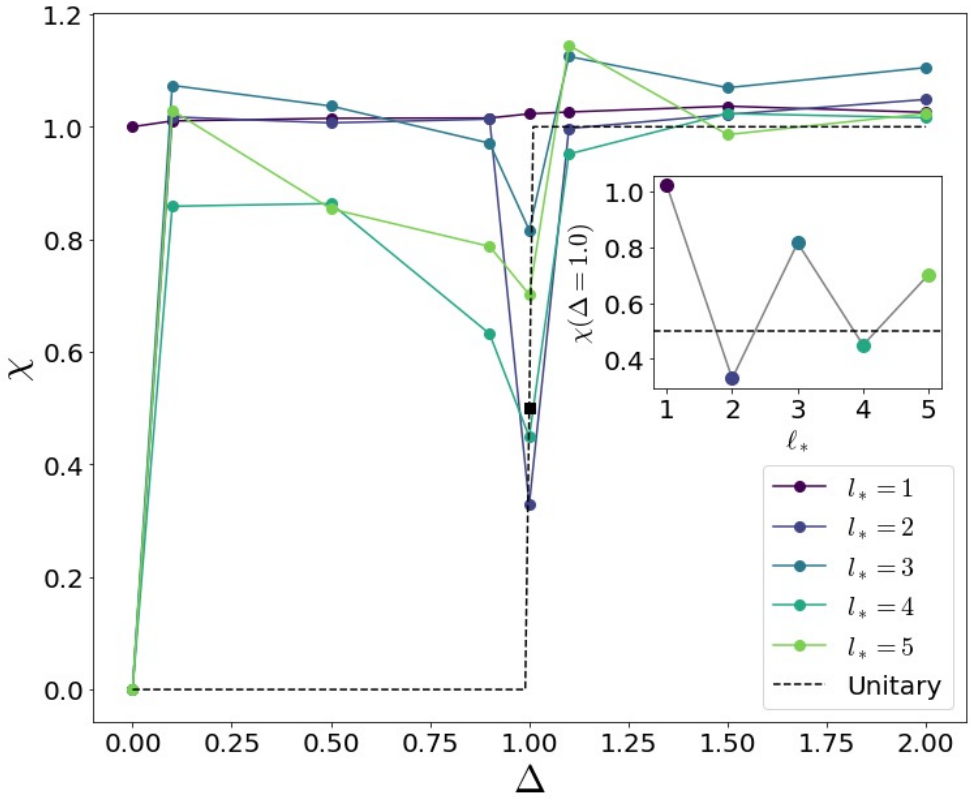

Figure 3.6: Scaling exponents χ of the modified NESS from the anisotropic XXZ model without the disorder. The black dashed line represents the value without DAOE [34, 51].

quasiparticles.

For strong anisotropy the unitary model is diffusive. When strongly perturbed with DAOE it retains that diffusive behavior in the long-system limit. At short length scales, though, it displays apparent subdiffusive behavior with apparent exponent $\chi > 1$. This transient behavior is not monotonic in cut-off length.

Fig. 3.6 shows the scaling exponent χ as a function of the anisotropy Δ. For $\ell_* = 1$ the modified NESS is diffusive (scaling exponent $\chi = 1$) at every anisotropy Δ. But for $\ell_* > 1$ the modified NESS's behavior is much richer. It is ballistic at the free fermion point $\Delta = 0$, just like the unitary NESS, but even small interactions cause DAOE to push the system to diffusion. (Recall that in Fig. 3.5 we saw the scaling exponent χ approaching the diffusive $\chi = 1$ as system size N increased.) At the isotropic point, $\Delta = 1$ DAOE preserves some of the superdiffusive behavior of the unitary model. We discuss both $\Delta = 0$ and $\Delta = 1$ further in the next sections.

In this section we have worked at large $\gamma = 10$. We briefly discuss small γ in App. B.4.

3.5.2.2 Free fermion case ($\Delta = 0$)

As can be seen from left-most point in Fig. 3.6, the $\Delta = 0$ case retains ballistic transport provided $\ell_* > 1$. This has a simple explanation in terms of the allowed NESS in the model. Most of the free fermion conserved quantities are quite complex in the spin language (see App. B.1). But there is a special exception: the local current J_i, when summed over all lattice sites, is conserved. Moreover, because this operator is a sum of 2-site operators, it is also exactly preserved by DAOE. So a linearized steady state of the form $I + \sum_i a_i J_i$ is an exact NESS since it is preserved by DAOE and commutes with H. Provided $\ell_* > 1$, we thus have a family of NESS that

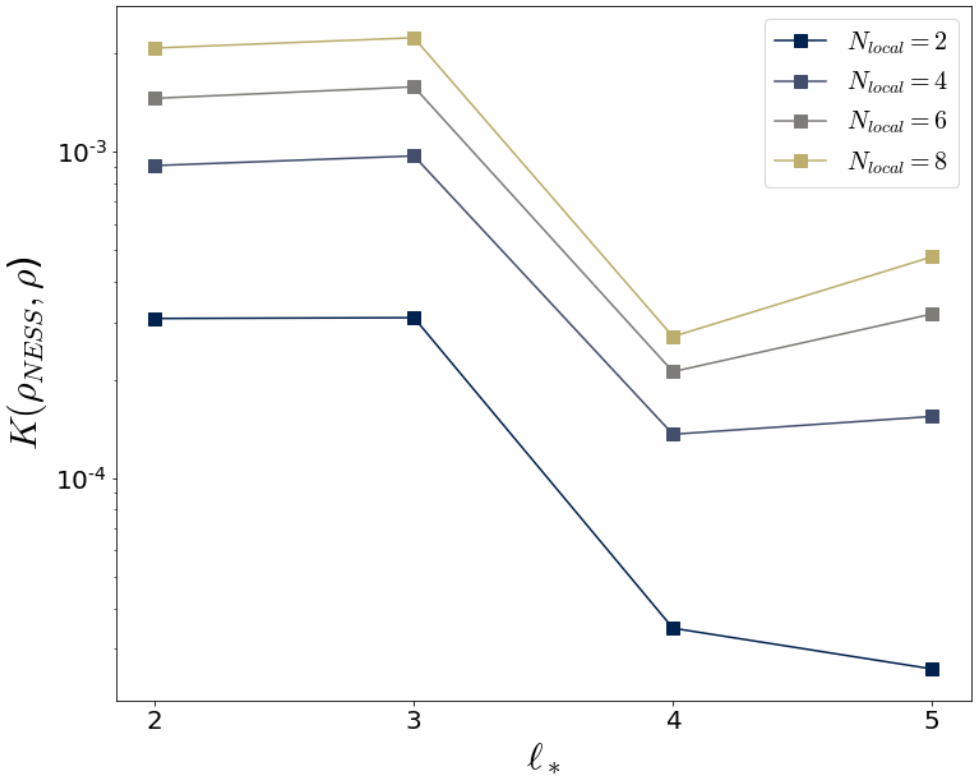

Figure 3.7: Trace distance $K(\rho_{NESS}, \rho)$ between trial density matrices and the local NESSs obtained as reduced density matrices of the full NESS of the free fermion case for various local system sizes N_{local}. The local NESSs are extracted from the full NESS of $N = 48$ and $\chi = 32$.

reproduce the ballistic transport of the unitary limit. This presumably explains the ballistic value seen in Fig. 3.6.

To test this presumption, we study the structure of the NESS in more detail. In reality, we expect the true unitary NESS to have a form like

$$\rho_{\text{NESS}} \propto e^{-\sum_i a_i J_i} + \cdots \tag{3.15}$$

with the a_i uniform. This is the maximum-entropy state at zero energy and an appropriate current where $\cdots$ denote corrections from other operators that are negligible for our purposes. The a_i are typically small, so the linearized form in the previous paragraph is a good local approximation, but there are non-negligible corrections to the linearized form when the system size is larger. Fig. 3.7 shows a comparison of the trace distance between the postulated NESS of Eq. 3.15 and the NESS obtained from DAOE. Here, the trace distance between two density matrices ρ_A and ρ_B is defined as

$$K(\rho_A, \rho_B) = \frac{1}{2} \operatorname{tr}\left(\sqrt{(\rho_A - \rho_B)^2}\right). \tag{3.16}$$

We see that the agreement is quite good already for $\ell_* = 2, 3$ and further improves for $\ell_* = 4, 5$. This particular pattern of improvement arises because the expansion of ρ_{NESS} only has operators of even weight, so when $\ell_* > 1$ we preserve all the weight two operators but not weight four operators, and when $\ell_* > 3$ we preserved all the weight two and four operators.

To summarize, when $\Delta = 0$ we showed that DAOE preserves a family of NESS exhibiting ballistic transport whenever $\ell_* > 1$. We further showed in Fig. 3.7 that these are the steady states realized in the actual converged simulation. Hence, we see again that the fact that DAOE

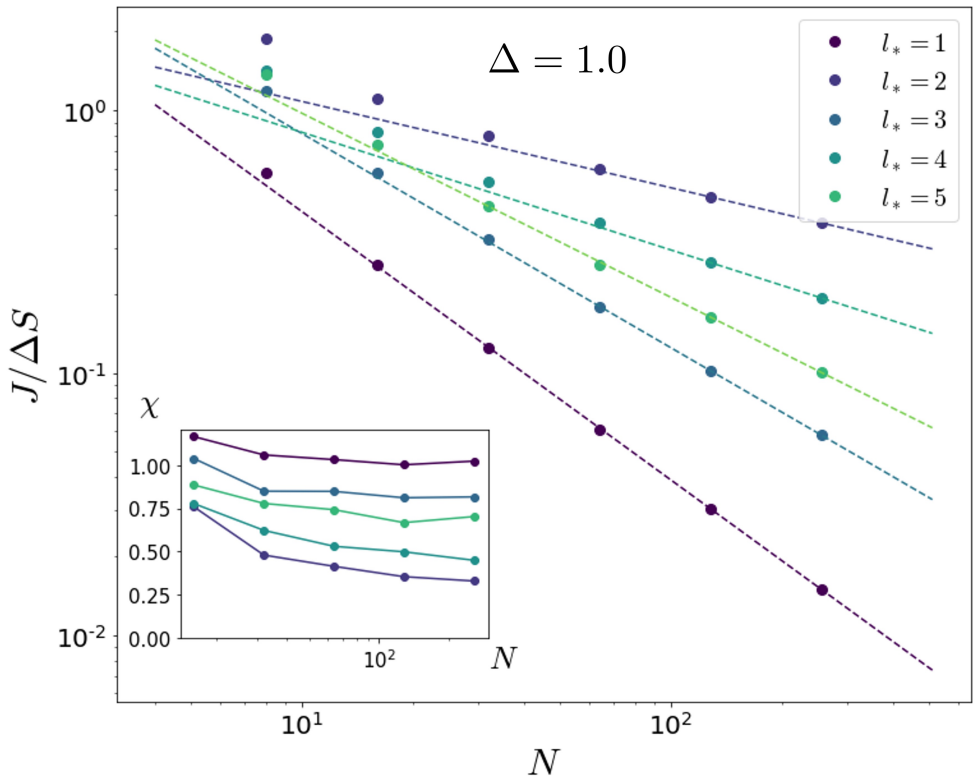

Figure 3.8: Scaled average spin current of the clean Heisenberg XXZ model as a function of system size N at $\Delta = 1.0$. The dashed lines are best power law fittings to corresponding the (modified) NESS expectation values.

preserves the summed current operator as a symmetry is crucial to recovering the unitary physics.

3.5.2.3 Isotropic case $(\Delta = 1.0)$

At the isotropic ($\Delta = 1.0$) point the model has an onsite $SU(2)$ symmetry. The unitary model is superdiffusive with exponent $\chi = 0.5$ [51, 205, 253]. SU(2)-symmetric Hamiltonian perturbations do not appear to break superdiffusion down to diffusion [228], although this unexpected stability is believed to be a finite-size effect. The appropriate effective field theory is diffusive, and classical $SU(2)$-symmetric models generically display diffusion [254]—though some classical models show finite-length transport faster than the asymptotic diffusion. $SU(2)$-symmetric dissipation, however, gives a system with at most logarithmic corrections to diffu-

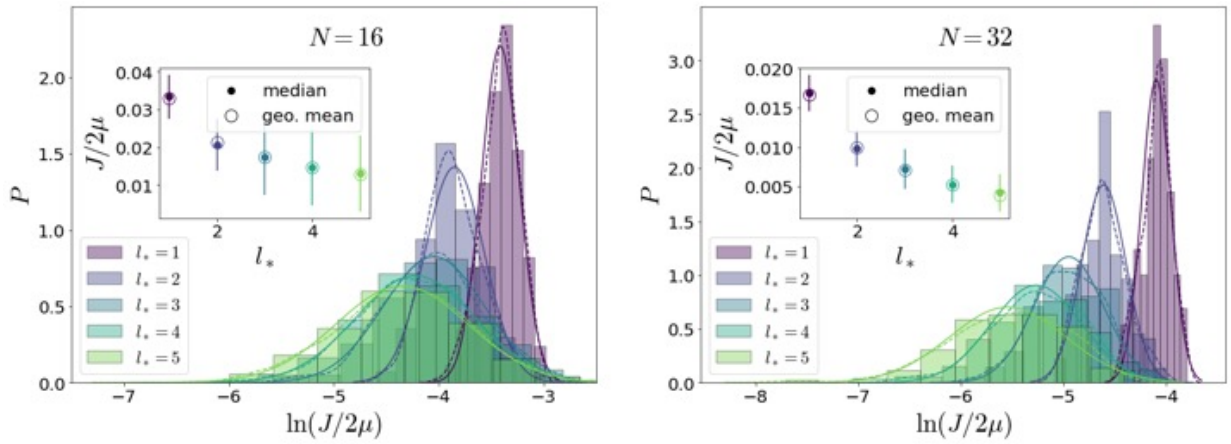

Figure 3.9: Probability distribution of logarithm of the scaled spin current $\ln(J/2\mu)$ of the modified NESS for system size $N = 16$ and $N = 32$. The disorder strength is $h = 2.0$ for both system sizes. Each solid and dashed line represents a continuous probability curve and the best normal distribution fitting for the given parameter, respectively.

sion [228].

A priori, then, one expects DAOE to make the system diffusive. For $\ell_* = 1$ this is what we see (in both Fig. 3.6 and Fig. 3.8): the system has diffusive transport scaling exponent $\chi \approx 1$ for lengths $N \geq 32$. But for $\ell_* \geq 2$ the system appears to converge to superdiffusive transport powers $\chi < 1$. We believe this convergence is only apparent: that DAOE induces a quasiparticle scattering length longer than the system sizes $N \leq 256$ we consider. The curious dependence of the exponent on ℓ_* may be a numerical signature of the contribution of different quasiparticle types to transport.

3.5.3 Disordered XY Model

Finally, we explore spin transport in the disordered XY model under strong operator weight dissipation. We consider a Hamiltonian

$$H = \sum_j \left(\sigma_j^x \sigma_{j+1}^x + \sigma_j^y \sigma_{j+1}^y\right) + \sum_j h_j \sigma_j^z \tag{3.17}$$

where the fields h_j are chosen uniformly at random $[-h, h]$. We consider $0.5 \leq h \leq 3.5$; for larger disorders, NESS convergence times are too large to be tractable. We take the operator weight dissipation large: $\gamma = 10.0$ at timestep $\tau = 1.0$.

The disordered XY model maps to a disordered free-fermion model (cf App. B.1), so it is an Anderson insulator. The system's dynamics are determined by its Anderson orbitals (localized single-particle eigenstates). The Anderson orbitals have characteristic width

$$\xi \sim \begin{cases} 24/h^2 & h \lesssim 2.0 \\ 1/\ln h & h \gtrsim 2.0 \ . \end{cases} \tag{3.18}$$

To the extent that an isolated Anderson insulator transports charge, it does so coherently: charge tunnels into an Anderson orbital on the left end and out from the same orbital on the right end. Because orbitals are localized, these tunneling rates are small; additionally, the Anderson orbitals' onsite amplitudes are log-normally distributed, so the tunneling rates (hence conductivities) will likewise be log-normally distributed.

But suppose sites in the middle of the Anderson insulator are connected to a bath. The bath can cause incoherent transitions between Anderson orbitals because the dissipation superoperator

will have matrix elements between Anderson orbital density matrices $|\varepsilon_j\rangle\langle\varepsilon_j|$, $|\varepsilon_k\rangle\langle\varepsilon_k|$ for nearby orbitals $|\varepsilon_j\rangle, |\varepsilon_k\rangle$. These matrix elements vary. But the resulting distribution of local resistivities has finite moments, so the system is diffusive—not subdiffusive (Other behavior is possible. If a fraction $p < 1$ of sites are connected to a bath, for example, the system will have runs of sites with no dephasing; runs of a given length will be exponentially rare but have exponentially large resistance, giving subdiffusion [58].).

The DAOE projection operator $\mathcal{D}_{\ell_*,\gamma}$ of Eq. 3.7 likewise causes incoherent transitions between Anderson orbitals, because it likewise has matrix elements between Anderson orbital density matrices $|\varepsilon_j\rangle\langle\varepsilon_j|$, $|\varepsilon_k\rangle\langle\varepsilon_k|$. But (at least for the large disorder) these matrix elements are only nontrivial for orbitals centered at sites j, k separated by at least ℓ_*, and they will go as the amplitude of an orbital at some site a distance ℓ_* away from the orbital's center site. Charge therefore tunnels a distance ℓ_* at rate Ψ_{ℓ_*} where Ψ_{ℓ_*} is a log-normally distributed random variable with mean

$$\mu = e^{-\ell_*/\xi} \tag{3.19}$$

and some variance σ determined by ℓ_* and the disorder properties. This gives a local diffusion coefficient $D \sim \ell_*^2 \Psi_{\ell_*}$ and a resistivity

$$\rho \sim D^{-1} \sim (\ell_*^2 \Psi_{\ell_*})^{-1}. \tag{3.20}$$

We can therefore think of such a system—an Anderson insulator evolved under DAOE—as a network of resistors of length ℓ_* and log-normal random resistance $R_j = \ell_* \rho$ distributed per

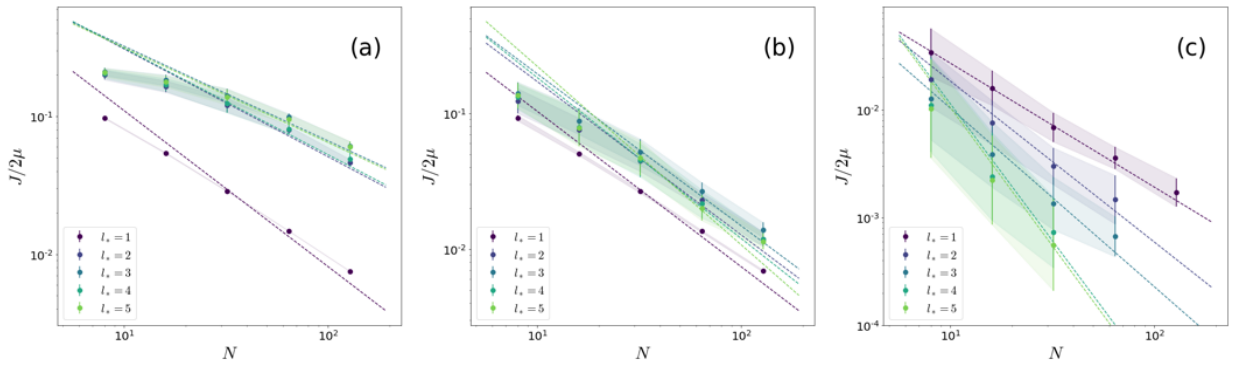

Figure 3.10: The geometric mean and the associated error bar of spin current of the disordered XY model as a function of system size N. Each panel shows the result of different disorder strengths ((a) $h = 0.5$, (b) $h = 1.0$, (c) $h = 3.0$). The dashed lines are the best power law fittings corresponding to geometric means from the last three data points.

3.20 and 3.19. The total resistance is

$$R = \sum_{n=1}^{N/\ell_*} R_n. \tag{3.21}$$

If the system is long enough, it will behave diffusively. The log-normal distribution has finite moments, so the resistance will be

$$\langle R \rangle \propto N/\ell_*, \tag{3.22}$$

with the constant given by the mean of the log-normal distribution, and the realization-to-realization variation will shrink as $1/\sqrt{N/\ell_*}$. But for short systems, the sum 3.21 is dominated by the largest individual resistance, which scales as

$$R_{\max} \sim e^{\mu + \sqrt{cN}} \tag{3.23}$$

for the mean μ of 3.19 and some ℓ_* and h-dependent c (This comes from standard results on extreme values of the normal distribution (see [255] example 1.1.7.)). Consequently, an ensemble

of systems may look subdiffusive, even across more than a decade of length, even though the systems become diffusive in the large-size limit.

In Fig. 3.9 we show the distribution of log end-to-end steady-state currents for two different system lengths, $N = 16$ and $N = 32$. In each case, a kernel density estimator (solid line) matches a best-fit Gaussian (dashed line) well, and the median and geometric mean agree closely. In each case the median current decreases as ℓ_* increases, but for $\ell_* \geq 3$ the decrease is more noticeable in the $N = 32$ distribution than the $N = 16$ distribution. This indicates that at $N = 16$ at least we are seeing substantial finite size effects.

In Fig. 3.10 we show the geometric mean currents

$$J_{\text{geom}} = \exp\{\langle \ln J/2\mu \rangle\} \tag{3.24}$$

as a function of system size, across ℓ_* and disorder width h. In the limit of large system size, the distribution of total resistances will show central-limiting behavior, and approach a Gaussian with variance increasing slower than the mean. But at the system sizes we treat the distribution is still broad (e.g. in Fig. 3.9 the $N = 32, \ell_* = 5$ current distribution spans about a decade). The arithmetic mean is therefore less enlightening than the geometric mean. The geometric mean currents appear to show power law scaling in system size—but this is because our data only span slightly more than a decade.

Fig. 3.11 shows convergence times as a function of h for system size $N = 32$. We consider the simulation converged in time when

$$\frac{1}{J}\frac{dJ}{dt} < 10^{-4} \tag{3.25}$$

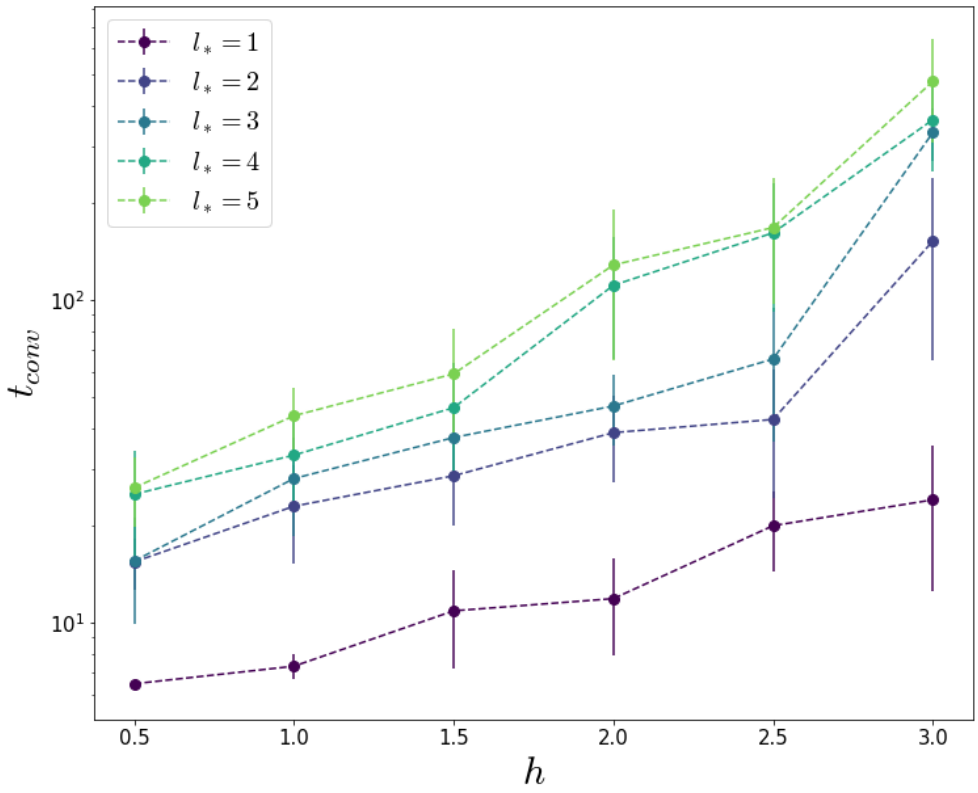

Figure 3.11: Convergence time for various operator cut-off lengths ℓ_* and the disorder strengths h for fixed system size $N = 32$.

where time is in units of coupling, and the site-to-site variation in current is less than the average across sites. We see a broadly exponential increase in convergence times with h.

3.6 Discussion

We have used non-equilibrium steady states of boundary-driven Lindblad systems to study how operator weight dissipation changes the scaling behavior of transport. We used as our test cases members of the XXZ family of models in three flavors: chaotic, integrable, and Anderson localized. We found that operator weight dissipation pushes the system towards diffusive transport scaling—except to the extent that the dissipation preserves some crucial symmetry or conserved quantity of the underlying dynamics. In the clean XXZ case at the isotropic point

($\Delta = 1$), simulations with DAOE display anomalous transport similar to the underlying integrable dynamics, and at the free-fermion integrable point ($\Delta = 0$) it displays ballistic transport for $\ell_* \geq 2$ because it preserves the underlying model's single-particle momentum conservation and resulting Drude peak. In the disordered XY model, DAOE simulations resemble the localized behavior of the underlying system to the extent that DAOE preserves the system's Anderson orbitals.

Our central result is that even quite strong operator-weight dissipation does not necessarily change the scaling behavior of a system's transport, provided it preserves the system's symmetries. From an effective field theory point of view this is a gratifying result. The premise of the effective field theory approach to hydrodynamics is that a system's dynamics are characterized up to some $O(1)$ numbers by its symmetries and related conservation laws; our work tests precisely this contention. Moreover, since recent numerical methods for hydrodynamics (including DAOE, but also a number of other methods) also take this as their premise, our work offers supporting evidence for that approach.

But our results for the isotropic point of the XXZ model remain a mystery from this effective field theory point of view. From that point of view one would expect the operator-weight dissipation to break integrability and consequently turn the system into a generic system characterized simply by its symmetries, in this case $SU(2)$; such a system would be diffusive. We found that the superdiffusion at the isotropic point appeared robust to operator-weight dissipation, though this may have been a finite-size effect.

One interesting direction is to extend the method to fermionic systems where the length and/or weight of a fermionic operator string can be defined in a similar way to the spin case. As an application, it would be interesting to revisit free-fermion integrable or near-integrable models

with technology, without the extra complications of a Jordan-Wigner transformation. This sort of operator weight dissipation might be applied to non-local models like the SYK model as well, although tensor network methods are not currently available in that case (but see [256] for recent progress in the context of sparse models).

It is also interesting to compare and contrast DAOE with more physical models of dissipation. For example, for various one-dimensional spin models, strong enough dephasing results in normal diffusion for various original transport types including ballistic transport to localization [32, 58, 257–259]. We find that the effect of operator weight dissipation on open system dynamics is closely tied to the symmetries it preserves.

3.7 Acknowledgements

CDW and YY thank the U.S. Department of Energy (DOE), Office of Science, Office of Advanced Scientific Computing Research (ASCR) Quantum Computing Application Teams program, for support under fieldwork proposal number ERKJ347.

Chapter 4: Temperature Dependece of Energy Transport in the $\mathbb{Z}_3$ Chiral Clock Model

This chapter is based on the publication 'Temperature dependence of energy transport in the $\mathbb{Z}_3$ chiral clock model' by Yongchan Yoo and Brian Swingle, published as Phys. Rev. B 109, 235104 (2024).

4.1 Overview

We employ matrix product state simulations to study energy transport within the non-integrable regime of the one-dimensional $\mathbb{Z}_3$ chiral clock model. To induce a non-equilibrium steady state throughout the system, we consider open system dynamics with boundary driving featuring jump operators with adjustable temperature and footprint in the system. Given a steady state, we diagnose the effective local temperature by minimizing the trace distance between the true local state and the local state of a uniform thermal ensemble. Via a scaling analysis, we extract the transport coefficients of the model at relatively high temperatures above both its gapless and gapped low-temperature phases. In the medium-to-high temperature regime we consider, diffusive transport is observed regardless of the low-temperature physics. We calculate the temperature dependence of the energy diffusion constant as a function of model parameters, including in the regime where the model is quantum critical at the low temperature. Notably, even

within the gapless regime, an analysis based on power series expansion implies that intermediate-temperature transport can be accessed within a relatively confined setup. Although we are not yet able to reach temperatures where quantum critical scaling would be observed, our approach is able to access the transport properties of the model over a broad range of temperatures and parameters. We conclude by discussing the limitations of our method and potential extensions that could expand its scope, for example, to even lower temperatures.

4.2 Introduction

The study of non-equilibrium quantum systems poses a central challenge across various fields of many-body physics, encompassing classic problems in solid-state systems to more recent problems arising in the dynamics of quantum information [12, 184, 201, 260–264]. Here we are interested in a classic problem in the physics of transport, namely the determination of energy currents induced by an applied temperature bias. This problem sits on the border of the broad domain of non-equilibrium physics because the current carrying steady state is a non-equilibrium state, but a notion of approximate local equilibrium still prevails in the system at late time. While the investigation of energy transport is a longstanding endeavor, it remains a challenging problem even in the case of locally interacting one-dimensional systems [177, 265], especially if one wishes to probe a temperature regime well below the microscopic energy scales. This paper focuses on energy transport in the context of a non-integrable quantum spin chain, with the specific goal as accessing lower temperatures than previously studied.

To introduce our approach, we first recall that for the simpler problem of equilibrium physics, tensor network approaches, especially matrix product state (MPS) techniques, have

demonstrated significant efficacy in one dimension [86, 180, 266, 267]. However, when considering dynamics of a non-integrable system, one generically expects entanglement to grow linearly with time. This growth in turn implies an exponential growth of the requisite bond dimension needed to capture the full state. This is a significant computational barrier, especially since the transport physics of interest is a long-time "hydrodynamic-like" property of the system. New approaches have been developed to surpass this entanglement obstacle by devising altered dynamical principles that diverge from the microscopic unitary evolution [184, 189, 268–270], and open quantum system methodologies, which employ an explicit external driving force to guide a system towards its non-equilibrium steady state (NESS), have emerged as a promising avenue for investigating transport properties [32, 33, 46, 144, 271–274]. On physical grounds, directly connecting a system to a reservoir is anticipated to diminish the entanglement within the system, making it plausible to investigate transport phenomena through a low-entanglement simulation by utilizing an open quantum system methodology.

Nevertheless, while the broad outlines of the open system approach are well established, an important open question is how to design reservoirs which are both efficiently implementable and can drive the system to a wide range of temperatures. There are two broad ways to approach this problem. The first approach involves establishing a reservoir configuration of infinite size and then eliminating the reservoir's degrees of freedom through a tracing-out process. However, the resultant master equation exhibits temporal non-locality, and its memory kernel has so far proven overly intricate for practical solvability [275]. For instance, the Redfield master equation [276], which is derived through additional approximations, remains challenging to practically solve.

A second more practical strategy involves searching for an evolution equation for the density matrix of the system that can effectively drive the system towards a controllable equilibrium

state or non-equilibrium steady state (NESS). In this situation, one uses the Lindblad master equation [24, 25] with specially chosen jump operators which hopefully drive the system to the desired state. If this is true and if the Lindblad equation can be efficiently solved within a space of low bond dimension matrix product states, then one has a practical method to extract transport physics, as well as other observables. In the case of a system exhibiting good thermalization properties, opting for appropriate local Lindblad operators (which represent the influence of reservoirs) exclusively at the edges of the system leaves the bulk dynamics largely unmodified while restricting the entanglement growth to a manageable amount. It has been argued that many systems, including non-interacting and interacting fermions as well as strongly interacting spins, can achieve thermalization under the condition of infinitely large and weakly damped reservoirs [4, 46]. However, achieving reliable thermalization at low temperatures is made difficult by various obstacles, such as mismatches between the bath scales and the system's energy scales and the possible slow approach to the NESS. Hence, designing jump operators that can effectively drive the system to equilibrium remains a challenging task, one that calls for exploration and experimentation.

Here we study energy transport in a $\mathbb{Z}_3$ chiral clock model [277–283] with boundary driving, with a focus on pushing the current methods to their limits. The chiral clock model has been extensively explored from a theoretical standpoint, driven in part by its relevance to a novel experimental setup involving trapped cold atoms [284]. Its low-temperature physics involves a symmetry-breaking quantum phase transition [285], and a prominent aspect of the model is its distinctive property dynamical critical exponent, $z \neq 1$, at criticality [286–288]. While substantial advancements have been made in exploring the phase transition characteristics of the model through both field-theoretical and numerically-based Density Matrix Renormalization Group

(DMRG) approaches [178], the dynamical aspects are less well studied. Prior results on energy transport include a generalized hydrodynamics framework at a critical integrable point [289], a NESS approach involving tailored Lindblad operators with a constant bath temperature [290] and a DMRG approach for the finite temperature thermal conductivity along a line of integrable points [291]. But the generic non-integrable behavior as a function of temperature has not yet been explored. Moreover, in light of recent efforts to push to low temperatures with open system methods, the chiral clock model is expected to be a challenging case, at least near the critical line owing to the nearly gapless low-energy spectrum. A long term goal, which we do not achieve here, is to probe transport in the quantum critical regime. The model is also challenging because the local Hilbert space dimension is 3 as compared to 2 for the spin-1/2 chains in many other studies. Thus the chiral clock model is both interesting and challenging and provides an excellent opportunity to thoroughly assess the capabilities of the tensor-network-based open system approach.

In this study, we explore the finite temperature transport properties of the $\mathbb{Z}_3$ chiral clock model by imposing a temperature gradient across the system, which can be achieved by manipulating the parameters of the bath operators. As observed in typical non-integrable interacting spin-$1/2$ systems, we anticipate that the model will exhibit a NESS featuring approximate local thermal equilibrium and diffusive energy transport. Importantly, we find that while the expanded local state space considerably increases the computational complexity, it remains feasible to apply the approach to systems over a range of temperatures and system sizes to give good estimates of the transport properties in the thermodynamic limit. The system's effective temperature is evaluated using the thermometry method outlined in Ref. [47], which relies on comparing steady-state local density matrices to their thermal equilibrium counterparts, quantified through a measure of

trace distance.

As an initial exploration, we examine the energy transport within the model for several choices of parameters, focusing on relatively high temperatures for the analysis. As shown in Figure 4.1, the parameters we study include regimes where the low temperature physics is gapped and points where it is quantum critical. At these high temperatures, we expect and indeed observe conventional diffusive transport irrespective of the model's symmetries and low energy physics (gapped or critical). Next, focusing on parameters where the low energy physics is quantum critical, we assess the temperature-dependence of the energy diffusion constant by progressively reducing the bath temperature. The effective temperature exhibits a linear correlation with the bath temperature before eventually reaching a non-zero saturation point, comparable to the model's characteristic energy scale, J. As such, reaching sufficiently low temperatures to directly probe the quantum critical physics remains an outstanding challenge in the open system approach. This behavior mirrors our earlier findings obtained through an analysis of smaller system sizes in Ref. [4]. We also note a resemblance between the temperature dependence of the gapless chiral clock model and the chaotic spin-$1/2$ XZ model [47].

This paper is structured as follows. First, the $\mathbb{Z}_3$ chiral clock model is introduced in Sec. 4.3. Then, in Sec. 4.4, we outline the boundary open system configuration and methods to estimate the effective temperature and the transport coefficients in question. In Sec. 4.5 we present the finite temperature transport characteristics of the system. Finally, we provide analyses of our findings and explore potential extensions in Sec. 4.6.

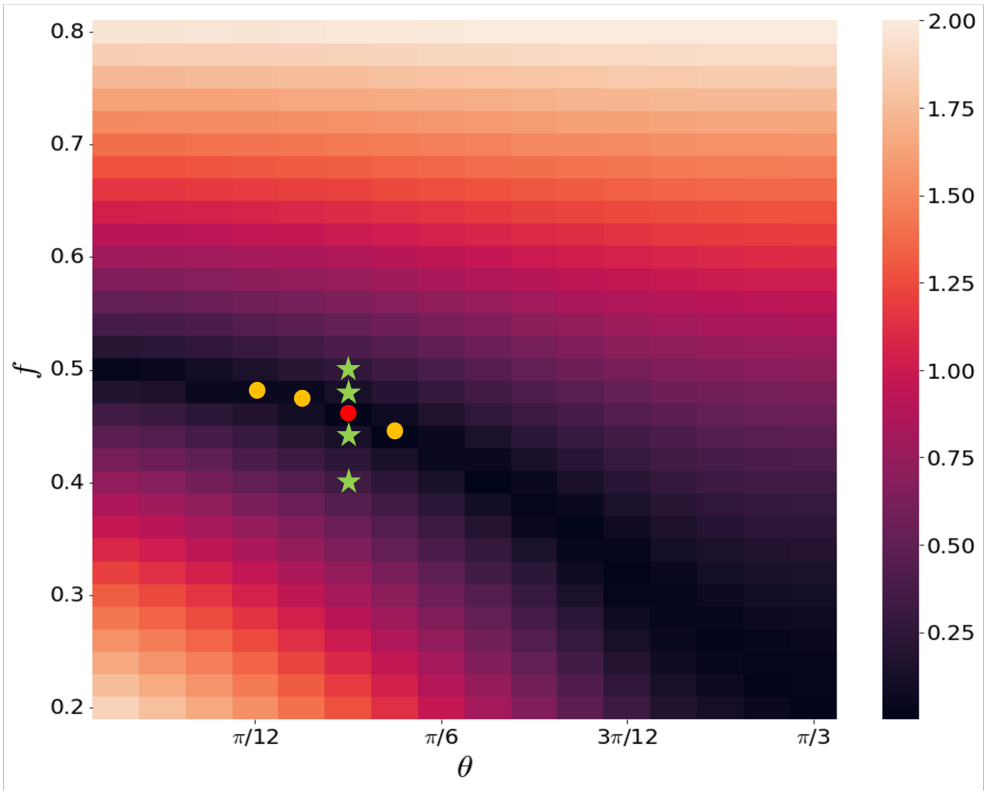

Figure 4.1: The energy gap of the $\mathbb{Z}_3$ chiral clock model for $\phi = 0$. The gap is computed using DMRG on a one-dimensional chain with a length of $L = 200$ and a bond dimension of $\chi = 200$. The depicted black region represents the gapless regime, indicating instances of direct transitions for small θ values and the intermediate incommensurate regime for larger θ. The yellow and red circles in the middle of the map are the chosen critical points of the energy transport study. The green stars represent selected points to study slightly gapped models. In particular, temperature-dependent transport of the model is considered at the red point.

4.3 The $\mathbb{Z}_3$ Chiral Clock Model

We consider a one-dimensional $\mathbb{Z}_3$ chiral clock model (CCM) on a chain with open boundary conditions. The Hamiltonian of the CCM for a total chain length L is given by [286–288]

$$H_{\text{CCM}} = -fe^{-i\phi}\sum_{j=1}^{L}\tau^{\dagger} - Je^{-i\theta}\sum_{j=1}^{L-1}\sigma_j^{\dagger}\sigma_{j+1} + \text{h.c.}, \tag{4.1}$$

where τ_i and σ_i are the local three-state operators at site i. They obey the algebraic relations

$$\tau^3 = \sigma^3 = \mathbb{1}, \quad \sigma\tau = \omega\tau\sigma; \quad \omega = e^{2\pi i/3}. \tag{4.2}$$

We choose the explicit matrix representations

$$\tau = \begin{pmatrix} 1 & 0 & 0 \\ 0 & \omega & 0 \\ 0 & 0 & \omega^2 \end{pmatrix}, \quad \sigma = \begin{pmatrix} 0 & 1 & 0 \\ 1 & 0 & 0 \\ 0 & 0 & 1 \end{pmatrix} \tag{4.3}$$

for τ and σ analogous to the Pauli matrices σ_z and σ_x, respectively, for spin-1/2 systems. From this point of view, the $\mathbb{Z}_3$ chiral clock model can be seen as an extension of the transverse field Ising model, featuring a larger local Hilbert space of dimension $d = 3$. The Hamiltonian presented above contains four parameters: the on-site spin flip strength f, the two-site interaction strength J, and the two "chiralities" ϕ and θ.

These many parameters contribute to the model's intricate phase diagram. As implied by its name, the model exhibits a global $\mathbb{Z}_3$ symmetry, which is implemented by the unitary operator

$\mathcal{G} = \prod_i \tau_i$. Similar to the behavior of the transverse field Ising model, each coupling strength, f and J, defines distinct regions within the phase diagram. Consequently, when $f \gg J$, one can anticipate a disordered phase, while on the opposite side of the phase diagram with $f \ll J$, a $\mathbb{Z}_3$ ordered phase becomes apparent.

The symmetry properties of the model can be further elucidated by the introduction of three operators, charge conjugation $\mathcal{C}$, spatial parity $\mathcal{P}$, and time reversal $\mathcal{T}$. The following symmetry transformation relations are satisfied by these operators [288]:

$$\mathcal{C}\sigma_i\mathcal{C} = \sigma_i^\dagger, \quad \mathcal{C}\tau_i\mathcal{C} = \tau_i^\dagger, \quad \mathcal{C}^2 = \mathbb{1}, \tag{4.4}$$

$$\mathcal{P}\sigma_i\mathcal{P} = \sigma_{-i}, \quad \mathcal{P}\tau_i\mathcal{P} = \tau_{-i}, \quad \mathcal{P}^2 = \mathbb{1}, \tag{4.5}$$

$$\mathcal{T}\sigma_i\mathcal{T} = \sigma_i^\dagger, \quad \mathcal{T}\tau_i\mathcal{T} = \tau_i, \quad \mathcal{T}^2 = \mathbb{1}. \tag{4.6}$$

The model can have other discrete symmetries depending on the values of parameters ϕ and θ due to the above relationships. When the chiralities are absent ($\phi = \theta = 0$), the model exhibits the presence of all three of these symmetries, leading to the model's reduction to the three-state quantum Potts model [292, 293]. However, when both $\theta \neq 0$ and $\phi \neq 0$, the discrete spacetime symmetry is solely a composite of $\mathcal{CPT}$, with no individual symmetry remaining intact. In contrast, either the $\phi = 0$ or $\theta = 0$ scenario retains separate time-reversal and parity symmetries, wherein the charge conjugation operator $\mathcal{C}$ is coupled with either $\mathcal{P}$ or $\mathcal{T}$, respectively. Notably, the spatial chirality θ introduces incommensurate floating phases in relation to the periodicity of the underlying lattice [294].

In addition, there is a special parameter curve $f\cos(3\phi) = J\cos(3\theta)$ where the CCM becomes integrable [295] and it further exhibits what is known as "superintegrability" at $\phi =$

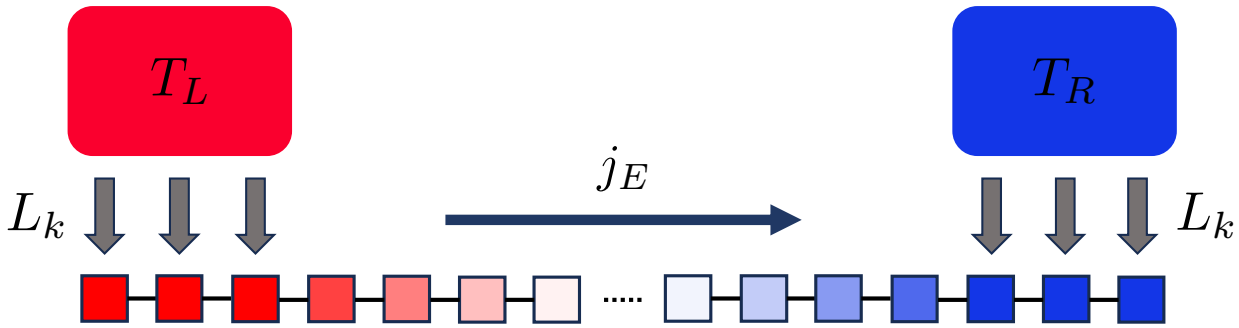

Figure 4.2: Illustrative representation of the boundary-driven transport setup. Thermal baths with temperatures T_L and T_R are produced at both ends of the system using the Lindbladian operator L_{jk}. In the depicted scenario, 3-site bath operators are shown, facilitating the establishment of the non-equilibrium steady state. The energy current j_E traversing the system is an outcome of this dynamic arrangement.

$\theta = \pi/6$ [296, 297]. Integrability offers a broad range of methods to manipulate the model, but transport properties near the integrable point are not fully understood.

For the sake of simplicity, our study focuses exclusively on the CCM with $\phi = 0$ and $f = 1 - J$. This specific choice has been extensively examined in previous literature [287, 288]. Notably, we consider several parameter choices for which the low energy physics is quantum critical, consistent with the phase transitions established in Ref. [287]. Because the low energy physics is gapless, we expect that probing low temperatures using the open system approach may be challenging, similar to our previous investigations (Ref. [4]). We consider a variety of regimes to verify that the low energy physics does not strongly affect the transport physics at moderate to high temperature. The parameters we study are overlayed on a map of the energy gap in Figure 4.1.

4.4 Methods

4.4.1 Tensor Network Simulation Setup

The non-equilibrium configuration depicted in Fig. 4.2 consists of a one-dimensional chain subjected to Markovian boundary driving, with two bath assemblies connected at its ends. We model the baths using specially chosen jump operators L_k at either end of the chain, with the left and right bath temperatures being separately tunable. This situation is well-characterized by the GKLS Master equation [24, 25]

$$\frac{d\rho}{dt} = \mathcal{L}(\rho) \equiv -i[H, \rho] + \sum_{jk} \left(L_{jk} \rho L_{jk}^\dagger - \frac{1}{2} \{ L_{jk}^\dagger L_{jk}, \rho \} \right), \tag{4.7}$$

where H is the Hamiltonian of the system and L_{jk} are Lindblad bath operators, which encode the information of the interaction between the system and the environment, that exclusively operate on the two ends of the one-dimensional chain. The form of these operators is guided by the thermal equilibrium states of the system's Hamiltonian. When the Hamiltonian H is absent, these operators drive the rightmost and leftmost M end sites (bath sites) of the system toward a thermal state ρ_B at temperature T_B. A comprehensive description of an arbitrary-size version of L_{jk} is provided in an Appendix of our previous paper [4].

We start by decomposing the Hamiltonian into three components as $H = H_S + H_B + gH_I$. Here, H_S, H_B, and H_I represent the sub-Hamiltonians that characterize the system (bulk), bath (both left and right), and their interaction, respectively. In the above decomposition, g is a dimensionless coupling which governs the degree of interaction between the system and the

environment. We set $g = 1$ throughout this study to enhance the convergence in time to the NESS. Further elaboration on this matter can be found in Sec. **??**.

Consider first the case where $T_L = T_R = T_B$. On general grounds, since the bath sites are only driven to thermal equilibrium when $g = 0$ and since the bath is not infinitely large, we do not expect the full system to be in thermal equilibrium at temperature T_B in the steady state. However, as long as the system is still driven to a thermal state and we can determine and tune the system temperature, this setup is still useful. Within our configuration, the temperature gradient is generated by maintaining different temperatures for the left and right bath operators. Specifically, we assign $T_L = 1.2T_B$ to the left and $T_R = 0.8T_B$ to the right bath operator. This deliberate difference in temperature at the two ends is chosen to provide a clear energy profile and energy current. Simultaneously, it ensures a slow variation in the bulk effective temperature along the chain. So long as this variation is small compared to the correlation length in the NESS, we expect a good notion of local thermal equilibrium. Moreover, a small local gradient ensures that the local response, i.e. the induced energy current, is accurately modeled as a linear response.

We emphasize that T_B will not in fact correspond to the local temperature at the ends chain in the uniform case with $T_L = T_R = T_B$. Similarly, in the biased case, neither T_L nor T_R will correspond to the local temperature at the ends of the chain (see the inset of Figure 4.4(b) for the relationship between T_B and the effective temperature in the middle of the chain). However, as parameters in the jump operators, T_L and T_R do allow us to dial the energy density at either end of the chain, at least within some large range. We separately directly determine the local effective temperature as described just below.

Next, we describe how to find the actual NESS. By considering the superoperator $\mathcal{L}$, which encodes both coherent and dissipative dynamics, the NESS ρ_{NESS} corresponds to a unique fixed

point solution where $d\rho_{\text{NESS}}/dt = 0$ in Eq. (4.7). It is important to note that while there is often a unique NESS solution, this is not always true [251] and the approach to the NESS can be slow even when it is unique. In particular, when jump operators only act on the system's boundary, we can expect many long-lived quasi-steady states. Mathematically, the NESS is equivalent to the limit of the solution of the master equation as time approaches infinity: $\rho_{\text{NESS}} = \lim_{t\to\infty} \rho(t)$. While some exceptions exist, such as cases involving non-interacting [61,62] and strongly-driven systems [65, 298–301], it remains challenging to directly solve the complete equation for exact NESS solutions in general. However, for the sort of one-dimensional system we are considering, tensor network methods provide a powerful set of tools to represent and evolve the density matrix.

For open quantum system simulations, the vectorization of the density matrix proves highly advantageous for representing the given problem within an expanded Hilbert space [80,302,303]. This approach involves a superket state, denoted as $|\rho\rangle$, which directly signifies the associated density matrix as a vector within the operator Hilbert space. Simultaneously, two different physical operators X and Y can operate on ρ via $|X\rho Y\rangle = Y^T \otimes X|\rho\rangle$. Within this framework, the Lindbladian operator described in Eq. (4.7) is transformed into an equivalent Liouvillian superoperator

$$\begin{aligned}\mathcal{L} = &-i\left(I\otimes H - H^T\otimes I\right)\\ &+\sum_\nu\left(L_\nu^*\otimes L_\nu - \frac{1}{2}\left(I\otimes L_\nu^\dagger L_\nu + L_\nu^T L_\nu^*\otimes I\right)\right).\end{aligned} \tag{4.8}$$

Using Eq. (4.8) as a starting point, the time evolution in the expanded Hilbert space can be realized through the application of the Time Evolving Block Decimation (TEBD) algorithm [76, 142] with the superoperator and superket state. To discretize the time evolution operator $e^{\mathcal{L}t}$, we

choose the second-order Suzuki-Trotter decomposition [84,85,180] with a time step of $\delta t = 0.05$. The cumulative error arising from these approximations remains sufficiently negligible for the physical parameters employed in our investigation. Given the non-integrable nature of the model, we expect a unique NESS but the convergence time can depend greatly on the initial state. We find it is quite useful to consider an infinite temperature initial state, which is then slowly evolved to the biased finite temperature NESS of interest. The calculation of the NESS can require a considerable amount of time, depending on the simulation parameters. For the parameters considered here, we found that a simulation time of approximately $t \sim 2000$ generally yields robust convergence. Additional details regarding the simulations are available in Appendix C.1.

4.4.2 Local Temperature

Utilizing the tensor network simulation elucidated in the preceding section, we first obtain the NESS of the system for a given set of parameters. Next, given our focus on transport properties as a function of temperature, it becomes imperative to deduce the effective temperature associated with the resulting NESS. As we mentioned, owing to the intricate interplay between the system and its bath, the effective temperature can diverge from the bath temperature T_B. One straightforward method to measure the effective temperature involves comparing the final NESS with the Gibbs state at a given temperature, which entails quantifying the dissimilarity between the two states. This approach becomes viable upon the introduction of a notion of local temperature [304–308].

We use an approach which allows for an estimation of the effective temperature of the system provided that the system is in local thermal equilibrium within the NESS [47]. The

method considers the reduced density matrix ρ^A_{NESS} of a small local subregion A of the NESS. We also the analogous reduced density matrix $\rho^A_{\text{thermal}}(T)$ obtained by specifying a global thermal state at temperature T for the entire system. We then search for the value of T which minimizes the trace distance, $K\left(\rho^A_{\text{NESS}}, \rho^A(T)\right)$, between these two states. The trace distance is given by

$$K\left(\rho^A_{\text{NESS}}, \rho^A(T)\right) = \frac{1}{2}\,\text{Tr}\left(\sqrt{\left(\rho^A_{\text{NESS}} - \rho^A(T)\right)^2}\right). \tag{4.9}$$

and we vary T to minimize this distance measure. This procedure provides a notion of local temperature and tells us how far from local equilibrium the NESS is. Moreover, if the global NESS state happens to be exactly thermal (including the ground state), the procedure will always return the correct global temperature. Physically, we can view this approach as a kind of gradient expansion as discussed in Ref. [47]. The trace distance is a particularly nice comparison tool as it provides an upper bound on the difference in expectation values for any local obserbable [272].

In our calculations, we chose a pair of adjacent sites as the subsystem A, denoted as $(i, i+1)$. So by dialing i through the chain, we can assign a local temperature to each pair of sites. This choice is not only computationally expedient but also ensures the preservation of a consistent and evenly distributed local temperature across the central region of the system. The temperature at the center of the system, denoted as T_S, can be regarded as a representative temperature for the system, derived from the NESS. The expression for T_S is given by:

$$T_S = \arg\min_T K\left(\rho^{\left(\frac{N}{2},\frac{N}{2}+1\right)}_{\text{NESS}}, \rho^{\left(\frac{N}{2},\frac{N}{2}+1\right)}(T)\right). \tag{4.10}$$

4.4.3 Transport Coefficients

The NESS serves as a basis for computing the expectation values of any designated local operator. In particular, we can evaluate local expectation values of currents and energy densities and thereby obtain the transport characteristics. For instance, in a scenario where a system exhibits a locally conserved quantity $Q = \sum_i Q_i$, the corresponding local current j_i can be computed utilizing both the continuity equation and Heisenberg's equations of motion:

$$\frac{\partial Q_i}{\partial t} = -i\left[Q_i, H\right] = -(j_i - j_{i+1}). \tag{4.11}$$

We consider the total energy $E = \sum_i E_i$ as the conserved quantity of the model Eq. (4.1), where the local energy operator is represented by the three-site operator

$$E_i = -f\tau_i - \frac{Je^{i\theta}}{2}\left(\sigma_{i-1}\sigma_i^\dagger + \sigma_i\sigma_{i+1}^\dagger\right) + \text{h.c.}, \tag{4.12}$$

with the chiral parameter ϕ set to 0. Through a series of algebraic computations employing Eq. (4.11), one can derive the corresponding energy current operator $j_{E;i}$. This operator can be expressed as a combination of two distinct two-site operators situated at the site $(i, i+1)$:

$$j_{E;i} = i\frac{fJe^{i\theta}}{2}\left(j_{E;i}^1 + j_{E;i}^2\right) + \text{h.c.} \tag{4.13}$$

$$j_{E;i}^1 = (\omega - 1)\,\sigma_i\,(\tau_i + \tau_{i+1})\,\sigma_{i+1}^\dagger \tag{4.14}$$

$$j_{E;i}^2 = \left(\omega^2 - 1\right)\sigma_i\left(\tau_i^\dagger + \tau_{i+1}^\dagger\right)\sigma_{i+1}^\dagger \tag{4.15}$$

We can appeal to Fourier's law as a model of the transport properties. In the context of

diffusive energy transport, when an energy bias $\Delta E = \langle E_L \rangle - \langle E_R \rangle$ is maintained across the system, where $\langle E_{L,R} \rangle$ denotes the fixed energy density at the left and right ends respectively, an energy current will be induced in the steady state. Using a continuum approximation with a slowly varying average energy density, the energy current $\langle j_E \rangle(x)$ is related to gradients in the profile of energy density $E(x)$ by

$$\langle j_E \rangle(x) = -D(E(x)) \frac{dE}{dx}. \tag{4.16}$$

The current must be independent of x in steady state, so integrating both sides of the above equation gives

$$L\langle j_E \rangle = -\int_{\angle E_R \rangle}^{\langle E_L \rangle} dE D(E) = -\overline{D} \Delta E. \tag{4.17}$$

In the second equality, we introduced $\overline{D}$ which is the diffusivity averaged over the energy window from $\langle E_R \rangle$ to $\langle E_L \rangle$. Thus we can write

$$\langle j_E \rangle = -\overline{D} \frac{\Delta E}{L}, \tag{4.18}$$

with L representing the length of the system. We conclude that the current can be studied as a function of L with $\langle j_E \rangle \propto 1/L$ diagnosing the presence of diffusive transport dynamics. The actual diffusion constant at a given energy can then be obtained from the local form of Fourier's law, Eq. (4.16).

In practice, the results at the single bond level are slightly noisy and we can get better data by averaging over many sites, as in the integrated Fourier's law, Eq. (4.18). However, $\overline{D}$ will be slightly different from the local $D(E(x))$. To model this, consider the Taylor series

$D(E) = D(E_M) + D'(E_M)(E - E_M) + \cdots$ where $E_M = (E_R + E_L)/2$. Integrating, we find $\overline{D} = D(E_M) + \cdots$. Hence, to first order in gradients, $\overline{D}$ is simply $D(E_M)$ and the midpoint energy E_M occurs in the middle of the segment. Thus, using the integrated Fourier's law only entails a small error from the neglect of second order terms. Given the good approximate linearity of the energy profile after discarding edge sites, and considering our other sources of error, this procedure gives reliable results.

This approach can be expanded to scenarios where the system demonstrates anomalous transport behavior. In such cases, the previously discussed relationship is altered through the introduction of a scaling exponent represented by γ:

$$\langle j_E \rangle = -\overline{D}_\gamma \frac{\Delta E}{L^\gamma} \tag{4.19}$$

In the context of the above equation, we consider a scenario where the only scaling exponent characterizing the transport is γ. This approach accounts for various forms of transport, including: (i) ballistic transport ($\gamma = 0$), (ii) superdiffusive transport $(0 < \gamma < 1)$, and (iii) subdiffusive transport $(\gamma > 1)$, in addition to the conventional diffusive transport $(\gamma = 1)$.

4.5 Results

In this section, we present our findings regarding the finite-temperature transport properties of the $\mathbb{Z}_3$ chiral clock model. The transport coefficients, namely the diffusion constant D and the scaling exponent γ, are determined from a system size of $L = 48$, which is utilized for all calculations in this section of the paper. Regarding the bath size, we predominantly employ a $2-$site bath configuration for the majority of cases. Furthermore, to tackle more challenging

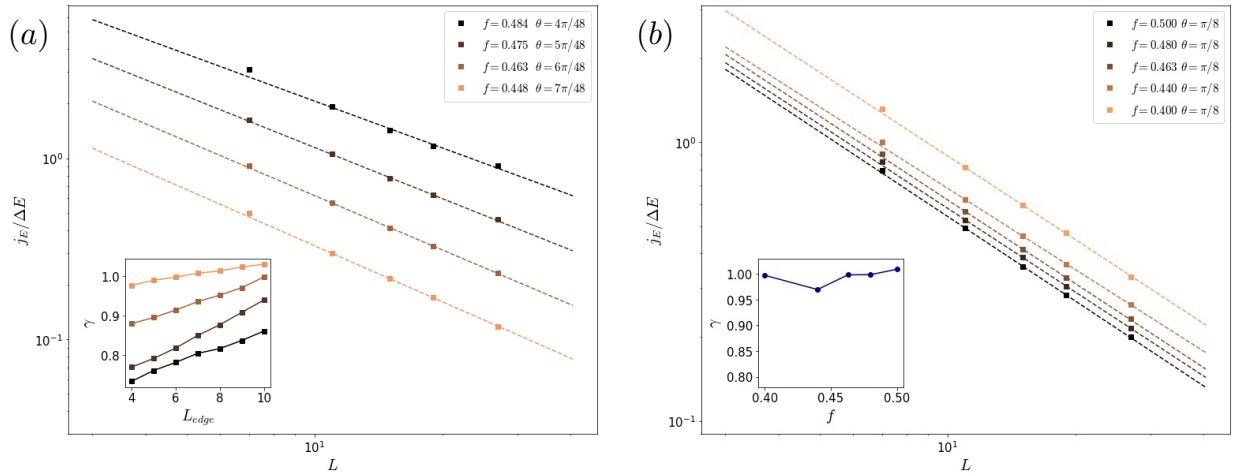

Figure 4.3: The scaled energy current $j_E/\Delta E$ is depicted against the system size L at a high bath temperature of $T_B = 10$. The data is derived from the NESS using selected parameters, encompassing various quantum critical points (a) as well as a slightly gapped regime adjacent to a specific critical point $(f = 0.463, \theta = \pi/8)$ (b). The dashed lines in the plot correspond to the best-fit results based on the generalized Fourier's law $j_E/\Delta E = -D/L^{\gamma}$, where $L_{\text{edge}} = 10$ is considered. The top panel also features an inset illustrating the variation of the scaling exponent γ with respect to L_{edge}. Meanwhile, the bottom panel includes an inset showcasing the extracted scaling exponent γ as a function of f.

scenarios at lower temperatures, we utilize a $3-$site bath setup and compare it to the $2-$site bath setup. Another critical consideration in our simulations is the bond dimension employed to approximate the resulting NESS. For the chosen parameter ranges, a bond dimension of $\chi = 200$ gives a satisfactory level of convergence, considering the order of magnitude of the trace distance. We provide additional details of convergence in this context in Appendix C.1.

4.5.1 High Temperature Transport Properties

We initiate our investigation by examining the energy transport of the model under conditions of high bath temperature. In this context, "high bath temperature" refers to a temperature that is finite yet large enough to establish a well-defined effective temperature across the entire system that is large relative to the model's energy scales. In this study, we set the bath temper-

ature to $T_B = 10$ to define this regime of energy transport. To estimate the system's effective temperature T_S, we employ the trace distance calculation outlined in Sec. **??**. In the case of a suitably large system, we determine that the system size does not significantly influence T_S. This observation allows us to directly employ Fourier's law to derive the transport coefficient at T_S.

The outcomes of the scaled energy current $j_E/\Delta E$ under high-temperature conditions are depicted in Fig. 4.3. Given that the model becomes non-integrable for non-zero chiralities, it is generally anticipated that the selected points in Fig. 4.1 would exhibit diffusive energy relaxation behavior regardless of the low-energy gap structure. We start with the results on energy transport in the gapless regime. We choose specific values of f and θ along the phase transition line, as detailed in Ref. [287]. In the calculation of the expectation values used for estimating transport coefficients, we account for the impact of driving and other boundary effects by excluding a total of $L_{\text{edge}} = 10$ sites at each boundary. Among our chosen points, the influence of finite-size effects from the boundaries is relatively modest for the two cases with larger θ values. In these instances, we observe the anticipated diffusive transport behavior, with a scaling exponent γ closely aligned with the expected value of 1, accompanied by a small uncertainty of approximately ± 0.03. Conversely, the remaining two points with smaller θ values exhibit signs of superdiffusive transport, characterized by scaling exponents around the range of 0.8 to 0.9.

Given our anticipation of normal diffusive transport in cases where $T_S \gg J$ and the expected preservation of symmetrical properties, we proceed to examine how finite-size effects impact the scaling exponent γ by systematically altering the number of sites excluded at the boundaries, denoted as L_{edge}. The inset in Fig. 4.3 (a) emphasizes the gradual rise of γ as the bulk system size becomes more confined to a smaller number of central sites. While not a precise solution, this qualitative examination indicates that strong finite effects tend to exhibit the

superdiffusivity. In general, we observe that the transport coefficients become challenging to compute as we approach the achiral model ($\theta \to 0$). Specifically, both the energy gradient ΔE and the energy current j_E become exceedingly small in this region, preventing the transport coefficients from converging with the chosen simulation parameters.

Next, we delve into the analysis of energy transport within the gapped phases of the model. To explore potential variations in transport properties across the direct phase transition line, we focus on a specific point ($f = 0.463, \theta = \pi/8$), along with two additional points sharing the same θ value from both the disordered and $\mathbb{Z}_3$ ordered phases. This particular point demonstrates better convergence compared to smaller θ values and remains sufficiently distant from the intermediate incommensurate phase. Our investigations confirm the prevalence of diffusive energy transport across all the selected points, as depicted in Fig. 4.3 (b). Thus, it appears that the model's transport behavior remains robust, unaffected by the low-temperature physics.

We have also extended our method to investigate scenarios where the gap size is comparable to the energy scale ($\Delta \sim J$). In such cases, the non-integrable model with a larger gap generally exhibits a shorter convergence time [89]. Similar to the situation with small θ values, we observe that the scaling exponent γ (data not shown) gradually converges towards the normal diffusive value. However, the increasing trend of γ is considerably smaller than 1, indicating that convergence of the NESS is affected by other factors, for example, difficulties estimating the gradient of energy and the possible presence of slowly decaying modes in the Liouvillian. Furthermore, it is noteworthy that the trace distance $K(\rho_{\text{NESS}}, \rho(T_S))$ is primarily influenced by T_S. Our observation suggests that as temperature decreases, the trace distance tends to worsen, presenting a challenge in accurately simulating low-temperature physics. While a relatively lower $K(\rho_{\text{NESS}}, \rho(T_S))$ doesn't necessarily ensure the complete reliability of the NESS, it remains a

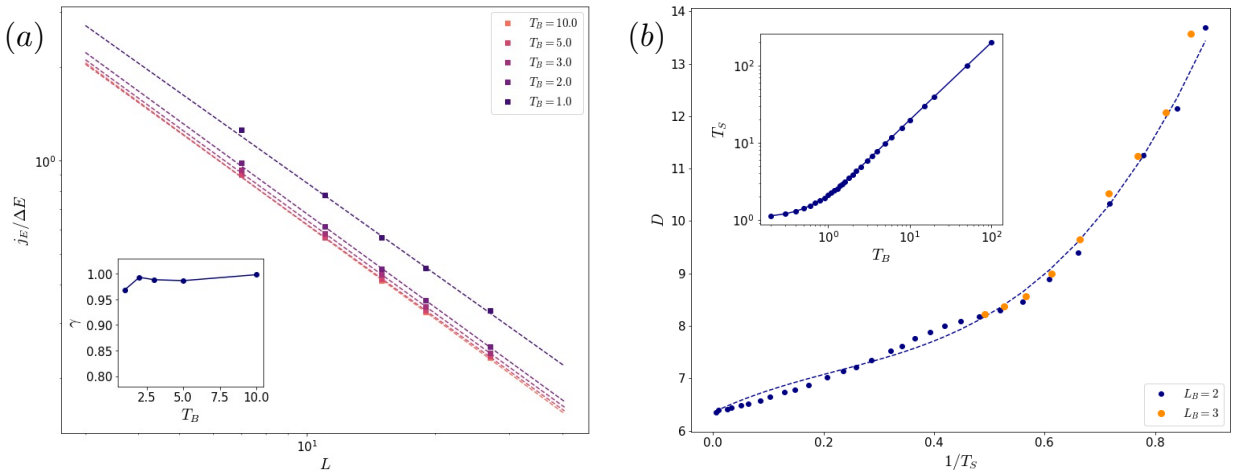

Figure 4.4: (a) The scaled energy current $j_E/\Delta E$ at various bath temperatures is described in relation to the system size L, derived from the NESS results for the parameters $(f = 0.463, \theta = \pi/8)$. The dashed lines illustrate the fitting according to the generalized Fourier's law $j_E/\Delta E = -D/L^{\gamma}$ with $L_{\text{edge}} = 10$. Inset provides a representation of the scaling exponent γ extracted as a function of f. (b) The obtained diffusion constant D from the generalized Fourier's law is shown as a function of the reciprocal of the system's temperature T_S for two different bath sizes. The dashed line represents the best-fit power series curve expressed in Eq. (4.20). The inset plot illustrates the relationship between T_S and T_B.

critical criterion for assessing the accuracy of the calculated transport coefficients, considering the computational complexity involved.

4.5.2 Transport Coefficients at Lower Temperatures

Now, we proceed to the study of energy transport at various temperatures using the same parameter point as in the slightly gapped regime analysis $(f = 0.463, \theta = \pi/8)$. The bath temperature is varied within the range of $0.5 \leq T_B \leq 100$, covering high temperature all the way down to just below the scale of J. The scaled energy currents exhibit a proportional relationship with the inverse of the system size within this temperature range, as shown in Fig. 4.4 (a). This result indicates that diffusive energy transport persists even at temperatures comparable to the energy scale J. Here, the trace distance K serves as an indicator of the transport simulation's

performance, reflecting the deviation between the NESS expectation values and the thermal state. For higher temperatures, we observe $K \sim 10^{-3}$, whereas as we approach lower temperatures, the quality of K deteriorates. As a result, we confine our investigation to temperatures where $K \sim 10^{-1}$ between the steady state and the thermal state, especially for the most challenging simulation scenarios.

Through our thermometry scheme, we observe a linear relationship between the effective system temperature T_S and the bath temperature T_B up to around $T_B \sim 1$. (as seen in the inset of Fig.4.4 (b)). In contrast, as the temperature decreases to lower limits, we notice that the improvement in T_S becomes non-linear and levels off to a nonzero value, which is on the same order of magnitude as the energy scale of the model, as discussed with a smaller system size in our earlier work (Ref. [4]). In prior work, we also observed a connection between the resulting T_S and the implementation of the bath. Specifically, employing a bath with weaker bath-system interactions and larger bath sizes seems to generally enable access to lower temperatures. On the other hand, using a weaker bath can lead to a numerical instability akin to what we observed in the high-temperature transport simulation as θ approaches zero. In general, the relaxation time is associated with the spectral gap $\Delta_{\mathcal{L}}$ of the super-operator. For our non-integrable model in a boundary-driven setup, a perturbation theory approach suggests that the spectral gap scales as $\Delta_{\mathcal{L}} \sim \Gamma g^2/L$ in the limit of $g, \gamma \to 0$ [67,89,309]. Consequently, the relaxation time also follows this scaling behavior. This implies that reducing the strength of bath-system interaction g leads to a notable increase in the time required for the NESS to reliably converge. However, it turns out that this trade-off provides only a marginal advantage in improving the effective temperature for this specific model. Despite implementing a larger bath, similar convergence issues persist, and the relaxation time remains largely unaffected by the bath size. In light of this, we explore the

application of the 3-site bath technique in the low-temperature regime, as illustrated in Fig. 4.4 (b). Notably, expanding the bath size primarily offers an enhancement in the trace distance. Specifically, the trace distance is slightly improved (by approximately 10%) for the 3-site bath calculation when compared to the 2-site bath, while the estimated diffusion constants exhibit consistent agreement between the two cases.

Using the approach of estimating local temperature, we acquire temperature-dependent diffusion constants for the model, as depicted in Fig. 4.4 (b). Given that the effective temperature remains significantly higher, making it reasonable to disregard any potential power-law modifications for the zero-temperature limit, we can maintain the assumption of diffusive energy transport within the low-temperature regime. At high temperatures, the diffusion constant converges to a constant value of approximately $D_\infty \approx 6.3$, exhibiting a notable resemblance to the spin-$1/2$ model outlined in Ref. [47]. Given the system's gapless nature at the quantum critical point, the energy gap Δ holds no significance in relation to its transport properties. Independent of the gap size, a power-series expansion in terms of the inverse temperature is a suitable approach for describing transport in the high-to-intermediate-temperature range, as discussed in Ref. [47]. This expansion is expressed as

$$D = D_\infty \left(1 + \sum_{a \geq 1} \frac{c_a}{T^a}\right). \tag{4.20}$$

At these temperature levels, a power-series fitting curve with $a = 3$ exhibits excellent agreement with the numerical results, indicating that the energy transport of the model falls within the realm of intermediate temperatures. Given that the model lacks a gap at low energy, one could speculate that a new energy scale needs to be introduced to elucidate this trend within the semi-classical kinetic theory for gapped systems [47, 225, 226].

4.6 Discussion

In this paper, we studied the finite temperature energy transport in the non-integrable $\mathbb{Z}_3$ chiral clock model by utilizing tensor network-based simulations of the open quantum system approach. Based on the notion of local temperature, the NESS's effective temperature is evaluated using trace distance-based thermometry. Subsequently, transport characteristics of the model are derived from the NESS using the generalized Fourier's law. In the high-temperature regime, we observe diffusive energy transport regardless of model parameters so long as we consider the non-integrable regime. This confirms our expectation that the low-temperature physics does not directly affect the high-temperature transport. Subsequently, we choose parameters corresponding to a quantum critical point at zero temperature to study the temperature dependence of transport coefficients. With modest computational resources, we are able to probe transport at lower temperatures comparable to the characteristic energy scale, J, of the model. The use of both $2-$ and $3-$site baths yields consistent outcomes in terms of extracting temperature-dependent diffusion constants at this specific point. Notably, the resulting diffusion constant at this point in the phase diagram aligns well with a power-series expansion in terms of inverse temperature.

By dedicating significantly larger computational resources, there is potential to delve into energy transport at even lower temperatures. At much lower temperatures, it becomes intriguing to investigate the emergence of power-law behavior in the temperature dependence of the transport coefficients, which could serve as an indication of quantum critical physics in transport. Reaching sufficiently low temperatures in the open system approach remains challenging, but we have taken some steps towards this goal by investigating gains from using a $3-$site bath. Furthermore, exploring the potential correlation between the model's transport properties and

its chiralities (and consequently its symmetries) at low temperatures offers another compelling avenue for future exploration.

One of the key messages of our work is that the exploration of these fascinating phenomena can be facilitated through carefully engineered bath configurations. In a previous study (Ref. [4]), a minimum attainable temperature for the gapless chiral clock model was suggested. An interesting avenue for future research could involve developing a comprehensive framework for designing optimized baths and dynamics, aiming to overcome this limitation. One possible approach to tackle this challenge involves approximating larger baths using the Product Spectrum Ansatz [310,311] for designing dissipators, as larger baths often lead to improved thermalization. Another potential avenue is the design of unconventional baths [312], including those based on random energy models or random matrix models. These bath models tend to exhibit densely populated spectral densities, suggesting that they could lead to effective thermalization if they can be implemented at a sufficiently large scale. Additionally, exploring similar techniques with other quantum master equations, such as the Redfield equation, could also be considered.

4.7 Acknowledgements

We thank Cris Zanoci for many valuable discussions. Y.Y. acknowledges support from the U.S. Department of Energy, Office of Science, Office of Advanced Scientific Computing Research, Accelerated Research for Quantum Computing program "FAR-QC". We also acknowledge computational resources provided by the Zaratan High Performance Computing Cluster at the University of Maryland, College Park.

Chapter 5: Summary and Outlook

In this dissertation, I aim to deepen my understanding of non-equilibrium dynamics in quantum systems and advance simulation capabilities using state-of-the-art technologies. I emphasize investigating transport phenomena and emergent behavior in one-dimensional spin systems across three distinct scenarios.

In the first scenario, I delve into the non-equilibrium steady state phases of an interacting Aubry-André-Harper model. This model incorporates a quasi-periodic potential, resulting in emergent collective phenomena. This investigation reveals peculiar spin transport patterns and quantum correlation structures, shedding light on the existence of multiple dynamical phases between well-studied thermal and many-body localized phases.

In the second scenario, I explore the impact of operator weight dissipation on transport scaling in various spin models. The results indicate that the effect of dissipation on transport is contingent upon its influence on the system's conserved quantities. When dissipation preserves these symmetries, it upholds the scaling of transport properties. However, if it disrupts these conserved quantities, it leads to diffusive transport scaling.

In the third scenario, I focus on energy transport within the non-integrable regime of the $\mathbb{Z}_3$ chiral clock model. Lindblad operators with adjustable size and temperature are employed to analyze energy transport coefficients at relatively high temperatures, both above gapless and

gapped low-temperature phases. Additionally, the temperature dependence of the energy diffusion constant across various model parameters is explored, including regimes where the model exhibits quantum critical behavior at low temperatures.

In delving into this collection of studies, I've come to appreciate the intricate nature of non-equilibrium dynamics in quantum systems—conceptually rich and technically demanding. Despite the extensive research conducted thus far, there remains a vast landscape of unexplored possibilities and avenues for further investigation and extension. Here, I present a few intriguing subjects that are on my mind.

Boundary-driven open quantum systems tend to be particularly challenging due to the larger dimension of the Hilbert space than closed systems. Tensor network methods exploit the baths' lower entanglement entropy to describe transport properties effectively. Many proposed techniques focus on circumventing issues that arise in such simulations. Hence, gaining a deeper understanding of the typical tensor structures of boundary-driven systems is crucial for designing more efficient methods.

While most open system models rely on approaches similar to MPS, alternative structures like tree tensor networks or neural network states could offer advantages in specific cases. For example, Boltzmann machines, while limited to small systems, can provide insights into the structure of NESS from a different perspective. Similarly, employing multi-scale entanglement renormalization ansatz (MERA) tensor networks could lead to innovative bath schemes for exploring scale-invariant systems, especially quantum critical systems. These advancements could facilitate more efficient implementations of higher-dimensional tensor networks, which are computationally demanding and lack fixed-gauge tensor contractions.

We've delved into operator weight dissipation and its dynamic nature, which naturally ties

into noisy quantum information processing machines. Understanding transport and general dynamic properties of quantum information quantities in dissipative settings that describe experimental platforms is enticing. Additionally, in addition to its practical implications, simulating fundamental models can provide insight into how various dissipation mechanisms affect critical exponents in a universality class.

Another area for improvement is low-temperature transport, where approaching low temperatures poses technical hurdles. Moreover, low temperatures can induce quantum phase transitions, significantly altering the system's transport properties. This complicates estimating transport coefficients as they may depend on multiple functional dependencies. Despite being extremely challenging, probing very low temperatures near quantum criticality may reveal novel physics.

While computational approaches have been the primary focus in various scenarios, microscopic descriptions based on analytical techniques are also important. These studies are of fundamental interest and may elucidate the disparities between isolated and open systems dynamics in a broader context. For instance, there's a theoretical framework for linking open system simulations with linear response theory to determine diffusion constants. Investigating whether such agreement between open-system and linear-response calculations can be achieved would be intriguing.

Appendix A: Supplementary Material for Chapter 2

A.1 Entanglement growth

The two time evolution methods we used have a small discrepancy in their asymptotic scaling exponent γ, in particular, in the regime of weak quasiperiodic potential strength [Fig. 2.4]. We investigate this difference mainly using the bipartite MPO entanglement entropy $\mathcal{S}$, [313] which is defined as

$$\mathcal{S} = -\sum_{i=1}^{\chi} \lambda_i^2 \log(\lambda_i^2). \tag{A.1}$$

Here λ_i is the normalized Schmidt values ($\sum_i \lambda_i^2 = 1$) of the matrix product density operator (MPDO) in the canonical form at the center of the system and χ is the dimension of the Schmidt values at the center. Basically, the dynamics of the MPO entanglement entropy describes the growth of the entanglement in the MPO basis and also estimates the required maximum bond dimension for efficient MPDO simulation.

The truncation of the MPDO associated with the finite bond dimension certainly affects the dynamics in the unitary evolution setting. As shown in the top of Fig. A.1, while the exact result without truncation ($\chi = 4^5 = 1024$ for $N = 10$) for $\mathcal{S}(t)$ increases essentially monotonically, the corresponding plots with truncated bond dimension show a peak at the early time followed by a slow decay to a lower value than the true value. Thus, it is hard to track the exact dynamics of

the system in this regime with moderate bond dimension.

Nevertheless, the diffusive character of the system can still be revealed with a modest bond dimension. The diffusion constant in this case can be extracted from a 'distance' function,

$$\mathcal{P}(t) = \sqrt{\sum_{i=1}^{N} \left(\langle \sigma_i^z(t) \rangle - \frac{S_z}{N} \right)^2}, \tag{A.2}$$

where S_z is the total magnetization of the fully relaxed state. At a long enough time, the distance function relates to the diffusion constant by $\mathcal{P}(t) \propto e^{-\pi^2 t D/N^2}$. As shown in the bottom of Fig. A.1, $\mathcal{P}(t)$ resembles the exact result much better than $\mathcal{S}(t)$ within the same bond dimension range. This indicates that transport properties and their exponents extracted from unitary evolution is reliable while not perfect.

For the Lindbladian setting, in contrast, there may be convergence issue for different initial states we choose. We again turn to the calculation of $\mathcal{S}(t)$ with a number of initial states and find $\mathcal{S}(t)$ of all randomly prepared initial states appropriately converge to the same value in practically accessible time and bond dimension [Fig. A.2]. Therefore, we confirm that the NESS with correct entanglement structure can be efficiently obtained by our method.

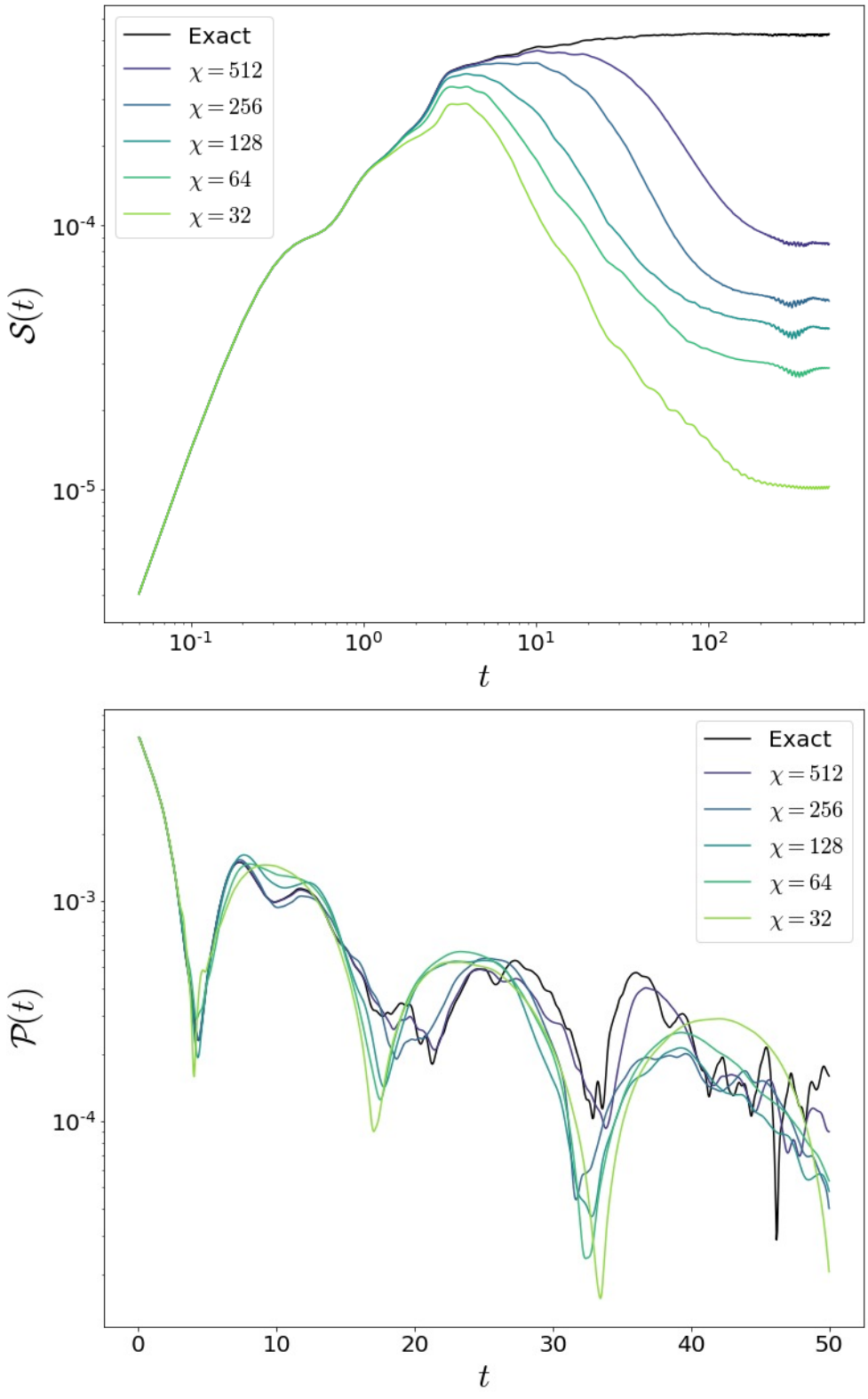

Figure A.1: The bipartite (the half-cut of the system) MPO entanglement entropy $\mathcal{S}(t)$ for different maximum bond dimensions for a small system size ($N = 10$) and $\lambda = 0.0$ (Upper figure). The distance function $\mathcal{P}(t)$ of the same model and parameters (Lower figure).

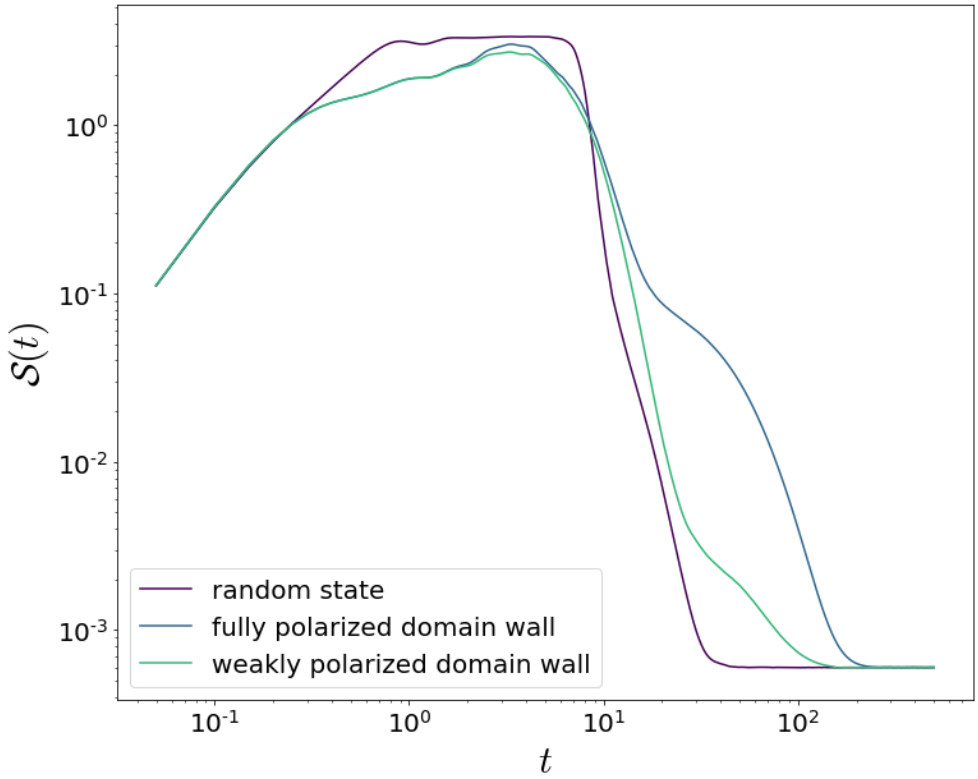

Figure A.2: The bipartite (the half-cut of the system) MPO entanglement entropy $\mathcal{S}(t)$ obtained from different initial superket states for the Lindbladian time evolution and system size ($N = 24$) and $\lambda = 0.0$.

Appendix B: Supplementary Material for Chapter 3

B.1 Conserved Quantities in the XY Model

Here we review the well-known construction of conserved quantities in the XY model obtained via Jordan-Wigner transformation to a non-interacting fermion problem.

In an XY chain of finite length, one can define fermion creation and annihilation operators as

$$c_r^\dagger = \prod_{r'<r} \sigma_{r'}^z \frac{\sigma_r^x + i\sigma_r^y}{2} \tag{B.1}$$

and

$$c_r = \prod_{r'<r} \sigma_{r'}^z \frac{\sigma_r^x - i\sigma_r^y}{2}. \tag{B.2}$$

For $r \neq r'$, it follows directly that

$$\{c_r, c_{r'}^\dagger\} = 0, \tag{B.3}$$

and for $r = r'$, we have

$$\{c_r, c_r^\dagger\} = \frac{1}{4}\{\sigma_r^x - i\sigma_r^y, \sigma_r^x + i\sigma_r^y\} = 1. \tag{B.4}$$

The Hamiltonian,

$$H = -J \sum_r \left(\sigma_r^x \sigma_{r+1}^x + \sigma_r^y \sigma_{r+1}^y\right), \tag{B.5}$$

in the fermion representation becomes

$$H = -J \sum_r \left(c_{r+1}^\dagger c_r + c_r^\dagger c_{r+1} \right). \tag{B.6}$$

From this representation, it is clear that we have an extensive set of conserved quantities given by

$$n_k = c_k^\dagger c_k \tag{B.7}$$

where

$$c_k = \sum_r \frac{e^{ikr}}{\sqrt{N}} c_r. \tag{B.8}$$

It is instructive to convert these conserved quantities back into the spin language. First, we write them in terms of the position basis creation/annihilation operators,

$$n_k = \sum_{r,r'} \frac{e^{-ik(r-r')}}{N} c_r^\dagger c_{r'}. \tag{B.9}$$

Next, we need the following identity for $c_r^\dagger c_{r'}$ valid for $r > r'$,

$$c_r^\dagger c_{r'} = \frac{\sigma_r^x + i\sigma_r^y}{2} \left[\prod_{r''=r'+1}^{r-1} \sigma_{r''}^z \right] \frac{\sigma_{r'}^x + i\sigma_{r'}^y}{2}. \tag{B.10}$$

Hence, a pair of fermion operators separated by ℓ sites gets mapped to a diameter (and weight) $\ell + 2$ spin operator. The conserved quantities are in turn superpositions of all possible pairs of fermion operators.

In the spin language, all non-trivial conserved quantities besides the charge and energy are

superpositions that include many high weight operators. Therefore, any DAOE-like scheme will necessarily badly damage all such non-trivial conserved quantities. The non-interacting character of the model is strongly modified, so it is not surprising that the results tend toward a more generic diffusive behavior.

This analysis must be modified, however, in the presence of quenched disorder. This is because such disorder tends to localize the fermions, and the conserved quantities, which are local in momentum space at zero disorder, are expected to evolve with increasing disorder towards operators which are more local in position space. Indeed, in the extreme limit of very strong disorder, it is just the fermion number on every site that is conserved. In this case, DAOE will not disrupt such local conserved quantities and we can expect the physics of localization to be better captured than the physics at weak disorder. This is essentially what is observed in Fig. 3.9.

B.2 NESS Convergence

B.2.1 NESS Convergence for Different Initial States

In the main text, we assumed that the systems in our study are under the appropriate conditions of the GKLS equation to find the corresponding NESS. Although we have not determined explicit forms of operators in Ref. [251], we tested the uniqueness of NESS with numerical experiments. Here, we prepared different random product density operators as initial states for the XXZ model with $\Delta = 0.5$. The numerically exact calculation for a small system size suggests that those random states converge to the same NESS (Fig. B.2). We believe that similar behaviors are expected for the general XXZ model with different hamiltonian parameters and larger systems with truncations resulting in approximated NESSs.

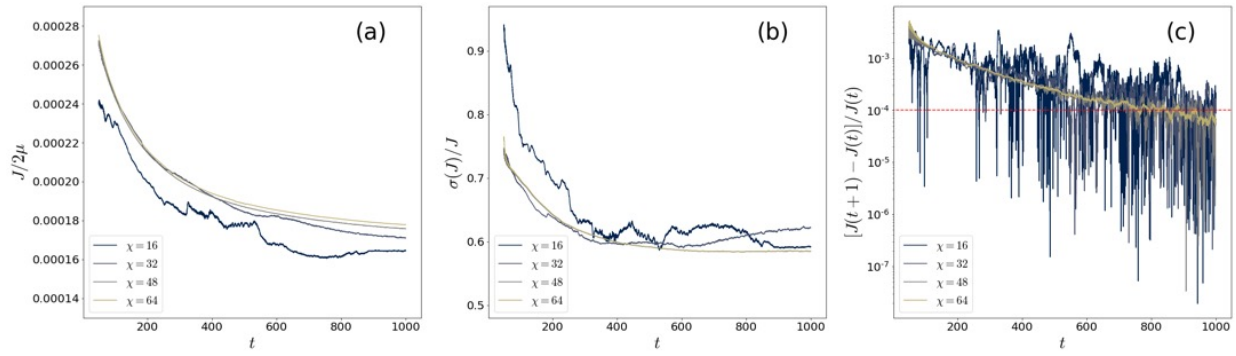

Figure B.1: Convergence in time to an approximate NESS of the disordered XY model with parameters $N = 32$, $h = 3.0$ and $\ell_* = 5$. (a) Current divided by bias as a function of time showing four different bond dimensions. We see approximate convergence in bond dimension. (b) Site-by-site variation of the current normalized by the average current as a function of time. (c) Change in current after one coupling time as a function of time. Our convergence criterion is that this normalized change is less than 10^{-4}. This is achieved after approximately $t = 800$.

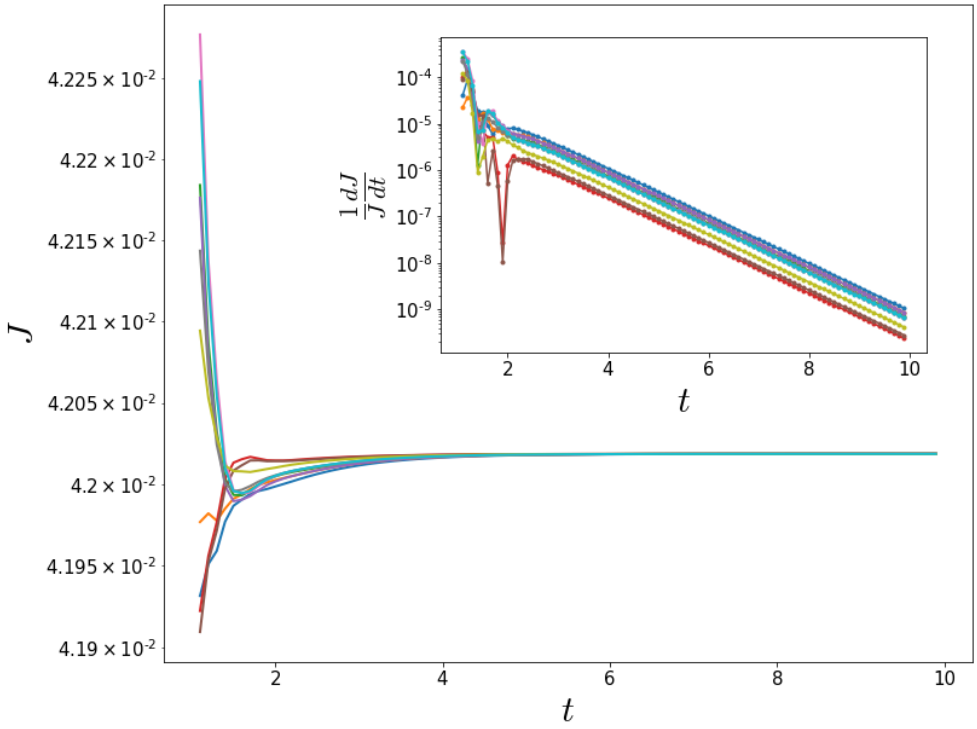

Figure B.2: Numerically exact calculations for the XXZ model with $\Delta = 0.5$ and system size of $N = 9$. Each colored line corresponds to a random product initial state.

B.2.2 Clean XXZ Model

In this section, we present the convergence of the modified NESS with bond dimension and trotter time step for non-disordered models in our study. In our simulations, we consider that the convergence with the time is achieved if the relative error of spin current in one characteristic time $[J(t-1) - J(t)]/J(t)$ is below 10^{-4}.

First, the convergence with Trotter step size is represented in Fig. B.3 (a). In the main text, we used $\delta t = 0.1$ for all numerical calculations. We find that $\delta t = 0.1$ results show only 2% difference compared to the smallest $\delta t = 0.025$ cases. It suggests that our choice of the Trotter time step correctly describes the given model's physics, given that a smaller Trotter step normally helps the simulation have a better approximation.

Next, the convergence with the bond dimension is shown in Fig. B.3 (b) According to our general observation, achieving the NESS convergence becomes more difficult as the anisotropy parameter Δ gets stronger. It is notable that the hardest case among our simulation parameter ($N = 256$, $\Delta = 2.0$ and $\ell_* = 5$) with $\chi = 64$ case also converges very well, demonstrating that the relative error is less than 2% in comparison with the next largest bond dimension $\chi = 48$. The result implies that DAOE-assisted NESS converges with a relatively smaller bond dimension for the clean XXZ model.

B.2.3 Disordered XY Model

In the main text, we encountered apparent subdiffusive transport in the disordered XY model. In this slow dynamical regime, accessing an accurate NESS with a reliable convergence is difficult to achieve due to both expensive space and time computational complexities. Here, we

describe the convergence of the modified NESS with respect to several simulation parameters.

Since a finite time evolution always approximates NESS in a practical calculation, accomplishing a tolerable error is the most important aspect of the simulation. Fig. B.1 (a) illustrates time evolution of scaled spin current of the modified NESS up to $t = 1000$. Similar to the non-disordered case, we set the same convergence criteria we employed for the clean XXZ model.

A similar trend is observed for the DAOE-NESS combined approach in accordance with the theory of DAOE, which states that artificial dissipation significantly reduces the required bond dimension to express a quantum state in question. One can also confirm that bond dimension $\chi = 64$ shows good convergence for the simulation with the longest cut-off length $\ell_* = 5$. Meanwhile, the shortest cut-off length $\ell_* = 1$ simulation only requires $\chi = 16$ to find a NESS convergence to a similar level (data not shown). Because the entanglement growth is more suppressed when applying DAOE with a shorter cut-off length, the quantum state can be efficiently represented with a smaller bond dimension. Meanwhile, a larger disorder and a longer cut-off length results in a shorter convergence time (Fig. 3.11) for fixed system size, as expected. Roughly, the convergence time exponentially growing function of both ℓ_* and h. This trend severely limits the accessible parameter regime of the study. However, we could not find any clear relation between bond dimension and convergence time.

Typically, site-to-site fluctuation of local spin current remains even though the average value converges. This site-to-site fluctuation also tends to slightly decrease by employing a larger bond dimension, however, it hugely depends on the disorder strength. This is measured by the scaled standard deviation σ/J (Fig. B.1 (b)). The number of samples M for each case is therefore determined by the statistical uncertainty $\sigma/J\sqrt{M}$, which is around 0.1 for the most difficult cases. For example, the $h = 3.0$ case has $\sigma/J \sim 0.6$, and it follows that the required M

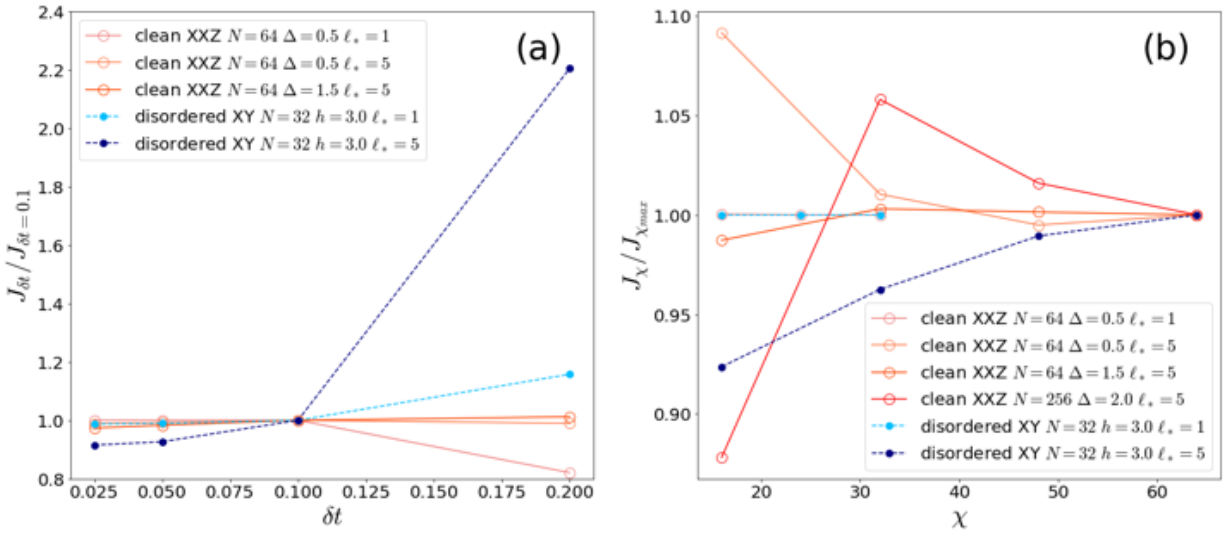

Figure B.3: (a) NESS convergence with Trotter time step. All data is extracted with bond dimension $\chi = 32$ for $\ell_* = 1$ and $\chi = 64$ for $\ell_* = 5$. (b) NESS convergence with bond dimension. Here, the Trotter step size is fixed at $\delta t = 0.1$.

is around 25 to meet our criteria.

It is clear that a smaller Trotter step δt results in a more accurate NESS approximation, but choosing an appropriate δt is necessary to reduce the total time complexity. In the main text, we used the second-order Suzuki-Trotter decomposition in the TEBD algorithm with $\delta t = 0.1$. The Hamiltonian contains at most 2-site operators, this even-odd type decomposed time evolution is expected not to change the physical properties of the model. The characteristic NESS convergences with the trotter step are shown in Fig. B.3 (a), for both shortest ($\ell_* = 1$) and longest ($\ell_* = 5$) operator cut-off lengths. The spin current seems to converge as we use smaller δt. The relative difference for the smallest $\delta t = 0.025$ case is about 1% and 8% for $\ell_* = 1$ and $\ell_* = 5$ respectively, compared to our usual value $\delta t = 0.1$ for the main text.

B.2.4 Weakly Dissipated NESS

In the main text, we frequently treat transport of the modified NESS under strong operator weight dissipations where subsequent dynamics is mostly governed by short operators. Analogous to the original study in Ref. [187] and diffusive case in the main text, it is deserving to explore the behavior of the modified NESS near the unitary limit. In particular, a reliable NESS calculation for a system with strong disorder and slow dynamics is notoriously hard. To investigate the potential improvement of NESS quality in subdiffusive transport physics, we choose the XY model with the Fibonacci disorder, which is realized by the deterministic disorder. In this model, the Fibonacci sequence gives the disorder h or $-h$ for each site (See [52, 314] for a detailed construction). Previous studies suggest that the model has varying anomalous transport; the scaling exponent χ monotonically increases as the disorder strength gets stronger. Here, we apply time-dependent $\gamma \sim 1/t$, trying to recover the unitary dynamics at a late time, otherwise, the setup is the same as in the main text.

Fig. B.4 shows the time-evolving $\langle J(t)\rangle/2\mu$ for three dissipation strengths for the model with $h = 2.0$ whose (non-dissipative) transport is subdiffusive ($\chi \sim 1.17$). The expectation value is sensitive to the (stronger) early time dissipation before overcoming the entanglement barrier and slowly relaxing to the unitary dynamics. It appears that there remains the accumulative effect of the early time despite the rapid decrease in dissipation. Meanwhile, stronger dissipation results in smaller scaled standard deviation of the expectation value, $\sigma/\langle J\rangle$ (inset of Fig. B.4). The result shows a clear improvement of convergence time in the strongest γ case as well. We have no clear relation of the tradeoff between the accuracy and the quality of convergence, however, the result offers a potential usage of this approach to approximate the unitary dynamics for such systems.

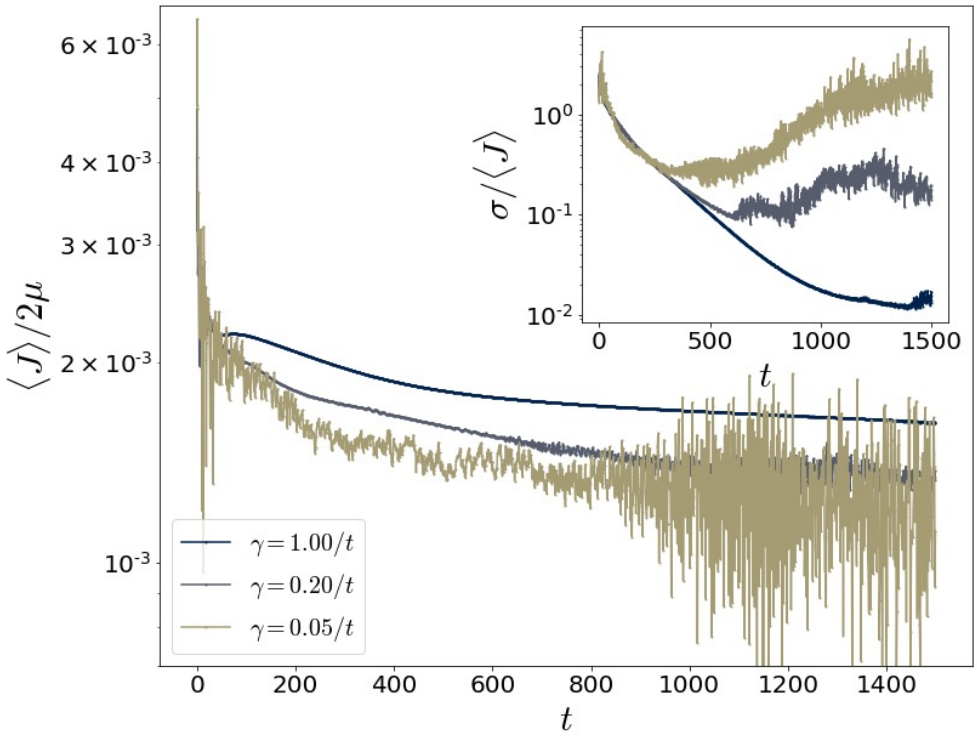

Figure B.4: Convergence of the scaled average spin current $\langle J \rangle / 2\mu$ obtained from the modified NESS with weak dissipations for the XY model with the Fibonacci disorder ($N = 89$ and $h = 2.0$). The inset shows corresponding scaled standard deviation $\sigma / \langle J \rangle$ of $\langle J \rangle$.

B.3 Operator Weight Distribution for Small Systems

The transport coefficients, D, and χ, experience both non-monotonic and monotonic behavior in ℓ_* depending on the system in question. Among many possible factors, the operator weight distribution of the NESS can be directly related to those phenomena. For a small system size ($N = 12$), it is possible to obtain the exact operator weight distribution of the NESS for several different parameters presented in the main text (Fig. B.5). In general, the trivial operator has almost of weight and the distribution exponentially decreases in length ℓ. However, non-monotonic distribution is observed for the ergodic systems, especially for short operators, which might be responsible for similar behaviors in the transport coefficients. On the other hand, the distribution has an exponential decrease trend for the localized models. The decreasing trend strengthens as the disorder increases, suggesting that the reinforced subdiffusive transport in a short length scale is connected to the operator weight distribution and the localization length. This investigation supports our rough analysis of the resultant non-monotonic or monotonic behavior of the transport coefficients in ℓ_* of the (modified) NESS.

B.4 Energy diffusion coefficients for the XXZ model at $\Delta = 1.5$

In Section 3.5.2.1 we discussed how DAOE affects transport in the integrable anisotropic XXZ model at large artificial dissipation $\gamma = 10$. The XXZ model is diffusive for $\Delta > 1$; in this appendix we extract diffusion coefficients for the model at $\Delta = 1.5$.

Fig. B.6 shows the diffusion coefficient as a function of γ for $\ell_* = 2, 3$. Curiously, the diffusion coefficient is closer to the true value for $\ell_* = 2$ than for $\ell_* = 3$. We attribute this to the

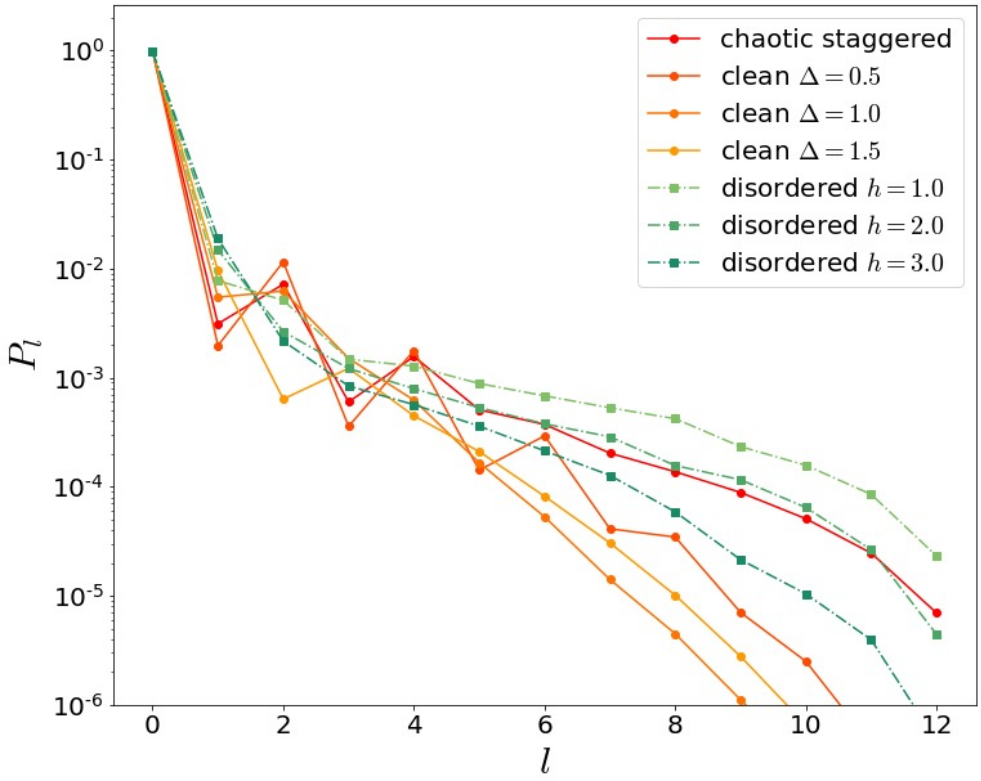

Figure B.5: Operator weight distribution for several parameters having different transport types as a function of length ℓ.

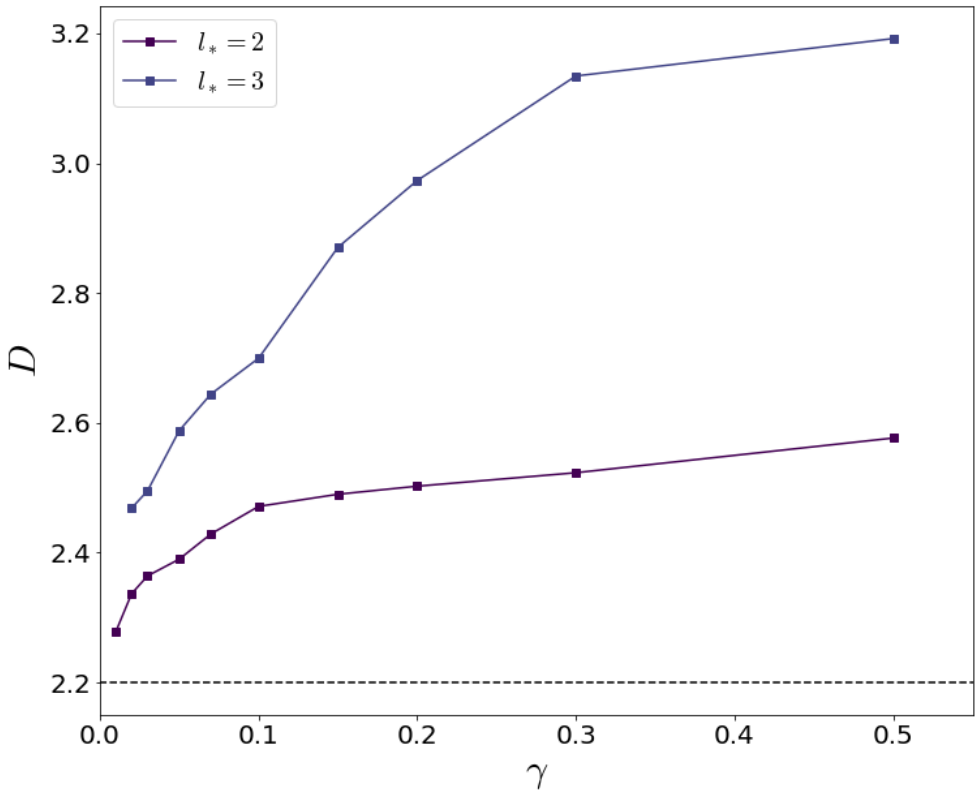

Figure B.6: Plot of diffusion constant D of the anisotropic XXZ model with $\Delta = 1.5$ from various dissipation strengths γ. D is extracted by using the best $1/L$ fitting curve, which is obtained from the system size $60 \leq L \leq 100$. Bond dimension is 64 and the convergence in the bond dimension is about 2%. Other simulation parameters are similar to the main text. The black dashed line is the diffusion constant calculated by similar NESS setting without dissipation in [34].

interplay between two effects. One the one hand, DAOE at any ℓ_* breaks the subtle integrability effects that give the true diffusion coefficient $D \approx 2.2$. Evidently, doing so increases the diffusion coefficient. On the other hand, the DAOE superoperator at $\ell_* = 2$ specifically decreases the energy current, because the energy current operator has nontrivial components consisting of three Pauli matrices, giving a correction to the general DAOE-caused increase of the diffusion coefficient. We expect that a better understanding would start with the effect of DAOE on the $\Delta = \infty$ kinetic picture of [206, 315] (cf [155]).

Appendix C: Supplementary Material for Chapter 4

C.1 Details of Tensor Network Simulations

Our main goal in this text is to investigate how the energy transport of the $\mathbb{Z}_3$ CCM is influenced by temperature variations. In this section, we take a closer look at the details of our tensor network calculations. For our finite temperature tensor network approach, we choose the vectorization approach to depict the density matrix [80] over the purification approach [78]. While this approach doesn't necessarily preserve positivity, it generally offers a more effective way to represent an open quantum system setup compared to alternatives. Using this formalism, we introduce the finite temperature bath into the superoperator L, as outlined in Eq. 4.8.

In the context of the boundary driving setup and using the specified superoperators, we attain a non-equilibrium steady state by employing the TEBD algorithm on the vectorized density matrix [76, 79, 142]. The time evolution superoperator is represented as $U = e^{\mathcal{L}\delta t}$ and is discretized using the Suzuki-Trotter decomposition. The $2k-$th order Suzuki-Trotter decomposition of the time evolution operator $U^{(2k)}$ is defined by the following recurrence relation [316],

$$U^{(2)}(\delta t) = e^{\frac{\delta t}{2}\mathcal{L}_{N-1}} \cdots e^{\frac{\delta t}{2}\mathcal{L}_1}, \tag{C.1}$$

$$U^{(2k)}(\delta t) = U^{(2k-2)}(u_k \delta t)^2 U^{(2k-2)}((1-4u_k)\delta t) U^{(2k-2)}(u_k \delta t)^2, \tag{C.2}$$

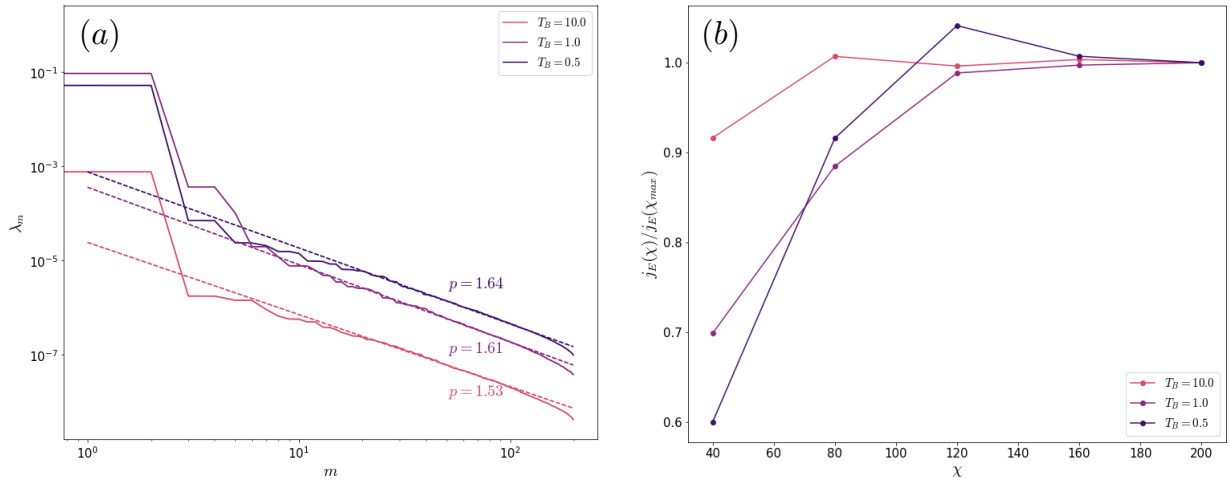

Figure C.1: Typical convergence of the NESS for $L = 32$, $\chi = 200$ at the critical point ($\chi = 200$, $f = 0.463, \theta = \pi/8$) at various bath temperatures. (a) Schmidt spectrum at the center of the chain. The best power-law fittings are presented with dashed lines. (b) Convergence of the scaled energy current as a function of bond dimension χ.

where $u_k = 1/(4-4^{1/(2k-1)})$. In our simulations, we opt for a second-order approximation and set the time step to $\delta t = 0.05$. When applying the discretized time evolution operator, we introduce a cumulative error of order $\mathcal{O}(\delta t^{2k+1})$ into our final state and, consequently, its expectation values. Despite this, we observe that the error remains below 1% within the parameters of our simulation.

An additional significant source of simulation error emerges from truncating the operator Hilbert space dimension of the density matrix. The extent of this truncation error is intricately linked to the operator space entanglement entropy of the NESS. To manage the computational complexity of the simulation, we utilize the standard Schmidt value truncation. In this approach, the Schmidt decomposition of the density matrix into two subsystems, denoted as A and B, is expressed as [88]:

$$\rho = \sum_m \sqrt{\lambda_m} \rho_m^A \otimes \rho_m^B. \tag{C.3}$$

Subsequently, the truncation error is evaluated as the sum of truncated Schmidt values, expressed as $\sum_{m>\chi} \lambda_m$. The canonical representation of MPS conveniently grants direct access to the spec-

trum of Schmidt values [86]. In our simulations, we notice a characteristic asymptotic power-law decay [177], denoted as $\lambda_m \sim m^{-p}$ (refer to Fig. C.1 (a)), which holds true for all simulation parameters. Hence, we believe that the non-equilibrium state will exhibit an efficient representation in terms of tensor networks even at low temperatures and extended local Hilbert space.

The combination of the cumulative Suzuki-Trotter expansion error and the truncated Hilbert space error introduces an imperfect representation of ρ_{NESS} as a tensor network. This inherent instability manifests as minor fluctuations in the expectation values, persisting even at later stages of the simulation. To estimate the most probable physical outcome, we take an average of our expectation values over approximately 10^3 Trotter steps, considering the most challenging simulation in our study.

Typically, opting for the initial state as an infinite temperature state, the dynamics encounters an upsurging entanglement entropy in the early stages, reaching saturation in later times. To ensure a good approximation at each time domain as the density matrix evolves, we employ varying bond dimensions. Initially, we start with a large bond dimension, $\chi = 200$, during the early stages, and then reduce χ to 81 for intermediate times where the entanglement entropy begins to saturate while the expectation values continue evolving. Subsequently, at late times, we increase the bond dimension back to $\chi = 200$ to fine-tune our solution. We consistently verify the convergence of NESS observables with the bond dimension and find $\chi = 200$ to be sufficient within our range of study. The convergence of the NESS expectation value, as illustrated in Fig. C.1, confirms that the NESS energy current improves with a larger χ, aligning with the power-law decay of the Schmidt value spectrum closely tied to the estimated error order [177].

Similar to chaotic spin-$1/2$ systems, our system converges to a unique NESS as a consequence of its dynamics [251]. When initializing the system with various states $\rho(0)$, we verify

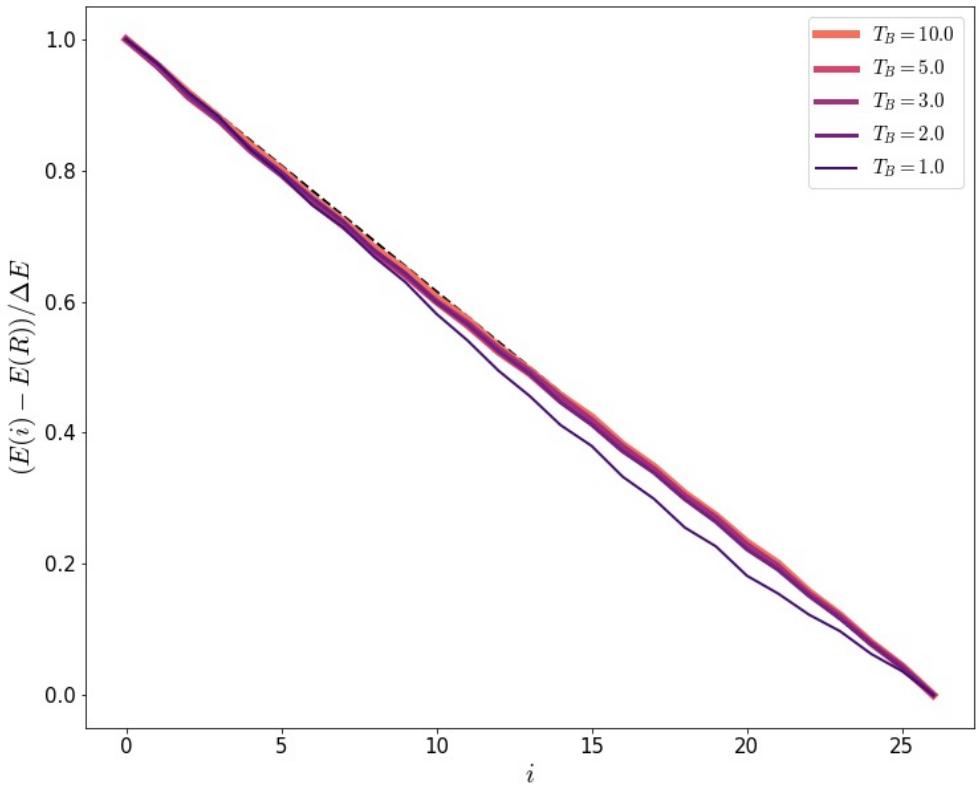

Figure C.2: The scaled energy profile of the NESS for $L = 48, \chi = 200$ at the critical point parameters $(f, \theta) = (0.463, \pi/8)$ and various bath temperatures for the center region of the system by dropping 10 sites at the each end. The black dashed line represents the exact linear profile.

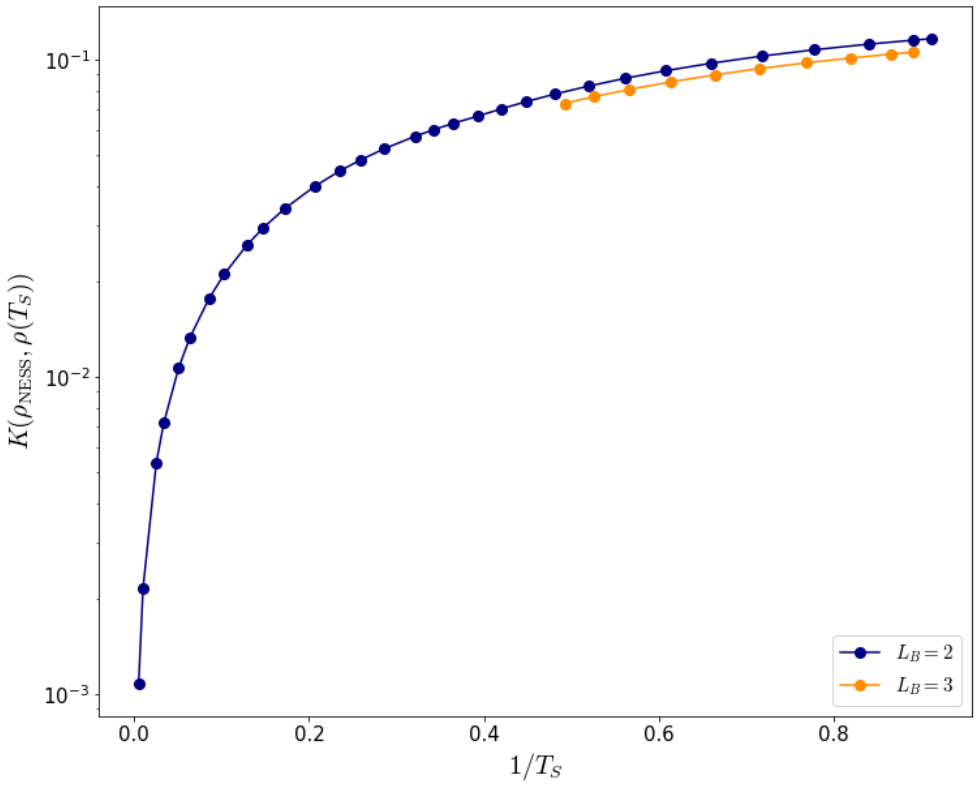

Figure C.3: The trace distance $K(\rho_{\mathrm{NESS}}, \rho(T_B))$ between the NESS for $L = 48, \chi = 200$ and the thermal state for the parameters $(f, \theta) = (0.463, \pi/8)$ as a function of the inverse of the effective temperature.

that the resulting state converges to the same NESS, with differences being negligible and attributed to cumulative errors and late-time fluctuations. The uniqueness of this NESS enables us to employ a temperature annealing strategy for lower temperature simulations, in which the relaxation times to reach the NESS are significantly extended. The primary computational workload arises from the gradual evolution during the mid-later stages. However, the early time evolution from an infinite temperature state can be bypassed by initiating the process with a slightly higher temperature NESS to attain the subsequent lower temperature NESS.

Obtaining expectation values for local operators with respect to the resulting NESS directly hinges upon the convergence quality of the NESS under the chosen simulation parameters. Given

our focus on estimating transport coefficients, one of the most crucial expectation values is the gradient of energy ΔE, which is in the denominator of Fourier's law and typically maintains a small magnitude. Even minor fluctuations in local energy can introduce significant errors in the transport coefficient estimations, limiting our simulation capacity. We carefully choose the central region of the system where the energy gradient closely approximates linearity, as depicted in Fig. Fig. C.2, to effectively analyze the bulk transport properties. Thus, we confirm that the analysis presented in the main text remains valid within the scope of our simulations.

In addition to the expectation value of local operators, the trace distance serves as a critical metric for estimating the closeness of the resulting NESS to the local thermal state. As illustrated in Fig. Fig. C.3, we observe characteristic behavior of the trace distance in the low-temperature simulation discussed in the main text. Notably, the effective local temperature estimated from the trace distance exhibits no significant variance with increasing system size under identical simulation parameters. Consequently, we can leverage Fourier's law phenomenologically to estimate temperature-dependent transport coefficients. However, the trace distance also highlights the challenge inherent in performing accurate low-temperature transport simulations within an open-quantum system framework. While we assert in the main text that a larger external bath marginally improves this situation, the exponential growth in the dimension of the bath operator with its size amplifies computational costs associated with the MPO-MPS multiplication. Furthermore, the relaxation time to reach NESS worsens significantly with larger bath operators, possibly caused by the spectral gap structure of the bath operators. These limitations compel us to restrict the use of bath operators larger than 3 sites for the most stable and reliable method to estimate low-temperature transport properties. Unfortunately, truncating the bond dimension for the thermal bath did not yield a more efficient expression; however, we remain optimistic that

advancements in bath engineering could enhance low-temperature simulations.

C.2 Multi-site Lindblad Operators

Our goal is to construct a super-operator $\mathcal{L}_B$ from a set of Lindblad operators $\{L_{jk}\}$ such that it drives the $M-$site bath to a Gibbs state at temperature T_B and chemical potential μ_B, i.e., $\mathcal{L}_B(\rho_B) = 0$ where

$$\rho_B = \frac{e^{-(H_B - \mu_B N_B)/T_B}}{\mathrm{Tr}\left(e^{-(H_B - \mu_B N_B)/T_B}\right)}, \tag{C.4}$$

and N_B is the total spin or particle number operator of the bath. We therefore require that ρ_B is a unique eigenvector of $\mathcal{L}_B$ with eigenvalue 0. However, this condition does not fully fix the jump operators, as it only ensures that the steady state is correct. One can additionally require that all the other modes decay at the same rate [33], which results in the fastest convergence to ρ_B. Alternatively, one could impose the detailed-balance condition between the energy levels of H_B, which may lead to better thermalization in certain regimes [35]. For our models, we find that both approaches work equally well even at low temperatures.

In the case of free fermions, the number of Lindblad operators required to thermalize the bath scales linearly with its size, while for a generic spin system, this number scales exponentially with M. This may seem problematic at first, since it would severely restrict the size of the bath that can be implemented in practice. However, as we show in the main text, even a relatively small bath can result in good thermalization under the right conditions. The real bottleneck is in designing a compact tensor network representation of the Liouvillian $\mathcal{L}_\mathcal{B}$, which can be efficiently applied to the bath without generating too much entanglement during time evolution.

A potential avenue of research would be to leverage the Product Spectrum Ansatz [310, 311] to design dissipators that only approximately thermalize larger baths.

For interacting spin systems, we extend the two-site Lindblad operators construction in Refs. [31, 33, 34, 47, 317] to systems of arbitrary size. Consider the general case where each of the M spins has a local Hilbert space dimension d. We begin by diagonalizing the density matrix $\rho_B = V^\dagger W V$, where $W = \mathrm{diag}(W_0, W_1, \ldots, W_{d^M-1})$ and V is unitary. Define a set of d^{2M} operators $\tilde{L}_{jk} \in \mathbb{R}^{d^M \times d^M}$

$$\tilde{L}_{jk} = \sqrt{\gamma W_j} E_{jk}, \quad 0 \leq j, k < d^M, \tag{C.5}$$

where E_{ab} is the matrix unit with a 1 in row a and column b as its only non-zero entry. Here γ quantifies the overall strength of the bath damping. It is easy to verify that

$$\tilde{L}_{jk} W \tilde{L}_{jk}^\dagger = \gamma W_j W_k E_{jj}, \tag{C.6}$$

$$\tilde{L}_{jk}^\dagger \tilde{L}_{jk} W = W \tilde{L}_{jk}^\dagger \tilde{L}_{jk} = \gamma W_j W_k E_{kk}. \tag{C.7}$$

Therefore we have

$$\begin{aligned} \tilde{\mathcal{L}}_B(W) &= \sum_{j,k=0}^{d^M-1} \left(\tilde{L}_{jk} W \tilde{L}_{jk}^\dagger - \frac{1}{2} \tilde{L}_{jk}^\dagger \tilde{L}_{jk} W - \frac{1}{2} W \tilde{L}_{jk}^\dagger \tilde{L}_{jk} \right) \\ &= \gamma \sum_{j,k=0}^{d^M-1} W_j W_k \left(E_{jj} - E_{kk} \right) = 0, \end{aligned} \tag{C.8}$$

and we can multiply this expression by $V^\dagger$ and V on the left and right sides, and use the identity $VV^\dagger = I$ to deduce that

$$\sum_{j,k=0}^{d^M-1} \left(L_{jk}\rho_B L_{jk}^\dagger - \frac{1}{2} L_{jk}^\dagger L_{jk}\rho_B - \frac{1}{2}\rho_B L_{jk}^\dagger L_{jk} \right) = 0, \tag{C.9}$$

with $L_{jk} = V^\dagger \tilde{L}_{jk} V$. Hence we can use these new Lindblad operators L_{jk} to construct a superoperator satisfying $\mathcal{L}_B(\rho_B) = 0$. Moreover, since V is unitary, the eigenvalues of $\mathcal{L}_B$ will be the same as those of $\tilde{\mathcal{L}}_B$. We can compute the latter using the vectorized representation of the Liouvillian [80, 303, 318]

$$\tilde{\mathcal{L}}_B = \sum_{j,k=0}^{d^M-1} \left(\tilde{L}_{jk}^* \otimes \tilde{L}_{jk} - \frac{1}{2} I \otimes \tilde{L}_{jk}^\dagger \tilde{L}_{jk} - \frac{1}{2} \tilde{L}_{jk}^T \tilde{L}_{jk}^* \otimes I \right), \tag{C.10}$$

where

$$\tilde{L}_{jk}^* \otimes \tilde{L}_{jk} = \gamma W_j E_{j(d^M+1),k(d^M+1)}, \tag{C.11}$$

$$I \otimes \tilde{L}_{jk}^\dagger \tilde{L}_{jk} = \gamma W_j \sum_{i=0}^{d^M-1} E_{k+i\cdot d^M, k+i\cdot d^M}, \tag{C.12}$$

$$\tilde{L}_{jk}^T \tilde{L}_{jk}^* \otimes I = \gamma W_j \sum_{i=0}^{d^M-1} E_{i+k\cdot d^M, i+k\cdot d^M}, \tag{C.13}$$

and I denotes the $d^M \times d^M$ identity matrix. It is straightforward to check that $\tilde{\mathcal{L}}_B$ has exactly one zero eigenvalue and the remaining eigenvalues are equal to $-\gamma$, since $\sum_{j=0}^{d^M-1} W_j = \mathrm{Tr}(\rho_B) = 1$. Hence our construction leads to the fastest relaxation to the target density matrix [33].

A different set of dissipators, satisfying detailed-balance relations, has also been pro-

posed [35]. Using our notation above, these operators take the form

$$\tilde{L}_{jk} = \sqrt{\frac{\gamma W_j}{W_j + W_k}} E_{jk}, \quad 0 \leq j \neq k < d^M. \tag{C.14}$$

We can again verify that they drive the bath to its correct thermal state

$$\tilde{\mathcal{L}}_B(W) = \gamma \sum_{j,k=0}^{d^M-1} \frac{W_j W_k}{W_j + W_k} (E_{jj} - E_{kk}) = 0, \tag{C.15}$$

since

$$\tilde{L}_{jk} W \tilde{L}_{jk}^\dagger = \gamma \frac{W_j W_k}{W_j + W_k} E_{jj}, \tag{C.16}$$

$$\tilde{L}_{jk}^\dagger \tilde{L}_{jk} W = W \tilde{L}_{jk}^\dagger \tilde{L}_{jk} = \gamma \frac{W_j W_k}{W_j + W_k} E_{kk}. \tag{C.17}$$

The final jump operators are given by $L_{jk} = V^\dagger \tilde{L}_{jk} V$.

C.3 Thermalization Results for Weakly Damping Thermal Baths

The results for the chiral clock model are displayed in Fig. C.4. We employ the annealing procedure and set the minimal bond dimension to $\chi = 81$. The convergence is noticeably slower, so we evolve the initial state up to $t = 2 \cdot 10^4$ for the smallest values of g and γ. For intermediate bath temperatures $T_B = 1$, the system's temperature T_S seems to converge the target at the smallest $g = \gamma = 0.1$. However, in the low temperature $T_B = 0.1$ case, the final bulk temperature does not improve past $T_S \approx 0.5$, even though the system is gapless. Nevertheless, there are

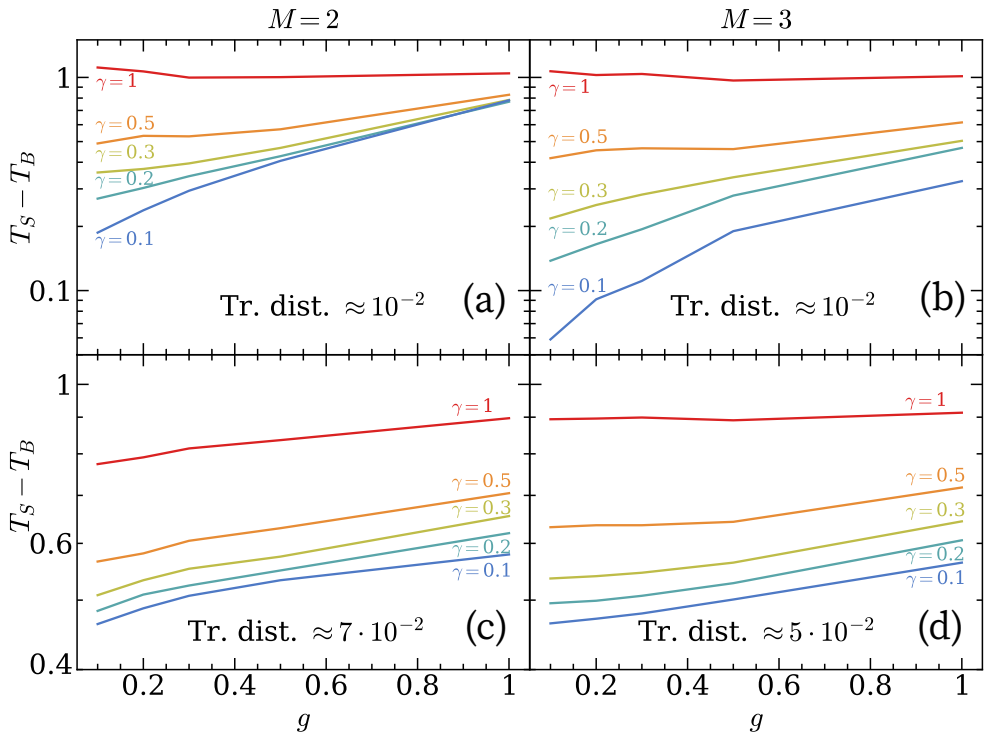

Figure C.4: Thermalization results for the chiral clock model coupled to a boundary bath at temperatures (a-b) $T_B = 1$ and (c-d) $T_B = 0.1$. For intermediate bath temperatures (top), the system approaches a temperature close to T_B in the limit of weak system-bath coupling g and damping γ. At low driving temperatures (bottom), the system's final temperature is significantly above T_B. The trace distances indicated in each panel are for the steady states with the lowest temperature.

slight improvements in the trace distance when expanding the bath from $M = 2$ sites to $M = 3$ sites. It is quite possible that cooling a gapless model may require much larger baths and longer convergence times, beyond what is accessible numerically with the current setup. Another explanation is that there may be an emergent energy scale that prohibits the Lindblad operators from cooling the system below that scale.

Bibliography

[1] Yongchan Yoo, Junhyun Lee, and Brian Swingle. Nonequilibrium steady state phases of the interacting aubry-andré-harper model. *Phys. Rev. B*, 102:195142, Nov 2020.

[2] Yongchan Yoo, Christopher David White, and Brian Swingle. Open-system spin transport and operator weight dissipation in spin chains. *Phys. Rev. B*, 107:115118, Mar 2023.

[3] Yongchan Yoo and Brian Swingle. Temperature dependence of energy transport in the $\mathbb{z}_3$ chiral clock model. *Phys. Rev. B*, 109:235104, Jun 2024.

[4] Cristian Zanoci, Yongchan Yoo, and Brian Swingle. Thermalization at low temperatures via weakly damped multisite baths. *Phys. Rev. B*, 108:035156, Jul 2023.

[5] Fernando G. S. L. Brandão and Aram W. Harrow. Product-State Approximations to Quantum States. *Communications in Mathematical Physics*, 342(1):47–80, February 2016.

[6] Anatoli Polkovnikov, Krishnendu Sengupta, Alessandro Silva, and Mukund Vengalattore. Colloquium: Nonequilibrium dynamics of closed interacting quantum systems. *Rev. Mod. Phys.*, 83:863–883, Aug 2011.

[7] J. Eisert, M. Friesdorf, and C. Gogolin. Quantum many-body systems out of equilibrium. *Nature Physics*, 11(2):124–130, feb 2015.

[8] Christian Gogolin and Jens Eisert. Equilibration, thermalisation, and the emergence of statistical mechanics in closed quantum systems. *Reports on Progress in Physics*, 79(5):056001, apr 2016.

[9] Pasquale Calabrese, Fabian H L Essler, and Giuseppe Mussardo. Introduction to 'quantum integrability in out of equilibrium systems'. *Journal of Statistical Mechanics: Theory and Experiment*, 2016(6):064001, jun 2016.

[10] Rahul Nandkishore and David A. Huse. Many-body localization and thermalization in quantum statistical mechanics. *Annual Review of Condensed Matter Physics*, 6(1):15–38, Mar 2015.

[11] Dmitry A. Abanin, Ehud Altman, Immanuel Bloch, and Maksym Serbyn. Colloquium: Many-body localization, thermalization, and entanglement. *Reviews of Modern Physics*, 91(2):021001, May 2019.

[12] Luca D'Alessio, Yariv Kafri, Anatoli Polkovnikov, and Marcos Rigol. From Quantum Chaos and Eigenstate Thermalization to Statistical Mechanics and Thermodynamics. *Advances in Physics*, 65(3):239–362, May 2016. arXiv:1509.06411 [cond-mat, physics:quant-ph].

[13] Fabian H L Essler and Maurizio Fagotti. Quench dynamics and relaxation in isolated integrable quantum spin chains. *Journal of Statistical Mechanics: Theory and Experiment*, 2016(6):064002, jun 2016.

[14] Lev Vidmar and Marcos Rigol. Generalized gibbs ensemble in integrable lattice models. *Journal of Statistical Mechanics: Theory and Experiment*, 2016(6):064007, jun 2016.

[15] Immanuel Bloch, Jean Dalibard, and Wilhelm Zwerger. Many-Body Physics with Ultracold Gases. *Reviews of Modern Physics*, 80(3):885–964, July 2008. arXiv: 0704.3011.

[16] Immanuel Bloch, Jean Dalibard, and Sylvain Nascimbène. Quantum simulations with ultracold quantum gases. *Nature Physics*, 8(4):267–276, April 2012.

[17] Christian Gross and Immanuel Bloch. Quantum simulations with ultracold atoms in optical lattices. *Science*, 357(6355):995–1001, September 2017.

[18] John Preskill. Quantum Computing in the NISQ era and beyond. *Quantum*, 2:79, August 2018.

[19] Sadao Nakajima. On Quantum Theory of Transport Phenomena: Steady Diffusion. *Prog. Theor. Phys.*, 20(6):948–959, 12 1958.

[20] Robert Zwanzig. Ensemble method in the theory of irreversibility. *J. Chem. Phys.*, 33(5):1338–1341, 1960.

[21] Heinz-Peter Breuer and Francesco Petruccione. *The Theory of Open Quantum Systems*. Oxford University Press, 01 2007.

[22] K Kraus. General state changes in quantum theory. *Annals of Physics*, 64(2):311–335, 1971.

[23] K Lendi R Alicki. *Quantum Dynamical Semigroups and Applications*, volume 717 of *Lecture Notes in Physics*. Springer Berlin Heidelberg, Berlin, Heidelberg, 2007.

[24] Vittorio Gorini. Completely positive dynamical semigroups of N-level systems. *Journal of Mathematical Physics*, 17(5):821, 1976.

[25] G. Lindblad. On the generators of quantum dynamical semigroups. *Communications in Mathematical Physics*, 48(2):119–130, June 1976.

[26] David E. Evans. Irreducible quantum dynamical semigroups. *Communications in Mathematical Physics*, 54(3):293–297, October 1977.

[27] Alberto Frigerio. Quantum dynamical semigroups and approach to equilibrium. *Letters in Mathematical Physics*, 2(2):79–87, December 1977.

[28] Herbert Spohn. An algebraic condition for the approach to equilibrium of an open N-level system. *Letters in Mathematical Physics*, 2(1):33–38, August 1977.

[29] Joaquin Marro and Ronald Dickman. *Nonequilibrium Phase Transitions in Lattice Models*. Cambridge University Press, 1 edition, May 1999.

[30] Bernard Derrida. Non-equilibrium steady states: fluctuations and large deviations of the density and of the current. *Journal of Statistical Mechanics: Theory and Experiment*, 2007(07):P07023, jul 2007.

[31] J. J. Mendoza-Arenas, S. R. Clark, and D. Jaksch. Coexistence of energy diffusion and local thermalization in nonequilibrium xxz spin chains with integrability breaking. *Phys. Rev. E*, 91:042129, Apr 2015.

[32] Marko Žnidarič. Dephasing-induced diffusive transport in the anisotropic heisenberg model. *New Journal of Physics*, 12(4):043001, Apr 2010.

[33] Tomaž Prosen and Marko Žnidarič. Matrix product simulations of non-equilibrium steady states of quantum spin chains. *Journal of Statistical Mechanics: Theory and Experiment*, 2009(02):P02035, February 2009.

[34] Marko Žnidarič. Transport in a one-dimensional isotropic heisenberg model at high temperature. *Journal of Statistical Mechanics: Theory and Experiment*, 2011(12):P12008, dec 2011.

[35] Mikel Palmero, Xiansong Xu, Chu Guo, and Dario Poletti. Thermalization with detailed-balanced two-site lindblad dissipators. *Phys. Rev. E*, 100:022111, Aug 2019.

[36] Philipp Strasberg. *Quantum Stochastic Thermodynamics: Foundations and Selected Applications*. Oxford University PressOxford, 1 edition, January 2022.

[37] Marko Znidaric, Tomaz Prosen, Giuliano Benenti, Giulio Casati, and Davide Rossini. Thermalization and ergodicity in one-dimensional many-body open quantum systems. *Phys. Rev. E*, 81:051135, May 2010.

[38] Ángel Rivas, A Douglas K Plato, Susana F Huelga, and Martin B Plenio. Markovian master equations: a critical study. *New Journal of Physics*, 12(11):113032, nov 2010.

[39] Archak Purkayastha, Abhishek Dhar, and Manas Kulkarni. Out-of-equilibrium open quantum systems: A comparison of approximate quantum master equation approaches with exact results. *Phys. Rev. A*, 93:062114, Jun 2016.

[40] Hannu Wichterich, Markus J. Henrich, Heinz-Peter Breuer, Jochen Gemmer, and Mathias Michel. Modeling heat transport through completely positive maps. *Phys. Rev. E*, 76:031115, Sep 2007.

[41] Amikam Levy and Ronnie Kosloff. The local approach to quantum transport may violate the second law of thermodynamics. *Europhysics Letters*, 107(2):20004, jul 2014.

[42] Xiansong Xu, Juzar Thingna, and Jian-Sheng Wang. Finite coupling effects in double quantum dots near equilibrium. *Phys. Rev. B*, 95:035428, Jan 2017.

[43] Devashish Tupkary, Abhishek Dhar, Manas Kulkarni, and Archak Purkayastha. Fundamental limitations in lindblad descriptions of systems weakly coupled to baths. *Phys. Rev. A*, 105:032208, Mar 2022.

[44] Devashish Tupkary, Abhishek Dhar, Manas Kulkarni, and Archak Purkayastha. Searching for lindbladians obeying local conservation laws and showing thermalization. *Phys. Rev. A*, 107:062216, Jun 2023.

[45] A. Asadian, D. Manzano, M. Tiersch, and H. J. Briegel. Heat transport through lattices of quantum harmonic oscillators in arbitrary dimensions. *Phys. Rev. E*, 87:012109, Jan 2013.

[46] Israel Reichental, Anat Klempner, Yariv Kafri, and Daniel Podolsky. Thermalization in open quantum systems. *Phys. Rev. B*, 97:134301, Apr 2018.

[47] Cristian Zanoci and Brian Swingle. Temperature-dependent energy diffusion in chaotic spin chains. *Phys. Rev. B*, 103:115148, Mar 2021.

[48] R. Steinigeweg, F. Heidrich-Meisner, J. Gemmer, K. Michielsen, and H. De Raedt. Scaling of diffusion constants in the spin-$\frac{1}{2}$ xx ladder. *Phys. Rev. B*, 90:094417, Sep 2014.

[49] Marko Znidaric. Coexistence of diffusive and ballistic transport in a simple spin ladder. *Phys. Rev. Lett.*, 110:070602, Feb 2013.

[50] Baowen Li and Jiao Wang. Anomalous heat conduction and anomalous diffusion in one-dimensional systems. *Phys. Rev. Lett.*, 91:044301, Jul 2003.

[51] Marko Ljubotina, Marko Žnidarič, and Tomaž Prosen. Spin diffusion from an inhomogeneous quench in an integrable system. *Nature Communications*, 8(1):16117, December 2017. arXiv: 1702.04210.

[52] Vipin Kerala Varma and Marko Žnidarič. Diffusive transport in a quasiperiodic fibonacci chain: Absence of many-body localization at weak interactions. *Physical Review B*, 100(8):085105, Aug 2019.

[53] Dephasing enhanced spin transport in the ergodic phase of a many-body localizable system. 529.

[54] Marko Žnidarič. Exact solution for a diffusive nonequilibrium steady state of an open quantum chain. *Journal of Statistical Mechanics: Theory and Experiment*, 2010(05):L05002, may 2010.

[55] Marko Žnidarič. Solvable quantum nonequilibrium model exhibiting a phase transition and a matrix product representation. *Phys. Rev. E*, 83:011108, Jan 2011.

[56] A. Bermudez, M. Bruderer, and M. B. Plenio. Controlling and measuring quantum transport of heat in trapped-ion crystals. *Phys. Rev. Lett.*, 111:040601, Jul 2013.

[57] William T B Malouf, John Goold, Gerardo Adesso, and Gabriel T Landi. Analysis of the conditional mutual information in ballistic and diffusive non-equilibrium steady-states. *Journal of Physics A: Mathematical and Theoretical*, 53(30):305302, jul 2020.

[58] Scott R. Taylor and Antonello Scardicchio. Subdiffusion in a one-dimensional anderson insulator with random dephasing: Finite-size scaling, griffiths effects, and possible implications for many-body localization. *Phys. Rev. B*, 103:184202, May 2021.

[59] Donny Dwiputra and Freddy P. Zen. Environment-assisted quantum transport and mobility edges. *Phys. Rev. A*, 104:022205, Aug 2021.

[60] Artur M. Lacerda, John Goold, and Gabriel T. Landi. Dephasing enhanced transport in boundary-driven quasiperiodic chains. *Phys. Rev. B*, 104:174203, Nov 2021.

[61] Tomaž Prosen. Third quantization: a general method to solve master equations for quadratic open fermi systems. *New J. Phys.*, 10(4):043026, apr 2008.

[62] Tomaž Prosen. Spectral theorem for the lindblad equation for quadratic open fermionic systems. *J. Stat. Mech. Theory Exp.*, 2010(07):P07020, jul 2010.

[63] A. J. Leggett, S. Chakravarty, A. T. Dorsey, Matthew P. A. Fisher, Anupam Garg, and W. Zwerger. Dynamics of the dissipative two-state system. *Rev. Mod. Phys.*, 59:1–85, Jan 1987.

[64] Daniel A. Lidar, Zsolt Bihary, and K.Birgitta Whaley. From completely positive maps to the quantum markovian semigroup master equation. *Chemical Physics*, 268(1):35–53, 2001.

[65] Tomaž Prosen. Exact nonequilibrium steady state of a strongly driven open xxz chain. *Phys. Rev. Lett.*, 107:137201, Sep 2011.

[66] Tomaž Prosen. Exact nonequilibrium steady state of a strongly driven open xxz chain. *Phys. Rev. Lett.*, 107:137201, Sep 2011.

[67] Mariya V. Medvedyeva, Tomaž Prosen, and Marko Znidaric. Influence of dephasing on many-body localization. *Phys. Rev. B*, 93:094205, Mar 2016.

[68] Chu Guo and Dario Poletti. Analytical solutions for a boundary-driven xy chain. *Phys. Rev. A*, 98:052126, Nov 2018.

[69] L M Sieberer, M Buchhold, and S Diehl. Keldysh field theory for driven open quantum systems. *Reports on Progress in Physics*, 79(9):096001, aug 2016.

[70] J. Eisert, M. Cramer, and M. B. Plenio. Colloquium: Area laws for the entanglement entropy. *Rev. Mod. Phys.*, 82:277–306, Feb 2010.

[71] M. B. Plenio, J. Eisert, J. Dreißig, and M. Cramer. Entropy, entanglement, and area: Analytical results for harmonic lattice systems. *Phys. Rev. Lett.*, 94:060503, Feb 2005.

[72] Dimitri Gioev and Israel Klich. Entanglement entropy of fermions in any dimension and the widom conjecture. *Phys. Rev. Lett.*, 96:100503, Mar 2006.

[73] Michael M. Wolf. Violation of the entropic area law for fermions. *Phys. Rev. Lett.*, 96:010404, Jan 2006.

[74] Raghu Mahajan, C. Daniel Freeman, Sam Mumford, Norm Tubman, and Brian Swingle. Entanglement structure of non-equilibrium steady states, 2016.

[75] Elliott H. Lieb and Derek W. Robinson. The finite group velocity of quantum spin systems. *Communications in Mathematical Physics*, 28(3):251–257, September 1972.

[76] Guifré Vidal. Efficient simulation of one-dimensional quantum many-body systems. *Physical Review Letters*, 93(4):040502, Jul 2004.

[77] A J Daley, C Kollath, U Schollwöck, and G Vidal. Time-dependent density-matrix renormalization-group using adaptive effective hilbert spaces. *Journal of Statistical Mechanics: Theory and Experiment*, 2004(04):P04005, apr 2004.

[78] F. Verstraete, J. J. García-Ripoll, and J. I. Cirac. Matrix product density operators: Simulation of finite-temperature and dissipative systems. *Phys. Rev. Lett.*, 93:207204, Nov 2004.

[79] Steven R. White and Adrian E. Feiguin. Real-time evolution using the density matrix renormalization group. *Phys. Rev. Lett.*, 93:076401, Aug 2004.

[80] Michael Zwolak and Guifré Vidal. Mixed-state dynamics in one-dimensional quantum lattice systems: a time-dependent superoperator renormalization algorithm. *Phys. Rev. Lett.*, 93(20):207205, November 2004.

[81] Gemma De las Cuevas, Norbert Schuch, David Pérez-García, and J Ignacio Cirac. Purifications of multipartite states: limitations and constructive methods. *New Journal of Physics*, 15(12):123021, dec 2013.

[82] A. Jamiolkowski. Linear transformations which preserve trace and positive semidefiniteness of operators. *Reports on Mathematical Physics*, 3(4):275–278, 1972.

[83] Man-Duen Choi. Completely positive linear maps on complex matrices. *Linear Algebra and its Applications*, 10(3):285–290, 1975.

[84] H. F. Trotter. On the product of semi-groups of operators. *Proceedings of the American Mathematical Society*, 10(4):545–551, 1959.

[85] Masuo Suzuki. Generalized Trotter's formula and systematic approximants of exponential operators and inner derivations with applications to many-body problems. *Communications in Mathematical Physics*, 51(2):183–190, June 1976.

[86] Ulrich Schollwöck. The density-matrix renormalization group in the age of matrix product states. *Annals of Physics*, 326(1):96–192, January 2011.

[87] Thomas Barthel, Ulrich Schollwöck, and Steven R. White. Spectral functions in one-dimensional quantum systems at finite temperature using the density matrix renormalization group. *Phys. Rev. B*, 79:245101, Jun 2009.

[88] Tomaž Prosen and Iztok Pizorn. Operator space entanglement entropy in a transverse ising chain. *Phys. Rev. A*, 76:032316, Sep 2007.

[89] Marko Znidaric. Relaxation times of dissipative many-body quantum systems. *Phys. Rev. E*, 92:042143, Oct 2015.

[90] Adrian E. Feiguin and Steven R. White. Finite-temperature density matrix renormalization using an enlarged hilbert space. *Phys. Rev. B*, 72:220401, Dec 2005.

[91] Thomas Barthel. Precise evaluation of thermal response functions by optimized density matrix renormalization group schemes. *New Journal of Physics*, 15(7):073010, jul 2013.

[92] C. Karrasch and J. E. Moore. Luttinger liquid physics from the infinite-system density matrix renormalization group. *Phys. Rev. B*, 86:155156, Oct 2012.

[93] C Karrasch, J H Bardarson, and J E Moore. Reducing the numerical effort of finite-temperature density matrix renormalization group calculations. *New Journal of Physics*, 15(8):083031, aug 2013.

[94] Johannes Hauschild, Eyal Leviatan, Jens H. Bardarson, Ehud Altman, Michael P. Zaletel, and Frank Pollmann. Finding purifications with minimal entanglement. *Physical Review B*, 98(23):235163, Dec 2018.

[95] C. Karrasch, J. Hauschild, S. Langer, and F. Heidrich-Meisner. Drude weight of the spin-$\frac{1}{2}$ xxz chain: Density matrix renormalization group versus exact diagonalization. *Phys. Rev. B*, 87:245128, Jun 2013.

[96] C. Karrasch, D. M. Kennes, and J. E. Moore. Transport properties of the one-dimensional Hubbard model at finite temperature. *Physical Review B*, 90(15):155104, October 2014. Publisher: American Physical Society.

[97] C. Karrasch, D. M. Kennes, and F. Heidrich-Meisner. Spin and thermal conductivity of quantum spin chains and ladders. *Phys. Rev. B*, 91:115130, Mar 2015.

[98] C Karrasch, JE Moore, and F Heidrich-Meisner. Real-time and real-space spin and energy dynamics in one-dimensional spin-1 2 systems induced by local quantum quenches at finite temperatures. *Physical Review B*, 89(7):075139, 2014.

[99] C. Karrasch, T. Prosen, and F. Heidrich-Meisner. Proposal for measuring the finite-temperature drude weight of integrable systems. *Phys. Rev. B*, 95:060406, Feb 2017.

[100] Romain Vasseur, Christoph Karrasch, and Joel E. Moore. Expansion potentials for exact far-from-equilibrium spreading of particles and energy. *Phys. Rev. Lett.*, 115:267201, Dec 2015.

[101] C Karrasch. Hubbard-to-heisenberg crossover (and efficient computation) of drude weights at low temperatures. *New Journal of Physics*, 19(3):033027, mar 2017.

[102] Jesko Sirker and Andreas Klümper. Real-time dynamics at finite temperature by the density-matrix renormalization group: A path-integral approach. *Phys. Rev. B*, 71:241101, Jun 2005.

[103] Steven R. White. Minimally entangled typical quantum states at finite temperature. *Phys. Rev. Lett.*, 102:190601, May 2009.

[104] Chu Guo and Dario Poletti. Matrix product states with adaptive global symmetries. *Phys. Rev. B*, 100:134304, Oct 2019.

[105] E. M. Stoudenmire and Steven R. White. Real-space parallel density matrix renormalization group. *Phys. Rev. B*, 87:155137, Apr 2013.

[106] Paul Secular, Nikita Gourianov, Michael Lubasch, Sergey Dolgov, Stephen R. Clark, and Dieter Jaksch. Parallel time-dependent variational principle algorithm for matrix product states. *Phys. Rev. B*, 101:235123, Jun 2020.

[107] Marek M. Rams and Michael Zwolak. Breaking the entanglement barrier: Tensor network simulation of quantum transport. *Phys. Rev. Lett.*, 124:137701, Mar 2020.

[108] Gabriela Wójtowicz, Justin E. Elenewski, Marek M. Rams, and Michael Zwolak. Open-system tensor networks and kramers' crossover for quantum transport. *Phys. Rev. A*, 101:050301, May 2020.

[109] Marlon Brenes, Juan José Mendoza-Arenas, Archak Purkayastha, Mark T. Mitchison, Stephen R. Clark, and John Goold. Tensor-network method to simulate strongly interacting quantum thermal machines. *Phys. Rev. X*, 10:031040, Aug 2020.

[110] D.M. Basko, I.L. Aleiner, and B.L. Altshuler. Metal–insulator transition in a weakly interacting many-electron system with localized single-particle states. *Annals of Physics*, 321(5):1126–1205, May 2006.

[111] Marko Znidaric, Tomaz Prosen, and Peter Prelovsek. Many-body localization in the heisenberg xxz magnet in a random field. *Physical Review B*, 77(6):064426, Feb 2008.

[112] Arijeet Pal and David A. Huse. Many-body localization phase transition. *Physical Review B*, 82(17):174411, Nov 2010.

[113] Maksym Serbyn, Z. Papić, and Dmitry A. Abanin. Criterion for Many-Body Localization-Delocalization Phase Transition. *Physical Review X*, 5(4):041047, December 2015.

[114] Andrew C. Potter, Romain Vasseur, and Siddharth A. Parameswaran. Universal Properties of Many-Body Delocalization Transitions. *Physical Review X*, 5(3):031033, September 2015.

[115] John Z. Imbrie. On Many-Body Localization for Quantum Spin Chains. *Journal of Statistical Physics*, 163(5):998–1048, June 2016.

[116] Katharine Hyatt, James R. Garrison, Andrew C. Potter, and Bela Bauer. Many-body localization in the presence of a small bath. *Physical Review B*, 95(3):035132, January 2017.

[117] Pranjal Bordia, Henrik Lüschen, Ulrich Schneider, Michael Knap, and Immanuel Bloch. Periodically driving a many-body localized quantum system. *Nature Physics*, 13(5):460–464, Jan 2017.

[118] Vedika Khemani, D. N. Sheng, and David A. Huse. Two Universality Classes for the Many-Body Localization Transition. *Physical Review Letters*, 119(7):075702, August 2017.

[119] S A Parameswaran and Romain Vasseur. Many-body localization, symmetry and topology. *Reports on Progress in Physics*, 81(8):082501, Jul 2018.

[120] Fabien Alet and Nicolas Laflorencie. Many-body localization: An introduction and selected topics. *Comptes Rendus Physique*, 19(6):498–525, Sep 2018.

[121] Adam Nahum, Jonathan Ruhman, and David A. Huse. Dynamics of entanglement and transport in one-dimensional systems with quenched randomness. *Physical Review B*, 98(3):035118, Jul 2018.

[122] Giacomo Roati, Chiara D'Errico, Leonardo Fallani, Marco Fattori, Chiara Fort, Matteo Zaccanti, Giovanni Modugno, Michele Modugno, and Massimo Inguscio. Anderson localization of a non-interacting bose–einstein condensate. *Nature*, 453(7197):895–898, Jun 2008.

[123] Y. Lahini, R. Pugatch, F. Pozzi, M. Sorel, R. Morandotti, N. Davidson, and Y. Silberberg. Observation of a localization transition in quasiperiodic photonic lattices. *Physical Review Letters*, 103(1):013901, Jun 2009.

[124] Michael Schreiber, Sean S. Hodgman, Pranjal Bordia, Henrik P. Lüschen, Mark H. Fischer, Ronen Vosk, Ehud Altman, Ulrich Schneider, and Immanuel Bloch. Observation of many-body localization of interacting fermions in a quasirandom optical lattice. *Science*, 349(6250):842–845, 2015.

[125] Henrik P. Lüschen, Pranjal Bordia, Sean S. Hodgman, Michael Schreiber, Saubhik Sarkar, Andrew J. Daley, Mark H. Fischer, Ehud Altman, Immanuel Bloch, and Ulrich Schneider. Signatures of many-body localization in a controlled open quantum system. *Physical Review X*, 7(1):011034, Mar 2017.

[126] Henrik P. Lüschen, Pranjal Bordia, Sebastian Scherg, Fabien Alet, Ehud Altman, Ulrich Schneider, and Immanuel Bloch. Observation of slow dynamics near the many-body localization transition in one-dimensional quasiperiodic systems. *Physical Review Letters*, 119(26):260401, Dec 2017.

[127] Henrik P. Lüschen, Sebastian Scherg, Thomas Kohlert, Michael Schreiber, Pranjal Bordia, Xiao Li, S. Das Sarma, and Immanuel Bloch. Single-particle mobility edge in a one-dimensional quasiperiodic optical lattice. *Physical Review Letters*, 120(16):160404, Apr 2018.

[128] Thomas Kohlert, Sebastian Scherg, Xiao Li, Henrik P. Luschen, Sankar Das Sarma, Immanuel Bloch, and Monika Aidelsburger. Observation of many-body localization in a one-dimensional system with a single-particle mobility edge. *Physical Review Letters*, 122(17):170403, May 2019.

[129] Shankar Iyer, Vadim Oganesyan, Gil Refael, and David A. Huse. Many-body localization in a quasiperiodic system. *Physical Review B*, 87(13):134202, Apr 2013.

[130] Mac Lee, Thomas R. Look, S. P. Lim, and D. N. Sheng. Many-body localization in spin chain systems with quasiperiodic fields. *Physical Review B*, 96(7):075146, Aug 2017.

[131] Yevgeny Bar Lev, Dante M. Kennes, Christian Klöckner, David R. Reichman, and Christoph Karrasch. Transport in quasiperiodic interacting systems: From superdiffusion to subdiffusion. *EPL (Europhysics Letters)*, 119(3):37003, Aug 2017.

[132] Marko Žnidarič and Marko Ljubotina. Interaction instability of localization in quasiperiodic systems. *Proc. Natl. Acad. Sci. U.S.A.*, 115(18):4595–4600, May 2018.

[133] Shenglong Xu, Xiao Li, Yi-Ting Hsu, Brian Swingle, and Sankar Das Sarma. Butterfly effect in interacting Aubry-Andre model: thermalization, slow scrambling, and many-body localization. *Phys. Rev. Research*, 1(3):032039, December 2019.

[134] Elmer V. H. Doggen and Alexander D. Mirlin. Many-body delocalization dynamics in long aubry-andré quasiperiodic chains. *Physical Review B*, 100(10):104203, Sep 2019.

[135] P G Harper. The General Motion of Conduction Electrons in a Uniform Magnetic Field, with Application to the Diamagnetism of Metals. *Proceedings of the Physical Society. Section A*, 68(10):879–892, October 1955.

[136] Serge Aubry and Gilles André. Analyticity breaking and anderson localization in incommensurate lattices. *Annals of Isr. Phys. Soc.*, 3:133, 01 1980.

[137] Xiao Li and S. Das Sarma. Mobility edge and intermediate phase in one-dimensional incommensurate lattice potentials. *Physical Review B*, 101(6):064203, Feb 2020.

[138] David J. Luitz, Nicolas Laflorencie, and Fabien Alet. Many-body localization edge in the random-field heisenberg chain. *Physical Review B*, 91(8):081103(R), Feb 2015.

[139] F. Setiawan, Dong-Ling Deng, and J. H. Pixley. Transport properties across the many-body localization transition in quasiperiodic and random systems. *Physical Review B*, 96(10):104205, Sep 2017.

[140] Kartiek Agarwal, Ehud Altman, Eugene Demler, Sarang Gopalakrishnan, David A. Huse, and Michael Knap. Rare-region effects and dynamics near the many-body localization transition. *Annalen der Physik*, 529(7):1600326, Jan 2017.

[141] Eduardo Mascarenhas, Hugo Flayac, and Vincenzo Savona. A Matrix-Product-Operator Approach to the Nonequilibrium Steady State of Driven-Dissipative Quantum Arrays. *Phys. Rev. A*, 92(2):022116, August 2015.

[142] Guifré Vidal. Efficient classical simulation of slightly entangled quantum computations. *Physical Review Letters*, 91(14):147902, Oct 2003.

[143] Masuo Suzuki. Improved Trotter-like formula. *Phys. Lett. A*, 180(3):232–234, September 1993.

[144] Marko Žnidarič, Antonello Scardicchio, and Vipin Kerala Varma. Diffusive and subdiffusive spin transport in the ergodic phase of a many-body localizable system. *Phys. Rev. Lett.*, 117(4):040601, July 2016.

[145] Fernando Iemini, Angelo Russomanno, Davide Rossini, Antonello Scardicchio, and Rosario Fazio. Signatures of many-body localization in the dynamics of two-site entanglement. *Physical Review B*, 94(21):214206, Dec 2016.

[146] Giuseppe De Tomasi, Soumya Bera, Jens H. Bardarson, and Frank Pollmann. Quantum Mutual Information as a Probe for Many-Body Localization. *Phys. Rev. Lett.*, 118(1):016804, January 2017.

[147] Berry Groisman, Sandu Popescu, and Andreas Winter. On the quantum, classical and total amount of correlations in a quantum state. *Phys. Rev. A*, 72(3):032317, September 2005.

[148] Ian Mondragon-Shem, Arijeet Pal, Taylor L. Hughes, and Chris R. Laumann. Many-body mobility edge due to symmetry-constrained dynamics and strong interactions. *Physical Review B*, 92(6):064203, August 2015.

[149] Elliott Baygan, S. P. Lim, and D. N. Sheng. Many-body localization and mobility edge in a disordered spin- 1 2 Heisenberg ladder. *Physical Review B*, 92(19):195153, November 2015.

[150] Xiaopeng Li, J. H. Pixley, Dong-Ling Deng, Sriram Ganeshan, and S. Das Sarma. Quantum nonergodicity and fermion localization in a system with a single-particle mobility edge. *Physical Review B*, 93(18):184204, May 2016.

[151] Sabyasachi Nag and Arti Garg. Many-body mobility edges in a one-dimensional system of interacting fermions. *Physical Review B*, 96(6):060203(R), August 2017.

[152] Ofer Aharony, Steven S. Gubser, Juan Maldacena, Hirosi Ooguri, and Yaron Oz. Large n field theories, string theory and gravity. *Physics Reports*, 323(3-4):183–386, Jan 2000.

[153] Thomas Hartman, Sean A. Hartnoll, and Raghu Mahajan. Upper bound on diffusivity. *Physical Review Letters*, 119(14):141601, Oct 2017.

[154] Andrew Lucas. Constraints on hydrodynamics from many-body quantum chaos, 2017.

[155] Jacopo De Nardis, Sarang Gopalakrishnan, Romain Vasseur, and Brayden Ware. Subdiffusive hydrodynamics of nearly-integrable anisotropic spin chains. *Proceedings of the National Academy of Sciences*, 119(34):e2202823119, August 2022. arXiv:2109.13251 [cond-mat].

[156] Hansveer Singh, Brayden A. Ware, Romain Vasseur, and Aaron J. Friedman. Subdiffusion and many-body quantum chaos with kinetic constraints. *Physical Review Letters*, 127(23):230602, December 2021. arXiv:2108.02205 [cond-mat, physics:quant-ph].

[157] Jason Iaconis, Andrew Lucas, and Rahul Nandkishore. Multipole conservation laws and subdiffusion in any dimension. *Physical Review E*, 103(2):022142, February 2021. Publisher: American Physical Society.

[158] Andrey Gromov, Andrew Lucas, and Rahul M. Nandkishore. Fracton hydrodynamics. *Physical Review Research*, 2(3):033124, July 2020. Publisher: American Physical Society.

[159] Johannes Feldmeier, Pablo Sala, Giuseppe De Tomasi, Frank Pollmann, and Michael Knap. Anomalous Diffusion in Dipole- and Higher-Moment-Conserving Systems. *Physical Review Letters*, 125(24):245303, December 2020. Publisher: American Physical Society.

[160] Alan Morningstar, Vedika Khemani, and David A. Huse. Kinetically constrained freezing transition in a dipole-conserving system. *Physical Review B*, 101(21):214205, Jun 2020.

[161] Jason Iaconis, Sagar Vijay, and Rahul Nandkishore. Anomalous subdiffusion from subsystem symmetries. *Physical Review B*, 100(21):214301, December 2019. Publisher: American Physical Society.

[162] Paolo Glorioso, Jinkang Guo, Joaquin F. Rodriguez-Nieva, and Andrew Lucas. Breakdown of hydrodynamics below four dimensions in a fracton fluid. *Nature Physics*, 18(8):912–917, August 2022. arXiv:2105.13365 [cond-mat, physics:hep-th].

[163] Hansveer Singh, Romain Vasseur, and Sarang Gopalakrishnan. Fredkin staircase: An integrable system with a finite-frequency drude peak. *Physical Review Letters*, 130(4):046001, jan 2023.

[164] Jonas Richter and Arijeet Pal. Anomalous hydrodynamics in a class of scarred frustration-free Hamiltonians. *Physical Review Research*, 4:L012003, January 2022. ADS Bibcode: 2022PhRvR...4a2003R.

[165] Pablo Sala, Julius Lehmann, Tibor Rakovszky, and Frank Pollmann. Dynamics in Systems with Modulated Symmetries, October 2021. arXiv:2110.08302 [cond-mat].

[166] John McGreevy. Generalized Symmetries in Condensed Matter, June 2022. arXiv:2204.03045 [cond-mat, physics:hep-th].

[167] Paul Niklas Jepsen, Jesse Amato-Grill, Ivana Dimitrova, Wen Wei Ho, Eugene Demler, and Wolfgang Ketterle. Spin transport in a tunable Heisenberg model realized with ultracold atoms. *Nature*, 588(7838):403–407, December 2020. Number: 7838 Publisher: Nature Publishing Group.

[168] Sebastian Geier, Nithiwadee Thaicharoen, Clément Hainaut, Titus Franz, Andre Salzinger, Annika Tebben, David Grimshandl, Gerhard Zürn, and Matthias Weidemüller. Floquet Hamiltonian Engineering of an Isolated Many-Body Spin System. *Science*, 374(6571):1149–1152, November 2021. arXiv:2105.01597 [cond-mat, physics:quant-ph].

[169] P. Scholl, H. J. Williams, G. Bornet, F. Wallner, D. Barredo, T. Lahaye, A. Browaeys, L. Henriet, A. Signoles, C. Hainaut, T. Franz, S. Geier, A. Tebben, A. Salzinger, G. Zürn, and M. Weidemüller. Microwave-engineering of programmable XXZ Hamiltonians in arrays of Rydberg atoms, March 2022. arXiv:2107.14459 [cond-mat, physics:physics, physics:quant-ph].

[170] David Wei, Antonio Rubio-Abadal, Bingtian Ye, Francisco Machado, Jack Kemp, Kritsana Srakaew, Simon Hollerith, Jun Rui, Sarang Gopalakrishnan, Norman Y. Yao, Immanuel Bloch, and Johannes Zeiher. Quantum gas microscopy of Kardar-Parisi-Zhang superdiffusion. *Science*, 376(6594):716–720, May 2022. arXiv:2107.00038 [cond-mat, physics:quant-ph].

[171] A. Scheie, N. E. Sherman, M. Dupont, S. E. Nagler, M. B. Stone, G. E. Granroth, J. E. Moore, and D. A. Tennant. Detection of Kardar–Parisi–Zhang hydrodynamics in a quantum Heisenberg spin-1/2 chain. *Nature Physics*, 17(6):726–730, June 2021. Number: 6 Publisher: Nature Publishing Group.

[172] Alexandre Blais, Arne L. Grimsmo, S. M. Girvin, and Andreas Wallraff. Circuit quantum electrodynamics. *Rev. Mod. Phys.*, 93:025005, May 2021.

[173] Wit Busza, Krishna Rajagopal, and Wilke van der Schee. Heavy ion collisions: The big picture and the big questions. *Annual Review of Nuclear and Particle Science*, 68(1):339–376, oct 2018.

[174] M. A. Cazalilla, R. Citro, T. Giamarchi, E. Orignac, and M. Rigol. One dimensional bosons: From condensed matter systems to ultracold gases. *Rev. Mod. Phys.*, 83:1405–1466, Dec 2011.

[175] Adilet Imambekov, Thomas L. Schmidt, and Leonid I. Glazman. One-dimensional quantum liquids: Beyond the luttinger liquid paradigm. *Rev. Mod. Phys.*, 84:1253–1306, Sep 2012.

[176] Xi-Wen Guan, Murray T. Batchelor, and Chaohong Lee. Fermi gases in one dimension: From bethe ansatz to experiments. *Rev. Mod. Phys.*, 85:1633–1691, Nov 2013.

[177] B. Bertini, F. Heidrich-Meisner, C. Karrasch, T. Prosen, R. Steinigeweg, and M. Z. Znidaric. Finite-temperature transport in one-dimensional quantum lattice models. *Reviews of Modern Physics*, 93(2):025003, may 2021.

[178] Steven R. White. Density matrix formulation for quantum renormalization groups. *Physical Review Letters*, 69(19):2863–2866, November 1992.

[179] Ulrich Schollwoeck. The density-matrix renormalization group in the age of matrix product states. *Annals of Physics*, 326(1):96–192, January 2011. arXiv: 1008.3477.

[180] Sebastian Paeckel, Thomas Köhler, Andreas Swoboda, Salvatore R. Manmana, Ulrich Schollwöck, and Claudius Hubig. Time-evolution methods for matrix-product states. *Annals of Physics*, 411:167998, December 2019.

[181] M Schulz, S R Taylor, A Scardicchio, and M Žnidarič. Phenomenology of anomalous transport in disordered one-dimensional systems. *Journal of Statistical Mechanics: Theory and Experiment*, 2020(2):023107, Feb 2020.

[182] Eyal Leviatan, Frank Pollmann, Jens H. Bardarson, David A. Huse, and Ehud Altman. Quantum thermalization dynamics with matrix-product states, 2017.

[183] Benedikt Kloss, Yevgeny Bar Lev, and David Reichman. Time-dependent variational principle in matrix-product state manifolds: Pitfalls and potential. *Physical Review B*, 97(2):024307, Jan 2018.

[184] Christopher David White, Michael Zaletel, Roger S. K. Mong, and Gil Refael. Quantum dynamics of thermalizing systems. *Physical Review B*, 97(3):035127, Jan 2018.

[185] C. Krumnow, J. Eisert, and Ö. Legeza. Towards overcoming the entanglement barrier when simulating long-time evolution, 2019.

[186] Bingtian Ye, Francisco Machado, Christopher David White, Roger S. K. Mong, and Norman Y. Yao. Emergent hydrodynamics in nonequilibrium quantum systems. *Physical Review Letters*, 125(3):030601, Jul 2020.

[187] Tibor Rakovszky, C. W. von Keyserlingk, and Frank Pollmann. Dissipation-assisted operator evolution method for capturing hydrodynamic transport, 2020.

[188] Thomas Klein Kvorning, Loïc Herviou, and Jens H. Bardarson. Time-evolution of local information: thermalization dynamics of local observables. *arXiv:2105.11206 [cond-mat, physics:quant-ph]*, May 2021. arXiv: 2105.11206.

[189] Alessio Lerose, Michael Sonner, and Dmitry A. Abanin. Overcoming the entanglement barrier in quantum many-body dynamics via space-time duality, 2022.

[190] Jonathan Wurtz and Anatoli Polkovnikov. Quantum Hydrodynamics in Spin Chains with Phase Space Methods. *ArXiv e-prints*, 1808:arXiv:1808.08977, August 2018.

[191] Jonathan Wurtz, Anatoli Polkovnikov, and Dries Sels. Cluster Truncated Wigner Approximation in Strongly Interacting Systems. *Annals of Physics*, 395:341–365, August 2018. arXiv: 1804.10217.

[192] Bihui Zhu, Ana Maria Rey, and Johannes Schachenmayer. A generalized phase space approach for solving quantum spin dynamics. *arXiv:1905.08782 [cond-mat, physics:physics, physics:quant-ph]*, May 2019. arXiv: 1905.08782.

[193] C. W. von Keyserlingk, Frank Pollmann, and Tibor Rakovszky. Operator backflow and the classical simulation of quantum transport, 2021.

[194] Christopher David White. Effective dissipation rate in a Liouvillean graph picture of high-temperature quantum hydrodynamics. *arXiv:2108.00019 [cond-mat]*, July 2021. arXiv: 2108.00019.

[195] Adam Nahum, Sthitadhi Roy, Sagar Vijay, and Tianci Zhou. Real-time correlators in chaotic quantum many-body systems. Technical Report arXiv:2205.11544, arXiv, May 2022. arXiv:2205.11544 [cond-mat, physics:hep-th, physics:quant-ph] type: article.

[196] Adam Nahum, Sagar Vijay, and Jeongwan Haah. Operator spreading in random unitary circuits. *Physical Review X*, 8(2):021014, Apr 2018.

[197] Tibor Rakovszky, Frank Pollmann, and C. W. von Keyserlingk. Diffusive hydrodynamics of out-of-time-ordered correlators with charge conservation. *Physical Review X*, 8(3):031058, Sep 2018.

[198] Vedika Khemani, Ashvin Vishwanath, and David A. Huse. Operator spreading and the emergence of dissipative hydrodynamics under unitary evolution with conservation laws. *Physical Review X*, 8(3):031057, Sep 2018.

[199] Sarang Gopalakrishnan, David A. Huse, Vedika Khemani, and Romain Vasseur. Hydrodynamics of operator spreading and quasiparticle diffusion in interacting integrable systems. *Physical Review B*, 98(22):220303(R), Dec 2018.

[200] Amos Chan, Andrea De Luca, and J. T. Chalker. Solution of a minimal model for many-body quantum chaos. *Physical Review X*, 8(4):041019, Nov 2018.

[201] Daniel E. Parker, Xiangyu Cao, Alexander Avdoshkin, Thomas Scaffidi, and Ehud Altman. A universal operator growth hypothesis. *Physical Review X*, 9(4):041017, Oct 2019.

[202] Simon Jesenko and Marko Znidaric. Finite-temperature magnetization transport of the one-dimensional anisotropic heisenberg model. *Phys. Rev. B*, 84:174438, Nov 2011.

[203] Stephan Langer, Markus Heyl, Ian P. McCulloch, and Fabian Heidrich-Meisner. Real-time energy dynamics in spin-$\frac{1}{2}$ heisenberg chains. *Phys. Rev. B*, 84:205115, Nov 2011.

[204] R. J. Sánchez, V. K. Varma, and V. Oganesyan. Anomalous and regular transport in spin-$\frac{1}{2}$ chains: ac conductivity. *Phys. Rev. B*, 98:054415, Aug 2018.

[205] Maxime Dupont and Joel E. Moore. Universal spin dynamics in infinite-temperature one-dimensional quantum magnets. *Phys. Rev. B*, 101:121106(R), Mar 2020.

[206] Sarang Gopalakrishnan and Romain Vasseur. Kinetic theory of spin diffusion and superdiffusion in xxz spin chains. *Phys. Rev. Lett.*, 122:127202, Mar 2019.

[207] Jacopo De Nardis, Denis Bernard, and Benjamin Doyon. Diffusion in generalized hydrodynamics and quasiparticle scattering. *SciPost Physics*, 6(4):049, April 2019.

[208] Marko Medenjak, Katja Klobas, and Tomaž Prosen. Diffusion in Deterministic Interacting Lattice Systems. *Physical Review Letters*, 119(11):110603, September 2017. Publisher: American Physical Society.

[209] Enej Ilievski and Jacopo De Nardis. Microscopic Origin of Ideal Conductivity in Integrable Quantum Models. *Physical Review Letters*, 119(2):020602, July 2017. Publisher: American Physical Society.

[210] Vir B. Bulchandani, Romain Vasseur, Christoph Karrasch, and Joel E. Moore. Solvable Hydrodynamics of Quantum Integrable Systems. *Physical Review Letters*, 119(22):220604, November 2017. Publisher: American Physical Society.

[211] Andrea De Luca, Mario Collura, and Jacopo De Nardis. Nonequilibrium spin transport in integrable spin chains: Persistent currents and emergence of magnetic domains. *Physical Review B*, 96(2):020403(R), July 2017. Publisher: American Physical Society.

[212] Enej Ilievski and Tomaž Prosen. Thermodyamic Bounds on Drude Weights in Terms of Almost-conserved Quantities. *Communications in Mathematical Physics*, 318(3):809–830, March 2013.

[213] R. G. Pereira, V. Pasquier, J. Sirker, and I. Affleck. Exactly conserved quasilocal operators for the XXZ spin chain. *Journal of Statistical Mechanics: Theory and Experiment*, 2014(9):P09037, September 2014. Publisher: IOP Publishing.

[214] X. Zotos, F. Naef, and P. Prelovsek. Transport and conservation laws. *Physical Review B*, 55(17):11029–11032, May 1997. Publisher: American Physical Society.

[215] C. Psaroudaki and X. Zotos. Spin and magnetothermal transport in the 1/2 XXZ chain. *Journal of Statistical Mechanics: Theory and Experiment*, 2016(6):063103, June 2016. Publisher: IOP Publishing.

[216] Mario Collura, Andrea De Luca, and Jacopo Viti. Analytic solution of the domain-wall nonequilibrium stationary state. *Physical Review B*, 97(8):081111(R), February 2018. Publisher: American Physical Society.

[217] X. Zotos. Finite Temperature Drude Weight of the One-Dimensional Spin- $1/2$ Heisenberg Model. *Physical Review Letters*, 82(8):1764–1767, February 1999. Publisher: American Physical Society.

[218] J. Herbrych, P. Prelovsek, and X. Zotos. Finite-temperature Drude weight within the anisotropic Heisenberg chain. *Physical Review B*, 84(15):155125, October 2011. Publisher: American Physical Society.

[219] Enej Ilievski, Jacopo De Nardis, Marko Medenjak, and Tomaž Prosen. Superdiffusion in One-Dimensional Quantum Lattice Models. *Physical Review Letters*, 121(23):230602, December 2018. Publisher: American Physical Society.

[220] Marko Medenjak, Christoph Karrasch, and Tomaž Prosen. Lower Bounding Diffusion Constant by the Curvature of Drude Weight. *Physical Review Letters*, 119(8):080602, August 2017. Publisher: American Physical Society.

[221] Robin Steinigeweg, Jochen Gemmer, and Wolfram Brenig. Spin-Current Autocorrelations from Single Pure-State Propagation. *Physical Review Letters*, 112(12):120601, March 2014. Publisher: American Physical Society.

[222] C. Karrasch, R. G. Pereira, and J. Sirker. Low temperature dynamics of nonlinear Luttinger liquids. *New Journal of Physics*, 17(10):103003, September 2015. Publisher: IOP Publishing.

[223] B. L. Altshuler, R. M. Konik, and A. M. Tsvelik. Low temperature correlation functions in integrable models: Derivation of the large distance and time asymptotics from the form factor expansion. *Nuclear Physics B*, 739(3):311–327, April 2006.

[224] R. Steinigeweg. Spin transport in the XXZ model at high temperatures: Classical dynamics vs. quantum S=1/2 autocorrelations. *EPL (Europhysics Letters)*, 97(6):67001, March 2012. Publisher: IOP Publishing.

[225] Kedar Damle and Subir Sachdev. Spin dynamics and transport in gapped one-dimensional Heisenberg antiferromagnets at nonzero temperatures. *Physical Review B*, 57(14):8307–8339, April 1998. Publisher: American Physical Society.

[226] Kedar Damle and Subir Sachdev. Universal Relaxational Dynamics of Gapped One-Dimensional Models in the Quantum Sine-Gordon Universality Class. *Physical Review Letters*, 95(18):187201, October 2005. Publisher: American Physical Society.

[227] Tomaz Prosen and Bojan Zunkovic. Macroscopic Diffusive Transport in a Microscopically Integrable Hamiltonian System. *Physical Review Letters*, 111(4):040602, July 2013. Publisher: American Physical Society.

[228] Jacopo De Nardis, Sarang Gopalakrishnan, Romain Vasseur, and Brayden Ware. Stability of superdiffusion in nearly integrable spin chains. *Physical Review Letters*, 127(5):057201, July 2021. arXiv: 2102.02219.

[229] Yevgeny Bar Lev, Guy Cohen, and David R. Reichman. Absence of diffusion in an interacting system of spinless fermions on a one-dimensional disordered lattice. *Physical Review Letters*, 114(10):100601, Mar 2015.

[230] Kartiek Agarwal, Sarang Gopalakrishnan, Michael Knap, Markus Muller, and Eugene Demler. Anomalous diffusion and griffiths effects near the many-body localization transition. *Physical Review Letters*, 114(16):160401, Apr 2015.

[231] E. J. Torres-Herrera and Lea F. Santos. Dynamics at the many-body localization transition. *Physical Review B*, 92(1):014208, Jul 2015.

[232] David J. Luitz, Nicolas Laflorencie, and Fabien Alet. Extended slow dynamical regime close to the many-body localization transition. *Physical Review B*, 93(6):060201, February 2016.

[233] P. Prelovsek and J. Herbrych. Self-consistent approach to many-body localization and subdiffusion. *Physical Review B*, 96(3):035130, Jul 2017.

[234] J. J. Mendoza-Arenas, M. Žnidarič, V. K. Varma, J. Goold, S. R. Clark, and A. Scardicchio. Asymmetry in energy versus spin transport in certain interacting disordered systems. *Physical Review B*, 99(9):094435, Mar 2019.

[235] David J. Luitz, Ivan Khaymovich, and Yevgeny Bar Lev. Multifractality and its role in anomalous transport in the disordered xxz spin-chain. *SciPost Physics Core*, 2(2), Apr 2020.

[236] Robert B. Griffiths. Nonanalytic Behavior Above the Critical Point in a Random Ising Ferromagnet. *Physical Review Letters*, 23(1):17–19, July 1969.

[237] Ronen Vosk, David A. Huse, and Ehud Altman. Theory of the many-body localization transition in one-dimensional systems. *Physical Review X*, 5(3):031032, Sep 2015.

[238] Sarang Gopalakrishnan, Kartiek Agarwal, Eugene A. Demler, David A. Huse, and Michael Knap. Griffiths effects and slow dynamics in nearly many-body localized systems. *Physical Review B*, 93(13):134206, April 2016.

[239] David J. Luitz and Yevgeny Bar Lev. Anomalous thermalization in ergodic systems. *Physical Review Letters*, 117(17):170404, Oct 2016.

[240] J. Suntajs, J. Bonca, T. Prosen, and L. Vidmar. Quantum chaos challenges many-body localization. *Physical Review E*, 102(6):062144, December 2020. arXiv:1905.06345 [cond-mat, physics:hep-th, physics:quant-ph].

[241] D. A. Abanin, J. H. Bardarson, G. De Tomasi, S. Gopalakrishnan, V. Khemani, S. A. Parameswaran, F. Pollmann, A. C. Potter, M. Serbyn, and R. Vasseur. Distinguishing localization from chaos: Challenges in finite-size systems. *Annals of Physics*, 427:68415, April 2021. ADS Bibcode: 2021AnPhy.42768415A.

[242] Dries Sels and Anatoli Polkovnikov. Dynamical obstruction to localization in a disordered spin chain. *Physical Review E*, 104(5):054105, November 2021. arXiv:2009.04501 [cond-mat, physics:quant-ph].

[243] Roopayan Ghosh and Marko Žnidarič. Theory of growth of number entropy in disordered systems. *arXiv:2112.12987 [cond-mat]*, January 2022. arXiv: 2112.12987.

[244] Roopayan Ghosh and Marko Žnidarič. Resonance-induced growth of number entropy in strongly disordered systems. *Physical Review B*, 105:144203, April 2022. ADS Bibcode: 2022PhRvB.105n4203G.

[245] Alan Morningstar, Luis Colmenarez, Vedika Khemani, David J. Luitz, and David A. Huse. Avalanches and many-body resonances in many-body localized systems. *Physical Review B*, 105:174205, May 2022. ADS Bibcode: 2022PhRvB.105q4205M.

[246] Piotr Sierant and Jakub Zakrzewski. Challenges to observation of many-body localization. *Physical Review B*, 105:224203, June 2022. ADS Bibcode: 2022PhRvB.105v4203S.

[247] Philip J. D. Crowley and Anushya Chandran. A constructive theory of the numerically accessible many-body localized to thermal crossover. *SciPost Physics*, 12(6):201, June 2022. arXiv:2012.14393 [cond-mat].

[248] P. W. Anderson. Absence of Diffusion in Certain Random Lattices. *Physical Review*, 109(5):1492–1505, March 1958.

[249] M. B. Hastings. Solving gapped Hamiltonians locally. *Physical Review B*, 73(8):085115, February 2006.

[250] Andras Molnar, Norbert Schuch, Frank Verstraete, and J. Ignacio Cirac. Approximating Gibbs states of local Hamiltonians efficiently with projected entangled pair states. *Physical Review B*, 91(4):045138, January 2015. Publisher: American Physical Society.

[251] Davide Nigro. On the uniqueness of the steady-state solution of the lindblad–gorini–kossakowski–sudarshan equation. *Journal of Statistical Mechanics: Theory and Experiment*, 2019(4):043202, apr 2019.

[252] Bingtian Ye, Francisco Machado, Jack Kemp, Ross B. Hutson, and Norman Y. Yao. Universal Kardar-Parisi-Zhang dynamics in integrable quantum systems, May 2022. arXiv:2205.02853 [cond-mat, physics:quant-ph].

[253] Marko Ljubotina, Marko Z. Znidaric, and Tomaz Prosen. Kardar-parisi-zhang physics in the quantum heisenberg magnet. *Physical Review Letters*, 122(21):210602, may 2019.

[254] Paolo Glorioso, Luca V. Delacrétaz, Xiao Chen, Rahul M. Nandkishore, and Andrew Lucas. Hydrodynamics in lattice models with continuous non-Abelian symmetries. *SciPost Physics*, 10(1):015, January 2021. arXiv:2007.13753 [cond-mat, physics:hep-th].

[255] L. de Haan and Ana Ferreira. *Extreme value theory: an introduction*. Springer series in operations research. Springer, New York ; London, 2006. OCLC: ocm70173287.

[256] Subhayan Sahu and Brian Swingle. Efficient tensor network simulation of quantum many-body physics on sparse graphs. *arXiv e-prints*, page arXiv:2206.04701, June 2022.

[257] J J Mendoza-Arenas, S Al-Assam, S R Clark, and D Jaksch. Heat transport in thexxzspin chain: from ballistic to diffusive regimes and dephasing enhancement. *Journal of Statistical Mechanics: Theory and Experiment*, 2013(07):P07007, Jul 2013.

[258] Marko Žnidarič and Martin Horvat. Transport in a disordered tight-binding chain with dephasing. *The European Physical Journal B*, 86(2), Feb 2013.

[259] Marko Žnidarič, Juan Jose Mendoza-Arenas, Stephen R. Clark, and John Goold. Dephasing enhanced spin transport in the ergodic phase of a many-body localizable system. *Annalen der Physik*, 529(7):1600298, Dec 2016.

[260] Adam Nahum, Jonathan Ruhman, Sagar Vijay, and Jeongwan Haah. Quantum Entanglement Growth Under Random Unitary Dynamics. *Physical Review X*, 7(3):031016, July 2017. arXiv:1608.06950 [cond-mat, physics:hep-th, physics:quant-ph].

[261] Brian Skinner, Jonathan Ruhman, and Adam Nahum. Measurement-Induced Phase Transitions in the Dynamics of Entanglement. *Physical Review X*, 9(3):031009, July 2019. arXiv:1808.05953 [cond-mat, physics:hep-th, physics:quant-ph].

[262] Shenglong Xu and Brian Swingle. Accessing scrambling using matrix product operators. *Nature Physics*, 16(2):199–204, February 2020. arXiv:1802.00801 [cond-mat, physics:hep-th, physics:quant-ph].

[263] Andrew C. Potter and Romain Vasseur. Entanglement dynamics in hybrid quantum circuits. pages 211–249. 2022. arXiv:2111.08018 [cond-mat, physics:quant-ph].

[264] Matthew P. A. Fisher, Vedika Khemani, Adam Nahum, and Sagar Vijay. Random Quantum Circuits. *Annual Review of Condensed Matter Physics*, 14(1):335–379, March 2023. arXiv:2207.14280 [cond-mat, physics:quant-ph].

[265] Thierry Giamarchi. *Quantum Physics in One Dimension*. Oxford University Press, December 2003.

[266] Román Orús. A practical introduction to tensor networks: Matrix product states and projected entangled pair states. *Ann. Phys.*, 349:117–158, 2014.

[267] J. Ignacio Cirac, David Pérez-García, Norbert Schuch, and Frank Verstraete. Matrix product states and projected entangled pair states: Concepts, symmetries, theorems. *Rev. Mod. Phys.*, 93:045003, Dec 2021.

[268] Jutho Haegeman, J. Ignacio Cirac, Tobias J. Osborne, Iztok Pizorn, Henri Verschelde, and Frank Verstraete. Time-dependent variational principle for quantum lattices. *Phys. Rev. Lett.*, 107:070601, Aug 2011.

[269] Eyal Leviatan, Frank Pollmann, Jens H. Bardarson, David A. Huse, and Ehud Altman. Quantum thermalization dynamics with matrix-product states, 2017.

[270] Tibor Rakovszky, C. W. von Keyserlingk, and Frank Pollmann. Dissipation-assisted operator evolution method for capturing hydrodynamic transport. *Phys. Rev. B*, 105:075131, Feb 2022.

[271] Toma ž Prosen and Marko Žnidarič. Diffusive high-temperature transport in the one-dimensional hubbard model. *Phys. Rev. B*, 86:125118, Sep 2012.

[272] J. J. Mendoza-Arenas, S. R. Clark, and D. Jaksch. Coexistence of energy diffusion and local thermalization in nonequilibrium xxz spin chains with integrability breaking. *Phys. Rev. E*, 91:042129, Apr 2015.

[273] Marko Žnidarič. Nonequilibrium steady-state kubo formula: Equality of transport coefficients. *Phys. Rev. B*, 99:035143, Jan 2019.

[274] Hendrik Weimer, Augustine Kshetrimayum, and Romá n Orús. Simulation methods for open quantum many-body systems. *Reviews of Modern Physics*, 93(1), mar 2021.

[275] Heinz-Peter Breuer and Francesco Petruccione. *The Theory of Open Quantum Systems*. Oxford University Press, January 2007.

[276] A.G. Redfield. The theory of relaxation processes. In John S. Waugh, editor, *Advances in Magnetic Resonance*, volume 1 of *Advances in Magnetic and Optical Resonance*, pages 1–32. Academic Press, 1965.

[277] David A. Huse. Simple three-state model with infinitely many phases. *Phys. Rev. B*, 24:5180–5194, Nov 1981.

[278] S. Ostlund. Incommensurate and commensurate phases in asymmetric clock models. *Phys. Rev. B*, 24:398–405, Jul 1981.

[279] David A. Huse and Michael E. Fisher. Domain walls and the melting of commensurate surface phases. *Phys. Rev. Lett.*, 49:793–796, Sep 1982.

[280] David A. Huse, Anthony M. Szpilka, and Michael E. Fisher. Melting and wetting transitions in the three-state chiral clock model. *Physica A: Statistical Mechanics and its Applications*, 121(3):363–398, 1983.

[281] F. D. M. Haldane, P. Bak, and T. Bohr. Phase diagrams of surface structures from bethe-ansatz solutions of the quantum sine-gordon model. *Phys. Rev. B*, 28:2743–2745, Sep 1983.

[282] Steven Howes, Leo P. Kadanoff, and Marcel Den Nijs. Quantum model for commensurate-incommensurate transitions. *Nuclear Physics B*, 215(2):169–208, 1983.

[283] Helen Au-Yang, Barry M. McCoy, Jacques H.H. Perk, Shuang Tang, and Mu-Lin Yan. Commuting transfer matrices in the chiral potts models: Solutions of star-triangle equations with genus¿1. *Physics Letters A*, 123(5):219–223, 1987.

[284] Hannes Bernien, Sylvain Schwartz, Alexander Keesling, Harry Levine, Ahmed Omran, Hannes Pichler, Soonwon Choi, Alexander S. Zibrov, Manuel Endres, Markus Greiner, Vladan Vuletić, and Mikhail D. Lukin. Probing many-body dynamics on a 51-atom quantum simulator. *Nature*, 551(7682):579–584, nov 2017.

[285] Subir Sachdev. *Quantum Phase Transitions*. Cambridge University Press, 2 edition, 2011.

[286] Ye Zhuang, Hitesh J. Changlani, Norm M. Tubman, and Taylor L. Hughes. Phase diagram of the Z 3 parafermionic chain with chiral interactions. *Physical Review B*, 92(3):035154, July 2015.

[287] Rhine Samajdar, Soonwon Choi, Hannes Pichler, Mikhail D. Lukin, and Subir Sachdev. Numerical study of the chiral $\mathbb{z}_3$ quantum phase transition in one spatial dimension. *Phys. Rev. A*, 98:023614, Aug 2018.

[288] Seth Whitsitt, Rhine Samajdar, and Subir Sachdev. Quantum field theory for the chiral clock transition in one spatial dimension. *Phys. Rev. B*, 98:205118, Nov 2018.

[289] Leonardo Mazza, Jacopo Viti, Matteo Carrega, Davide Rossini, and Andrea De Luca. Energy transport in an integrable parafermionic chain via generalized hydrodynamics. *Phys. Rev. B*, 98:075421, Aug 2018.

[290] Naveen Nishad and G J Sreejith. Energy transport in z3 chiral clock model. *New Journal of Physics*, 24(1):013035, jan 2022.

[291] Sandipan Manna and G. J. Sreejith. Thermal drude weight in an integrable chiral clock model. *Phys. Rev. B*, 108:054304, Aug 2023.

[292] Rinat Kedem. Thermodynamics of the 3-state Potts Spin chain. *Journal of Statistical Physics*, 71(5-6):903–921, June 1993.

[293] Rinat Kedem and Barry M. McCoy. Construction of modular branching functions from Bethe's equations in the 3-state Potts chain. *Journal of Statistical Physics*, 71(5-6):865–901, June 1993.

[294] Yan-Wei Dai, Sam Young Cho, Murray T. Batchelor, and Huan-Qiang Zhou. Entanglement entropy and massless phase in the antiferromagnetic three-state quantum chiral clock model. *Phys. Rev. B*, 95:014419, Jan 2017.

[295] R J Baxter. The challenge of the chiral potts model. *Journal of Physics: Conference Series*, 42(1):11, jun 2006.

[296] Giuseppe Albertini, Barry M. McCoy, and Jacques H.H. Perk. Commensurate-incommensurate transition in the ground state of the superintegrable chiral potts model. *Physics Letters A*, 135(3):159–166, 1989.

[297] Barry M. McCoy and Shi shyr Roan. Excitation spectrum and phase structure of the chiral potts model. *Physics Letters A*, 150(8):347–354, 1990.

[298] S R Clark, J Prior, M J Hartmann, D Jaksch, and M B Plenio. Exact matrix product solutions in the heisenberg picture of an open quantum spin chain. *New J. Phys.*, 12(2):025005, feb 2010.

[299] Tomaž Prosen. Exact nonequilibrium steady state of an open hubbard chain. *Phys. Rev. Lett.*, 112:030603, Jan 2014.

[300] Vladislav Popkov and Carlo Presilla. Obtaining pure steady states in nonequilibrium quantum systems with strong dissipative couplings. *Phys. Rev. A*, 93:022111, Feb 2016.

[301] Vladislav Popkov, Tomaž Prosen, and Lenart Zadnik. Inhomogeneous matrix product ansatz and exact steady states of boundary-driven spin chains at large dissipation. *Phys. Rev. E*, 101:042122, Apr 2020.

[302] Hendrik Weimer, Augustine Kshetrimayum, and Román Orús. Simulation methods for open quantum many-body systems. *Rev. Mod. Phys.*, 93:015008, Mar 2021.

[303] Gabriel T. Landi, Dario Poletti, and Gernot Schaller. Nonequilibrium boundary-driven quantum systems: Models, methods, and properties. *Rev. Mod. Phys.*, 94:045006, Dec 2022.

[304] Michael Hartmann, Günter Mahler, and Ortwin Hess. Existence of temperature on the nanoscale. *Phys. Rev. Lett.*, 93:080402, Aug 2004.

[305] M Hartmann and G Mahler. Measurable consequences of the local breakdown of the concept of temperature. *EPL*, 70(5):579–585, jun 2005.

[306] Michael Hartmann. Minimal length scales for the existence of local temperature. *Contemp. Phys.*, 47(2):89–102, 2006.

[307] Artur García-Saez, Alessandro Ferraro, and Antonio Acín. Local temperature in quantum thermal states. *Phys. Rev. A*, 79:052340, May 2009.

[308] M. Kliesch, C. Gogolin, M. J. Kastoryano, A. Riera, and J. Eisert. Locality of temperature. *Phys. Rev. X*, 4:031019, Jul 2014.

[309] Zi Cai and Thomas Barthel. Algebraic versus exponential decoherence in dissipative many-particle systems. *Phys. Rev. Lett.*, 111:150403, Oct 2013.

[310] John Martyn and Brian Swingle. Product spectrum ansatz and the simplicity of thermal states. *Phys. Rev. A*, 100:032107, Sep 2019.

[311] Troy J. Sewell, Christopher David White, and Brian Swingle. Thermal multi-scale entanglement renormalization ansatz for variational gibbs state preparation, 2022.

[312] Ancel Larzul and Marco Schirò. Energy transport between strange quantum baths, 2022.

[313] Paolo Zanardi. Entanglement of quantum evolutions. *Phys. Rev. A*, 63:040304, Mar 2001.

[314] Cecilia Chiaracane, Francesca Pietracaprina, Archak Purkayastha, and John Goold. Quantum dynamics in the interacting fibonacci chain. *Physical Review B*, 103(18):184205, May 2021.

[315] M. Ganahl, M. Haque, and H. G. Evertz. Quantum Bowling: Particle-hole transmutation in one-dimensional strongly interacting lattice models. *arXiv:1302.2667 [cond-mat]*, February 2013.

[316] Masuo Suzuki. General theory of fractal path integrals with applications to many-body theories and statistical physics. *Journal of Mathematical Physics*, 32(2):400–407, February 1991.

[317] J. J. Mendoza-Arenas, M. Znidaric, V. K. Varma, J. Goold, S. R. Clark, and A. Scardicchio. Asymmetry in energy versus spin transport in certain interacting disordered systems. *Phys. Rev. B*, 99:094435, Mar 2019.

[318] Hendrik Weimer, Augustine Kshetrimayum, and Román Orús. Simulation methods for open quantum many-body systems. *Rev. Mod. Phys.*, 93:015008, Mar 2021.